MODELLING AND FEASIBILITY ANALYSIS OF A STANDALONE RENEWABLE HYBRID (PV-WIND-BIOMASS) MICROGRID

by

MOHAMMAD IMRIAJ

SAIF IMRAN PASHA

BACHELOR OF SCIENCE IN ELECTRICAL AND ELECTRONIC ENGINEERING

Department of Electrical and Electronic Engineering
INTERNATIONAL ISLAMIC UNIVERSITY CHITTAGONG

JULY 2022

MODELLING AND FEASIBILITY ANALYSIS OF A STANDALONE RENEWABLE HYBRID (PV-WIND-BIOMASS) MICROGRID

by

MOHAMMAD IMRIAJ

SAIF IMRAN PASHA

A thesis
submitted as partial fulfilment of the requirement for the degree of

BACHELOR OF SCIENCE IN ELECTRICAL AND ELECTRONIC ENGINEERING

Department of Electrical and Electronic Engineering
INTERNATIONAL ISLAMIC UNIVERSITY CHITTAGONG

JULY 2022

CERTIFICATE OF APPROVAL

The thesis entitled "**Modelling and Feasibility Analysis of a Standalone Renewable Hybrid (PV-Wind-Biomass) Microgrid**" was submitted by **Mohammad Imriaj**, bearing Matric ID. **ET-161001** and **Saif Imran Pasha**, bearing Matric ID. **ET-161003** of session **Spring 2016**, to the Department of Electrical and Electronic Engineering, International Islamic University Chittagong, has been accepted as satisfactory in partial fulfilment of the requirements for the degree of Bachelor of Science in Engineering and approved for the examination held on **22nd July, 2022**.

_____

Supervisor
Engr. Md. Shahid Ullah
Assistant Professor,
Department of Electrical and Electronic Engineering
International Islamic University Chittagong.

DECLARATION

We hereby declare that this work was completed by us, and no part of this thesis has been submitted elsewhere for the granting of a degree or certificate.

_____

Mohammad Imriaj

_____

Saif Imran Pasha

ACKNOWLEDGMENT

All praises and thanks to Allah (SWT), the Lord of the world, the most Beneficent, without Whose mercy it would not be possible for us to complete this thesis.

Furthermore, we extend our profound appreciation and respect to our distinguished thesis advisor, Engr. Md. Shahid Ullah, Assistant Professor, Department of EEE, IIUC, for his continued support, encouragement, and direction during the composition of this thesis. Without his gentle guidance, it would have been impossible to finish the thesis. He was really encouraging and patient with us while we made repeated errors, and he always provided us encouragement by enhancing our strategies.

The academic members of our department, particularly our undergraduate adviser, Engr. Md. Lokman Hossain, Lecturer, Department of EEE, IIUC, are also acknowledged for their assistance. In addition, we are indebted to all the writers and researchers whose work we employed when doing research and writing this thesis.

Finally, we cannot express enough gratitude to our great parents, family, close friends, and well-wishers for their inexhaustible support and inspiration, which are the continual source of strength for achieving and maintaining consistency throughout our path.

Authors

ABSTRACT

Even with the most advanced development of the times, the electrical grid is not present in many remote places of the globe. Hybrid renewable energy systems can provide power to remote and isolated locations (HRES). This article focuses on the modelling, analysis, and simulation of a hybrid (photovoltaic/wind/biomass/battery storage) power system. In addition to the PV, wind, and biomass energy sources, the battery is used as a backup energy system. When the hybrid system's power is inadequate to power the load, the battery storage system constantly supplies the load with extra power from the PV system. A bidirectional DC-DC converter is used for the management and control of the energy system. Maximum power point tracking (MPPT) has been implemented in order to collect the maximum power point from the PV system. To reduce losses in the hybrid system, MPPT controllers and DC-DC converters are integrated. Solar photovoltaic (PV), wind turbine generator, and biomass systems are explored under varied climatic circumstances. MATLAB/Simulink and HOMER Pro are software programs that model, simulate, and assess the whole hybrid system.

TABLE OF CONTENTS

CERTIFICATE OF APPROVAL ii

DECLARATION iii

ACKNOWLEDGEMENT iv

ABSTRACT v

TABLE OF CONTENTS vi

LIST OF FIGURES x

LIST OF TABLES xiii

LIST OF ABBREVIATIONS xiv

CHAPTER 1 INTRODUCTION 1

1.1 Introduction to Renewable Energy 1
1.2 Introduction to Hybrid Renewable Energy System 4
1.3 Objective 5
1.4 Thesis Outline 6
1.5 Summary 6

CHAPTER 2 LITERATURE REVIEW 7

2.1 Introduction 7
2.2 PV Overview 8
2.2.1 PV Cell Overview 8
2.2.1.1 The Difference Between PV Cell, Module, and Array 8
2.2.1.1.1 PV Cell 8
2.2.1.1.2 PV Module 9
2.2.1.1.3 PV Array 9
2.2.1.2 Working Principle of PV Cell 9
2.2.1.3 PV Cell Technologies 10
2.3 Wind Overview 12
2.4 Biomass Overview 12
2.4.1 Bio-Reactor 13
2.4.2 Anaerobic digestion process 13
2.4.2.1 Hydrolysis 13
2.4.2.2 Acidogenesis 14
2.4.2.3 Acetogenesis 14
2.4.2.4 Methanogenesis 14

CHAPTER 3 METHODOLOGY **16**

3.1 PHOTOVOLTAIC ENERGY SYSTEM 16
3.1.1 Modelling of the PV System 16
3.1.1.1 Ideal PV Cell 16
3.1.1.2 Modelling of PV Array 17
3.1.1.3 PV Characteristics 19
3.1.1.4 Factors Affecting PV Characteristic Curves 21
3.1.1.4.1 The Effect of Solar Radiation Variations 21
3.1.1.4.2 The Effect of Temperature Variations 22
3.1.1.4.3 The Effect of Shading 23
3.1.2 Maximum Power Point Tracking of a PV System 24
3.1.2.1 MPPT Techniques 24
3.1.2.1.1 Perturb and Observe (P&O) 25
3.1.3 Finalized Model of the PV System 28

3.2 BATTERY AND POWER MANAGEMENT SYSTEM 29
3.2.1 Introduction 29
3.2.2 Battery 29

3.3 CONVERTERS 31
3.3.1 DC-DC Converters 31
3.3.1.1 Buck Converter 31
3.3.1.2 Boost Converter 32
3.3.1.2.1 First-Mode Operation 32
3.3.1.2.2 Second-Mode Operation 32
3.3.1.3 Buck-Boost Converter 33
3.3.1.3.1 First-Mode Operation 34
3.3.1.3.2 Second-Mode Operation 34
3.3.1.4 Buck-Boost Converter with MPPT 34
3.3.2 Bidirectional DC-DC Converter 36
3.3.2.1 Non-isolated Bidirectional DC-DC Converters 36
3.3.2.2 Isolated Bidirectional DC-DC Converters 36
3.3.3 Bidirectional DC-DC Converter for Charging and Discharging 37

3.4 WIND ENERGY SYSTEM 38
3.4.1 Wind System Components 38
3.4.2 Modelling of Wind Turbine System 38
3.4.3 Generators 41
3.4.3.1 Modelling of PMSG 41
3.4.4 Pitch Angle Controller 42
3.4.5 Finalized Model of Wind System 43

3.5 BIOGAS FUELED POWER SYSTEM 44
3.5.1 Introduction 44
3.5.2 Mathematical Modelling 44
3.5.2.1 Modelling of Biogas Reactor 44
3.5.2.1.1 Hydrolysis Modelling 45
3.5.2.1.2 Acidogenesis Modelling 46
3.5.2.1.3 Acetogenesis Modelling 47
3.5.2.1.4 Methanogenesis Modelling 48
3.5.2.1.5 Reactor Simulink Model 49
3.5.2.2 Modelling And Control Of A Microturbine-Generation System 49
3.5.2.2.1 Principles of microturbine working 50
3.5.2.2.2 Modelling of a microturbine 51
3.5.2.2.2.1 Speed control 51
3.5.2.2.2.2 Temperature control 52
3.5.2.2.2.3 Acceleration control 53
3.5.2.2.2.4 Fuel system control 53
3.5.2.2.2.5 Compressor-turbine model 54
3.5.2.2.2.6 Turbine dynamics 55
3.5.2.2.3 Permanent magnet synchronous generator model 56
3.5.2.3 Modelling of storage system 58
3.5.3 Finalized Model of Biomass System 59

3.6 LOCATION AND RESOURCES 60
3.6.1 Resource Analysis 60
3.6.1.1 Solar Resource Analysis 60
3.6.1.2 Wind Resource Analysis 61
3.6.1.3 Biomass Resource Analysis 61
3.6.2 Load Profile 62

CHAPTER 4 RESULT AND DISCUSSION 64

4.1 MATLAB-Simulink 64
4.2 HOMER Pro 70
4.2.1 Optimal System Report 70
4.2.2 Feasibility Analysis 75

CHAPTER 5 CONCLUSION AND FUTURE WORKS 77

5.1 Conclusions 77
5.2 Limitations 77
5.3 Future Works 77

REFERENCES **78**

APPENDIX **82**

LIST OF FIGURES

Figure 1.1	Global electricity generation, 2012–2040 (trillion kWh)	1
Figure 1.2	Global electricity production from renewable power, 2012–40	2
Figure 1.3	Solar PV global year on year change, 2001–2021	3
Figure 1.4	The global wind power year on year change, 2001–2021	3
Figure 1.5	Biomass power global year on year change, 2001–2021	4
Figure 1.6	Block diagram of the proposed hybrid system	5
Figure 2.1	Structures of PV devices	8
Figure 2.2	Working principle of PV cell	10
Figure 2.3	Timeline of PV cell energy conversion efficiencies from NREL	11
Figure 2.4	Basic components of horizontal-axis wind turbines	12
Figure 2.5	A schematic diagram of the four stages of AD process	15
Figure 3.1	The proposed PV system	16
Figure 3.2	The electrical circuit of a single-diode PV cell	17
Figure 3.3	The characteristic I-V curve of a PV cell	17
Figure 3.4	The Simulink model of the PV array	19
Figure 3.5	I-V and P-V characteristic curves	20
Figure 3.6	PV module characteristics showing the fill factor	21
Figure 3.7	I-V characteristics with different irradiance for the PV array	21
Figure 3.8	P-V characteristics with different irradiance for the PV array	22
Figure 3.9	Temperature effect on the PV characteristics	22
Figure 3.10	A PV array in shaded condition	23
Figure 3.11	The effect of shading on I-V and P-V characteristics	24
Figure 3.12	P-V characteristics (the principle of P&O technique)	26
Figure 3.13	Flowchart of P&O algorithm	27
Figure 3.14	The Simulink model of P&O algorithm	27
Figure 3.15	Simulink model of the PV System	28
Figure 3.16	The Simulink model of the battery	29
Figure 3.17	Battery discharge characteristics	30
Figure 3.18	A Buck converter	31
Figure 3.19	A Boost converter	32
Figure 3.20	An on-state operation of a boost converter	32
Figure 3.21	An off-state operation of a boost converter	32
Figure 3.22	A buck-boost converter	33
Figure 3.23	An on-state operation of a buck-boost converter	34
Figure 3.24	An off-state operation of a buck-boost converter	34
Figure 3.25	A PV array with a buck-boost converter	35
Figure 3.26	Bidirectional power flow	36
Figure 3.27	The proposed wind energy system	38
Figure 3.28	Cp-λ characteristics of wind turbines for various values of pitch angle β	40
Figure 3.29	Wind-turbine power characteristics at β = 0	41

Figure 3.30	The pitch angle controller in Simulink	42
Figure 3.31	Simulink model of the Wind system.	43
Figure 3.32	The proposed Biomass energy system	44
Figure 3.33	Simulink model for hydrolysis process	46
Figure 3.34	Simulink model for acidogenesis process	47
Figure 3.35	Simulink model represents acidogenesis process	48
Figure 3.36	Simulink model of methanogenesis process	48
Figure 3.37	Simulink model representing amount of methane output from reactor	49
Figure 3.38	Simulink model for the four stages of AD process	49
Figure 3.39	A schematic diagram of an MT system	51
Figure 3.40	Block diagram represents MT speed control	52
Figure 3.41	Block diagram of temperature controller	52
Figure 3.42	Block diagram of an MT control function	53
Figure 3.43	Block diagram of fuel system control	54
Figure 3.44	Block diagram of compressor-turbine model	55
Figure 3.45	Model of MT in Simulink, containing all control systems	56
Figure 3.46	Simulink model for the storage system	58
Figure 3.47	Simulink model of the Biomass system.	59
Figure 3.48	Optimal location for the Hybrid Power plant	60
Figure 3.49	Monthly Average Solar GHI (Global Horizontal Irradiance)	61
Figure 3.50	Monthly Average Wind Speed with Altitude and Anemometer Height	61
Figure 3.51	Monthly Average Available Biomass	62
Figure 3.52	Daily average load profile of Community load consumers	63
Figure 3.53	Daily average load profile of Commercial load consumers	63
Figure 4.1	Simulink model of the Hybrid Power Plant	64
Figure 4.2	Output voltage of the Hybrid Power Plant	65
Figure 4.3	Output current of the Hybrid Power Plant	65
Figure 4.4	Solar Radiation Input in Simulink	65
Figure 4.5	Temperature Input in Simulink	66
Figure 4.6	Output Voltage of the PV Plant	66
Figure 4.7	Output Current of the PV Plant	66
Figure 4.8	Battery Discharge with Time	67
Figure 4.9	Battery Recharging when PV Plant is in Operation	67
Figure 4.10	Wind Speed Input in Simulink	67
Figure 4.11	Output voltage of the Wind System	68
Figure 4.12	Output current of the Wind System	68
Figure 4.13	Methane Output of the Bioreactor	68
Figure 4.14	Output voltage of the Biomass Plant	69
Figure 4.15	Output current of the Biomass Plant	69
Figure 4.16	Hourly and Daily output of PV Plant (kW)	73
Figure 4.17	Hourly and Daily output of Wind System (kW)	73

Figure 4.18 Hourly and Daily output of Biomass generator (kW) 73
Figure 4.19 Hourly and Daily state of charge of the Battery System (%) 74
Figure 4.20 Hourly and Daily Inverter output of System Converter (kW) 74
Figure 4.21 Hourly and Daily Rectifier output of System Converter (kW) 74

LIST OF TABLES

Table 3.1	Main Characteristics of Various MPPT Techniques	22
Table 3.	Daily load profiles	62
Table 4.1	System Architecture	70
Table 4.2	PV Plant Statistics	70
Table 4.3	Wind System Statistics	71
Table 4.4	Biomass Plant Statistics	71
Table 4.5	Battery Storage System Statistics	72
Table 4.6	System Converter Statistics	72
Table 4.7	Cost Summary of Each Component of the Hybrid Power Plant over 25 years	75
Table 4.8	Economical Comparison over 25 Years (Each Plant has a capacity of 1MW and under the same load)	76
Table 4.9	Emission Comparison over 25 Years (Each Plant has a capacity of 1MW and under the same load)	76

LIST OF ABBREVIATIONS

TWh	Terawatt Hour
GER22	Global Electricity Review 2022
PV	Photovoltaic
DC	Direct Current
AC	Alternating Current
MPPT	Maximum Power Point Tracking
PMSG	Permanent Magnet Synchronous Generator
P&O	Perturb and Observe
INC	Incremental Conductance
FLC	Fuzzy Logic Control
NNC	Neural Network Control
MT	Mini Turbine
STC	Standard Test Conditions
NREL	National Renewable Energy Laboratory
NOCT	Nominal Operating Cell Temperature
IGBT	Insulated Gate Bipolar Transistor
MOSFET	Metal Oxide Semiconductor Field Effect Transistor
WTG	Wind Turbine Generator
AD	Anaerobic Digestion
COD	Chemical Oxygen Demand
PID	Proportional–Integral–Derivative
LVG	Least Value Gate
TCR	Combustion Reaction Time Delay Constant
TCD	Compressor Discharge Volume Time
TTD	Compressor-Turbine Transport Delay

CHAPTER 1
INTRODUCTION

1.1 Introduction to Renewable Energy

Energy is crucial to the development of nations, and it is ultimately responsible for the industrial and economic growth of any country. It must thus be preserved more effectively. The effective conservation of energy resources should be paid adequate weight. In addition, technology should be developed to produce energy in the most environmentally responsible manner [1]. Since the beginning of the industrial revolution, the dominant source of energy has been fossil fuels [2]. Fossil fuels are non-renewable resources since their regeneration would require millions of years. Renewable resources are those that are abundant in nature, such as wind energy, or can be regenerated rapidly, such as Biomass. Never-before-seen levels of interest in renewable energy research and projects are being shown by a variety of corporations and governments. This is a result of environmental and fossil fuel depletion concerns. This has inspired scholars to develop renewable and clean energy sources to protect the environment and reduce reliance on fossil fuels [3]. Renewables are the fastest-growing form of electricity production, with a predicted annual growth rate of 2.9% between 2012 and 2040, as shown in Figure (1.1) [4].

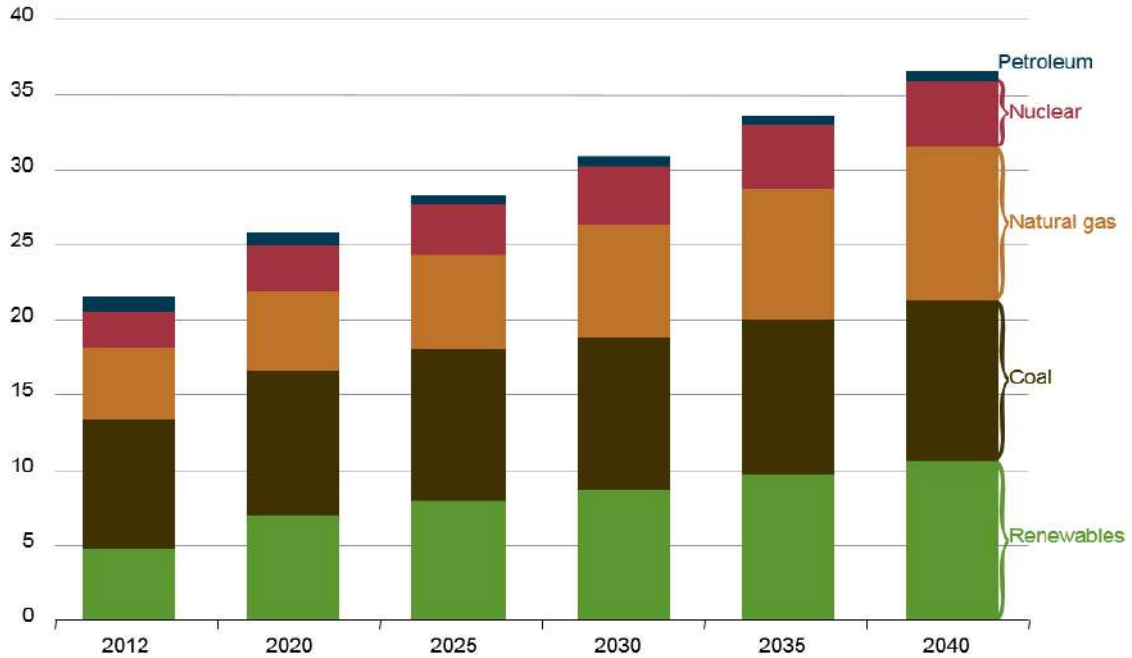

Figure 1.1: Global electricity generation, 2012–2040 (trillion kWh) [4].

Numerous renewable energy sources exist, including hydroelectric, solar, wind, and geothermal energy. From 2012 to 2040, hydroelectric, solar, and wind energy are the renewable energy resources with the most rapid growth, as illustrated in Figure (1.2) [4].

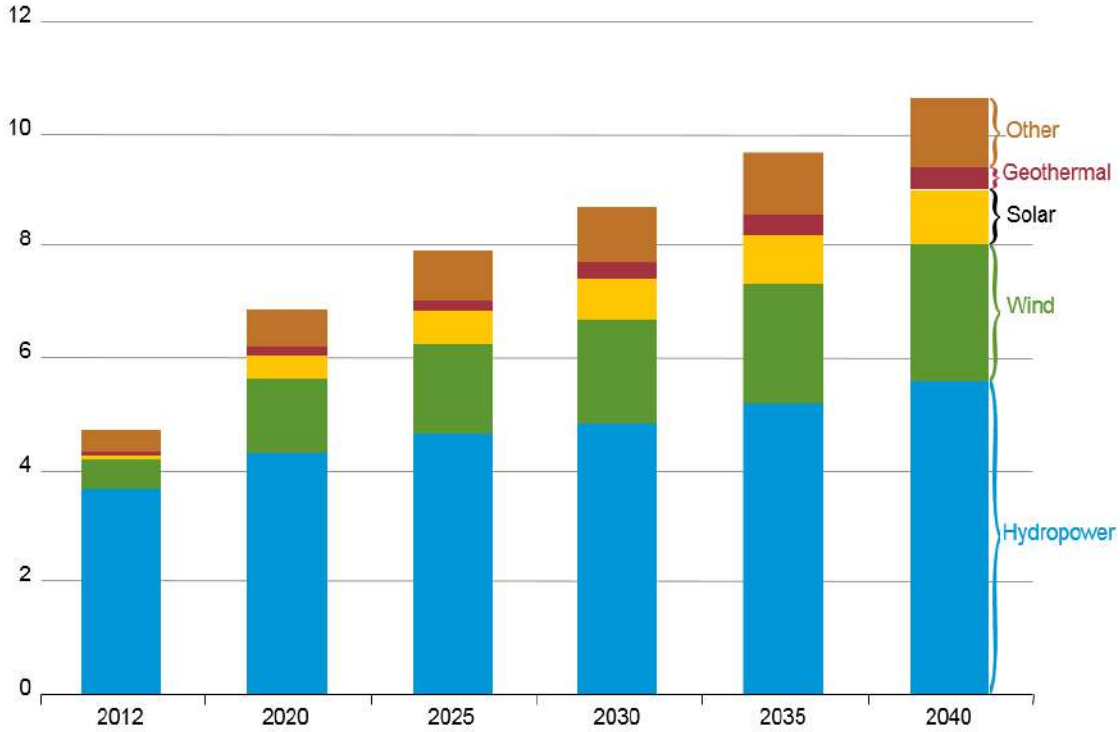

Figure 1.2: Global electricity production from renewable power, 2012–40 [4].

According to the GER22 study, worldwide solar production grew by 23 percent in 2021. It was the fastest-growing source of electricity production for the seventeenth year in a row. To achieve 1023 TWh, yearly production grew by 188 TWh. [5]. In 2021, 3.7% of the world's power was generated by solar energy. This was an increase from the paltry 1.1% in 2015, the year the Paris Agreement was signed [5]. By 2030, solar power production must expand sevenfold, from 4% of the world's electricity in 2021 to 19% of the world's electricity in 2030. This requires maintaining a year-over-year growth rate of 24%; last year's growth rate was 23% and the ten-year average has been 33% [5].

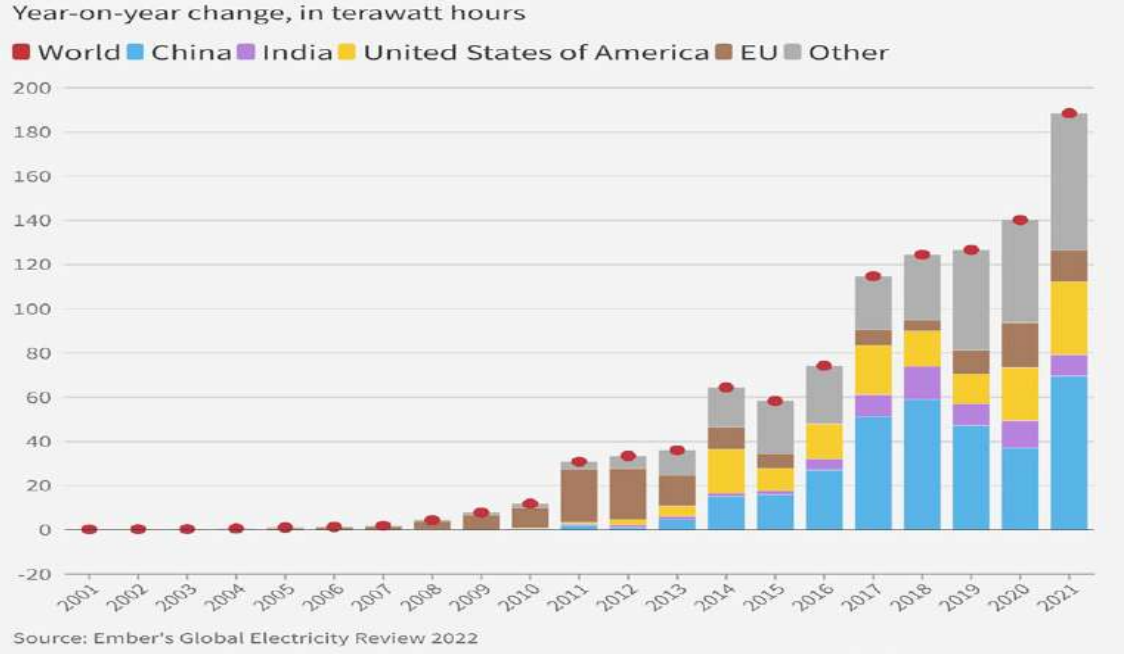

Figure 1.3: Solar PV global year on year change, 2001–2021 [5].

14 percent, or 227 TWh, was added to the quantity of energy generated by wind in 2021, bringing the total to 1,814 TWh [5]. This was both the greatest gain in absolute terms and the highest growth rate during the preceding four years. After solar, it was the second-fastest growing source of power. The proportion of wind-generated power climbed from 3.5% in 2015, the year the Paris Agreement was signed, to 6.6% in 2021 [5].

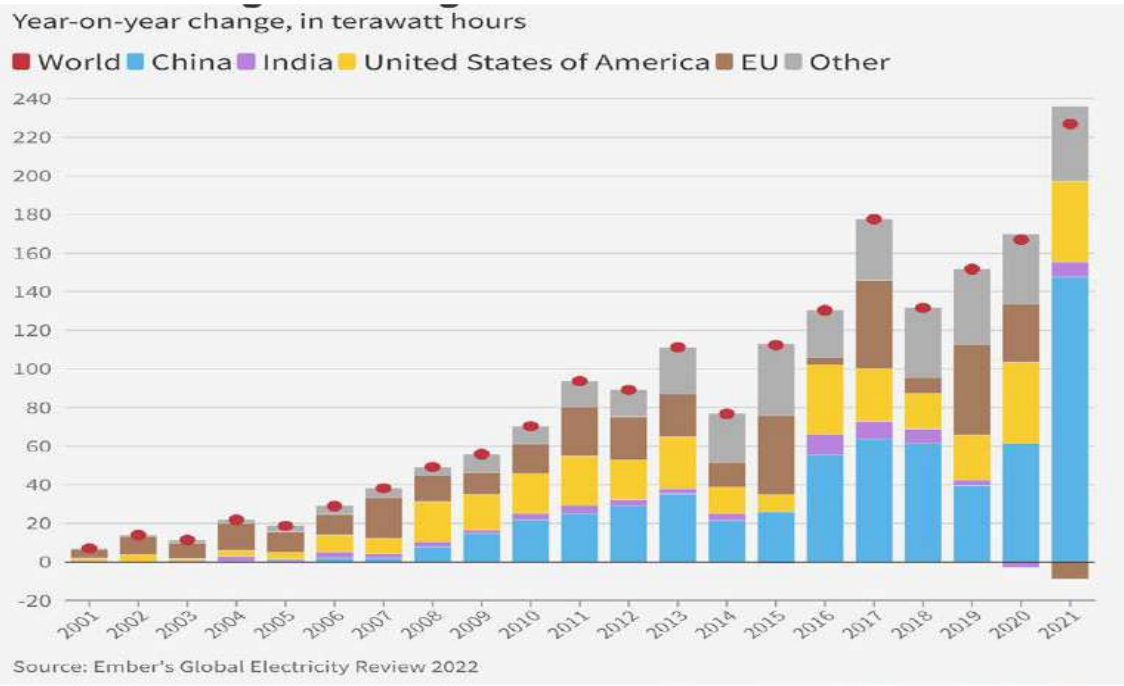

Figure 1.4: The global wind power year on year change, 2001–2021 [5].

In 2021, the worldwide bioenergy production climbed by 6 percent to 646 TWh [5]. Bioenergy statistics are the least reliable of all fuel kinds. Since 2015, the demand for energy as a whole has increased, maintaining bioenergy's share of global generation at about 2%. Wind climbed by almost a ratio of two, from 4 percent to 7 percent, while solar increased from 1 percent to 4 percent [5].

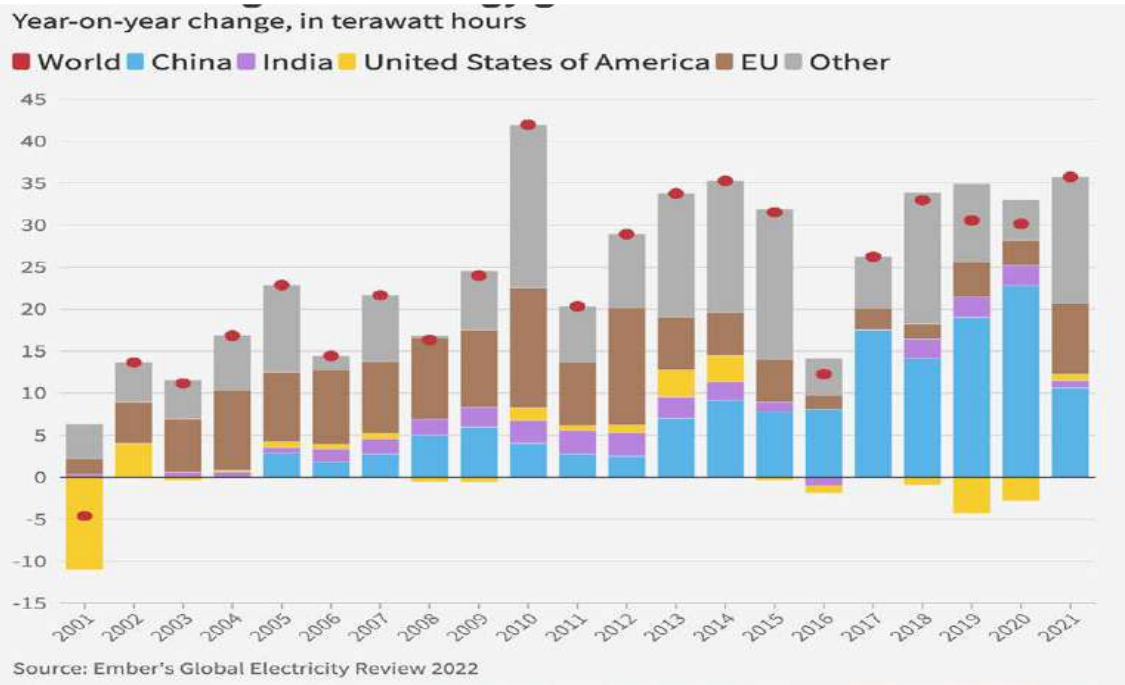

Figure 1.5: Biomass power global year on year change, 2001–2021 [5]

1.2 Introduction to Hybrid Renewable Energy System

A hybrid renewable energy system combines two or more renewable energy resources with a control system, allowing the system to provide the required quality of electricity [6]. Solar and wind energy sources exhibit unpredictability and randomness. Because solar radiation levels are regulated by environmental and climatic variables such as temperature and clouds, solar energy is unreliable [7]. Although wind may provide significant amounts of energy, it is very unpredictable. Consequently, wind energy is sometimes seen as unreliable. Renewable energy systems may be made more stable and reliable with the help of energy storage devices. Consequently, a hybrid system including solar PV, a wind turbine, a biomass generator, and a battery storage system is often more dependable than wind or solar PV systems alone [8].

This study models, studies, and simulates a hybrid solar PV/wind/Biomass power system with a battery storage system. When the solar photovoltaic or wind system is turned off, the Biomass system and the battery may provide the load with electricity. The hybrid system's block diagram is illustrated in Figure (1.5).

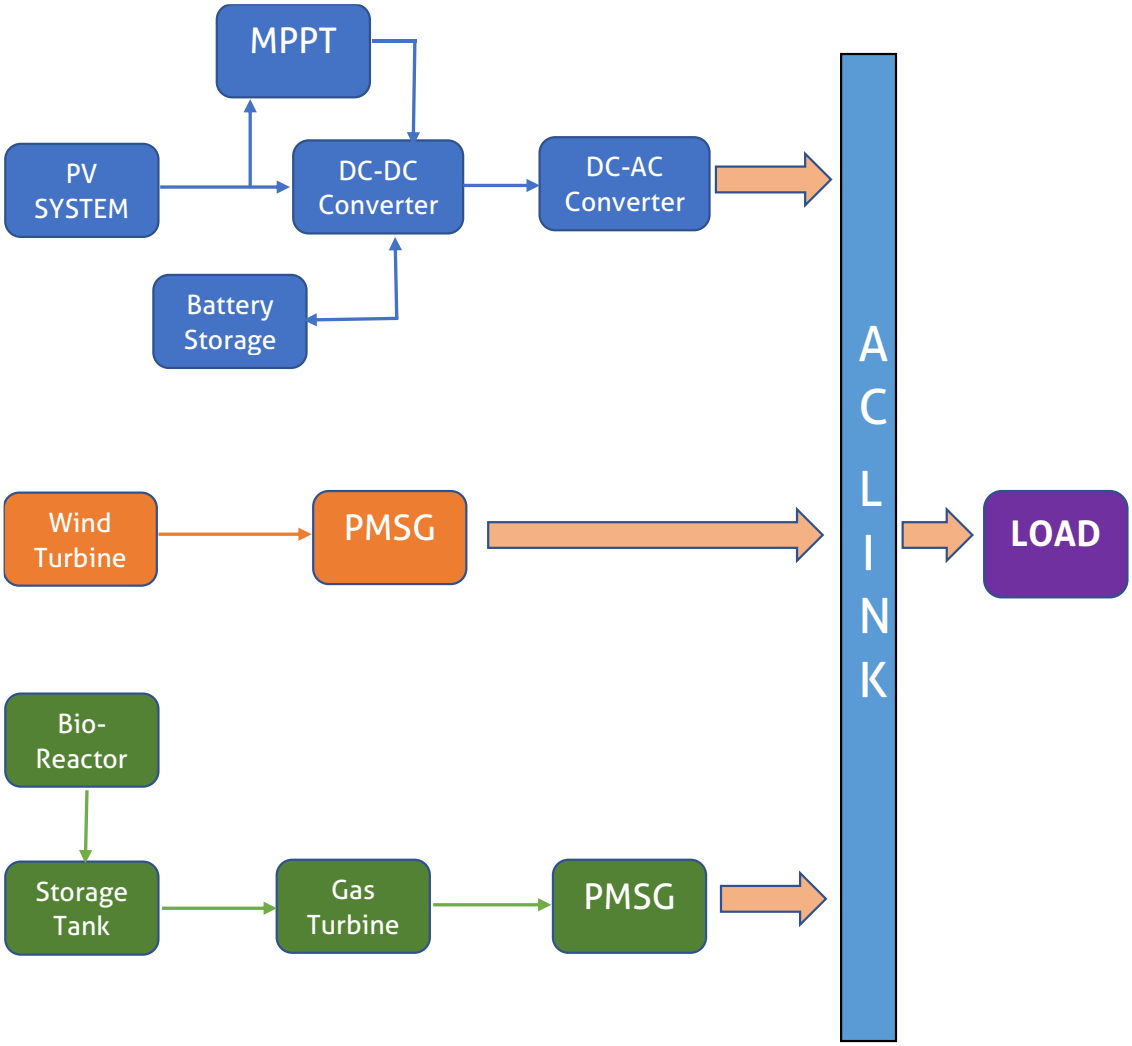

Figure 1.6: Block diagram of the proposed hybrid system.

1.3 Objective

Our objective is:

- To design and simulate in MATLAB-Simulink a Standalone Hybrid PV-Wind-Biomass power system with battery storage.
- To assess the Energy Load for the selected Sandwip, Chittagong area.
- To examine and analyze the sustainable power potential mainly for the three resources- Biomass, Solar, and Wind.

- To design a PV-Wind-Biomass hybrid structure at an appropriate place within the aforementioned territory using HOMER Pro.
- Analysis of the economic and environmental effects of the hybrid power production system using HOMER Pro.

1.4 Thesis Outline

In five chapters of this thesis, we detail and analyze our study. These are the outlines of our thesis:

Introduction may be found in Chapter 1. This chapter discusses the introduction of the thesis subject.

The second chapter is a literature review. This chapter discusses all past works pertaining to this dissertation.

The development of the Hybrid Microgrid using MATLAB/Simulink is explained in the third chapter's methodology section.

Chapter 4 is devoted to the discussion of our dissertation's findings.

Chapter 5 concludes with a discussion of conclusion and future endeavors.

1.5 Summary

MATLAB/Simulink and HOMER Pro simulations revealed that this model had a lower "Net Present Cost" than oil-based power plants but a slightly higher "Net Present Cost" than natural gas-based power plants. Despite this, the initial Capital expenditures for the hybrid power plant are much higher. Compared to Natural gas-based power plants and Oil-based power plants, the Hybrid power plant has much less hazardous emissions. It may be inferred that employing a hybrid PV-Wind-Biomass turbine system with a battery storage system is more efficient and dependable than using a PV, Biomass, or Wind power system individually. Considering the entire cost and the substantial decrease in environmental emissions, it may also be a better option than installing a fossil fuel-based power plant.

CHAPTER 2
LITERATURE REVIEW

2.1 Introduction

Due to the rising demand for energy and the limited availability of conventional fossil fuel energy sources, research into renewable energy sources has accelerated. As a consequence, countless research papers have been published in an effort to improve the efficiency and reliability of renewable energy sources.

- Modelling and simulating a 36W PV module with variable temperature and irradiance is shown in [8]. Two separate MPPT approaches have been employed: incremental conductance (INC) and perturbation and observation (P&O). Compared to the incremental conductance method, the P&O approach uses less hardware and is easier to implement. However, the progressive conductance approach seldom produces any extra power loss.
- [9] explains the design, modelling, and assessment of an intelligent controller that maximizes the power delivered by sources to manage the power flow between a PV-wind hybrid power system and an energy storage system. To achieve the MPP for PV modules, the perturb and observe (P&O) approach is compared with a neural controller (NNC). With the NNC, the PV system may reach its maximum power point faster and with fewer variations under steady-state circumstances.
- In the work [10], P&O, incremental conductance, and FLC MPPT techniques for solar applications are addressed. By modifying the standard P&O and incremental conductance approaches, the hill-climbing controller is able to track the maximum power point under variable irradiance. Due to the nonlinearity of the curve of the maximum power point voltage, it also modifies the reference voltage rise to meet the operating point. The modified P&O, incremental conductance, and fuzzy logic control performances are compared based on the results of the efficiency tests, and the efficiency is around 99.4%. This research concludes that the performance of the modified hill-climbing algorithms is better to that of the fuzzy logic control (FLC).
- The methods involved in battery charging and discharging are analyzed in [11]'s examination of several bidirectional converter types and battery charging and discharging procedures. After evaluating the different characteristics of non-

isolated bidirectional converter topologies, it was found that the non-isolated bidirectional half-bridge DC-DC converter may be the best option for hybrid system applications.

- In [42], a comprehensive modelling and simulation of a biomass-fueled power system is described. The model may be used for simulation and analysis in both steady-state and transient states, and it explains the dynamics of an MT.

2.2 PV Overview

2.2.1 PV Cell Overview

2.2.1.1 The Difference Between PV Cell, Module, and Array

A photovoltaic cell is considered to be the fundamental element of a solar PV system. Due to limitations on surface area, the quantity of power produced by a PV cell is normally limited to a few watts. Therefore, PV cells are joined in parallel or series to make a PV module. Moreover, PV modules may be linked in series, parallel, or both, depending on the required current and voltage [6]. The structure of a PV cell, module, and array is shown in Figure (2.1).

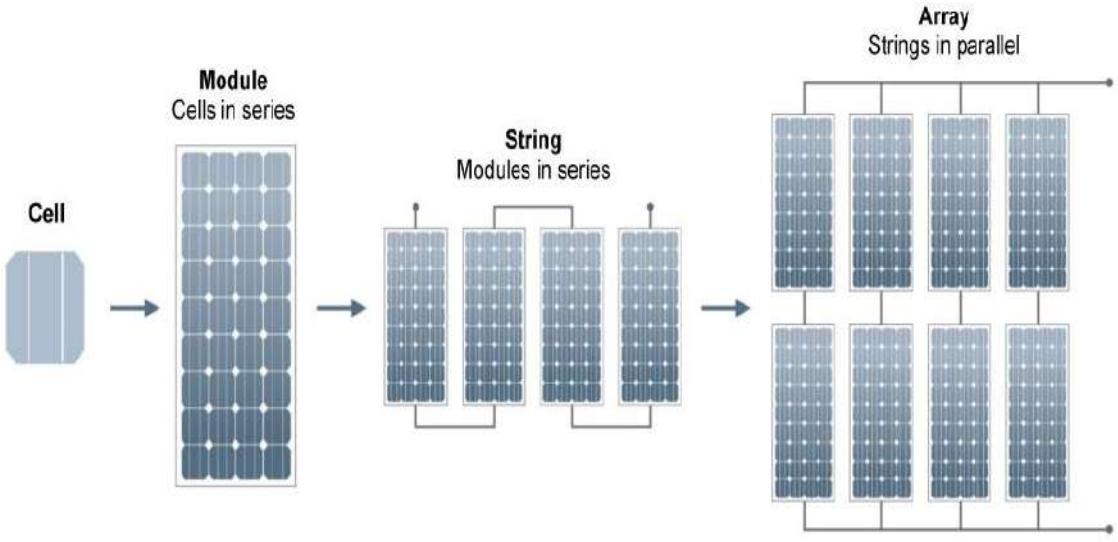

Figure 2.1: Structures of PV devices.

2.2.1.1.1 PV Cell

A photovoltaic (PV) cell is a photodiode made of semiconductor p-n junction material that can convert radiation from the sun energy directly into electrical energy. Several

varieties of semiconducting materials are employed in the fabrication of PV cells, with silicon being the most prevalent. PV cells are linked in series to provide a high voltage and in parallel to enhance the current. Under Standard Test Conditions (STC), a single PV cell generates roughly 1.5W at a voltage between 0.5 and 0.6V [17].

2.2.1.1.2 PV Module

As indicated in the Figure (2.1), a PV module, also known as a panel, is a cluster of cells linked in parallel or series (often 36 or 72) to create increased power and voltage. In a series connection, the voltage of the photovoltaic module is equal to the sum of the voltages of each PV cell, and the current of each PV cell is same. In contrast, in a parallel arrangement, the output voltage of the solar module will be equivalent to the voltage of a single PV cell, and the current will equal the sum of the currents of each PV cell [13].

2.2.1.1.3 PV Array

A PV array is composed of a series and/or parallel connection of many solar modules. In trading applications, the output power of a single module is inadequate to provide the necessary power, thus PV modules are connected in series or parallel to create extra power. The combination of PV modules is comparable to PV cells attached to a single module. They are connected in parallel to raise the output current and in series to boost the output voltage [7].

2.2.1.2 Working Principle of PV Cell

The photoelectric effect is crucial to the functioning of a PV cell. This impact may be described as follows: When a photon of solar radiation hits a photovoltaic cell, the electrons in the semiconductor get excited and leap from the highest-energy valence band to the unbound conduction band. Due to the electric field, these electrons follow a certain route. Positive and negative terminals and a voltage between the terminals are generated by electron mobility. When an external circuit is connected to these terminals [7], direct current (DC) flows across the circuit. The whole conversion process is represented in Figure (2.2) [9].

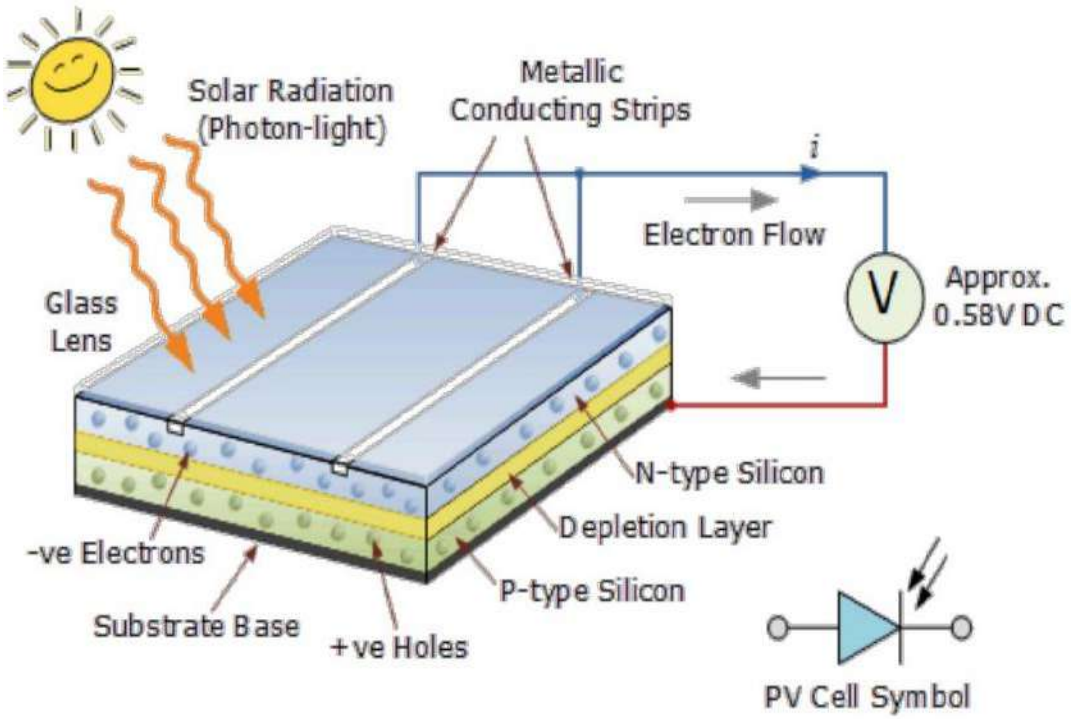

Figure 2.2: Working principle of PV cell.

2.2.1.3 PV Cell Technologies

Numerous technologies exist in the PV industry; however, they may typically be categorized into three generations depending on the kind of material utilised and marketing strategies. First-generation photovoltaic cells use single-crystalline and polycrystalline (multicrystalline) silicon wafer-based material types [18]; they are crystalline silicon wafer-based material types. In the early 1980s [19], the thin-film technology employed by the second generation of PV cells was created. Among the photovoltaic cells of the third generation are organic photovoltaic cells, perovskite photovoltaic cells, and multijunction concentrator PV cells. Due to the ongoing development of these technologies, they have not yet been widely marketed [18]. Figure (2.3) illustrates a timeline of photovoltaic technologies' solar cell energy conversion efficiencies.

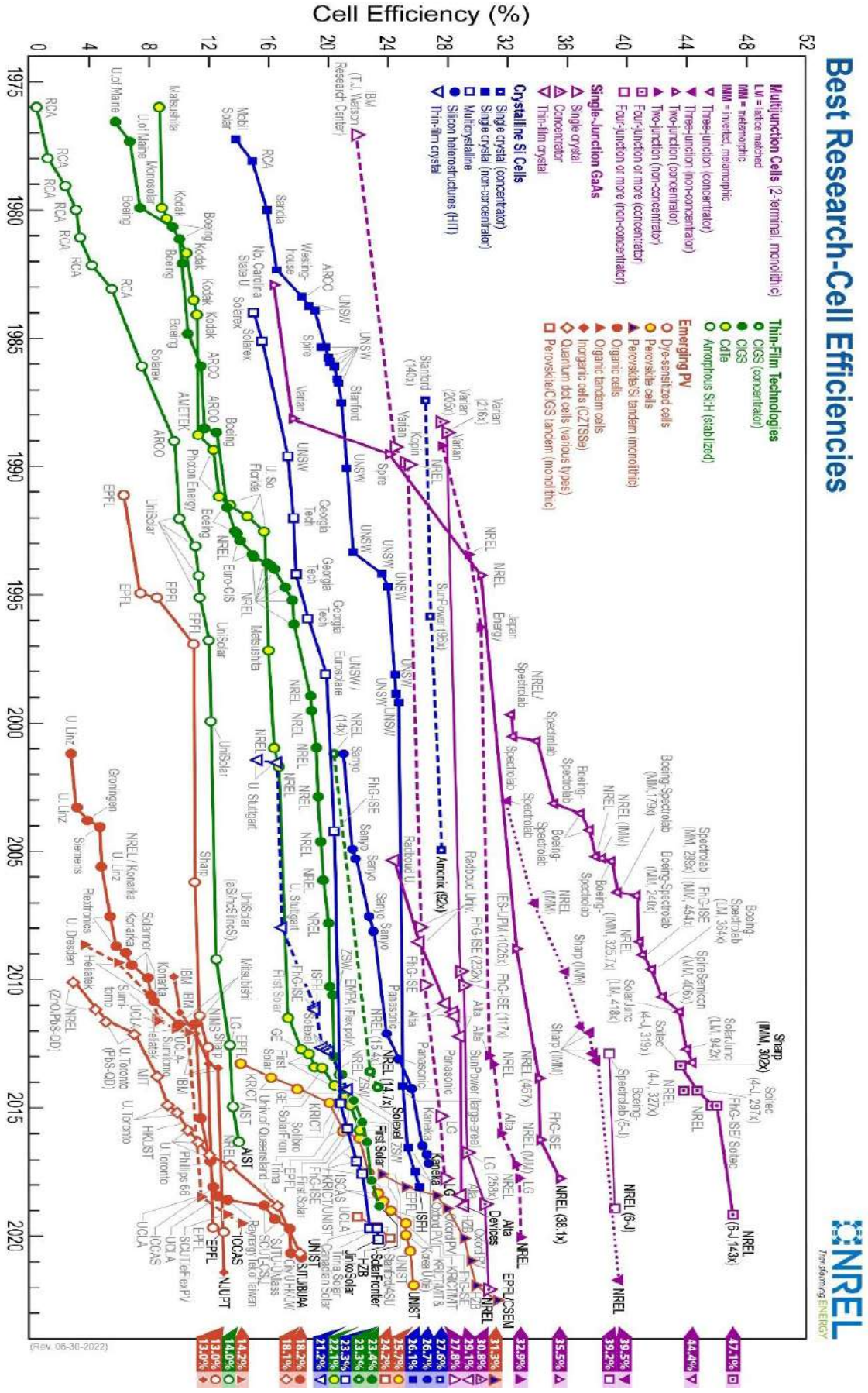

Figure 2.3: Timeline of PV cell energy conversion efficiencies from NREL [20].

2.3 Wind Overview

Wind is the natural movement of air volumes, whose attributes are determined by its velocity and direction. Variations in air pressure resulting from solar heating of various parts of the Earth's surface create this movement. Therefore, wind may be seen as an indirect kind of solar energy. Despite the fact that air flows both horizontally and vertically, only the horizontal movement is considered wind energy [35].

Wind turbines are instruments that gather wind energy and are classified based on the orientation of their axes with respect to the wind flow. The two most common types of wind turbines are those with horizontal and vertical axis. Horizontal-axis turbines are used most commonly in both large-scale and small-scale energy generating [35]. A wind turbine's primary function is to create electricity from the mechanical impact caused by the kinetic energy of the wind, which may either be supplied to the electric grid or used to power a load. A wind turbine is composed of a tower, rotor blades that spin around a hub, and a gearbox located in the nacelle. The essential wind turbine system components are explained in Figure (2.4).

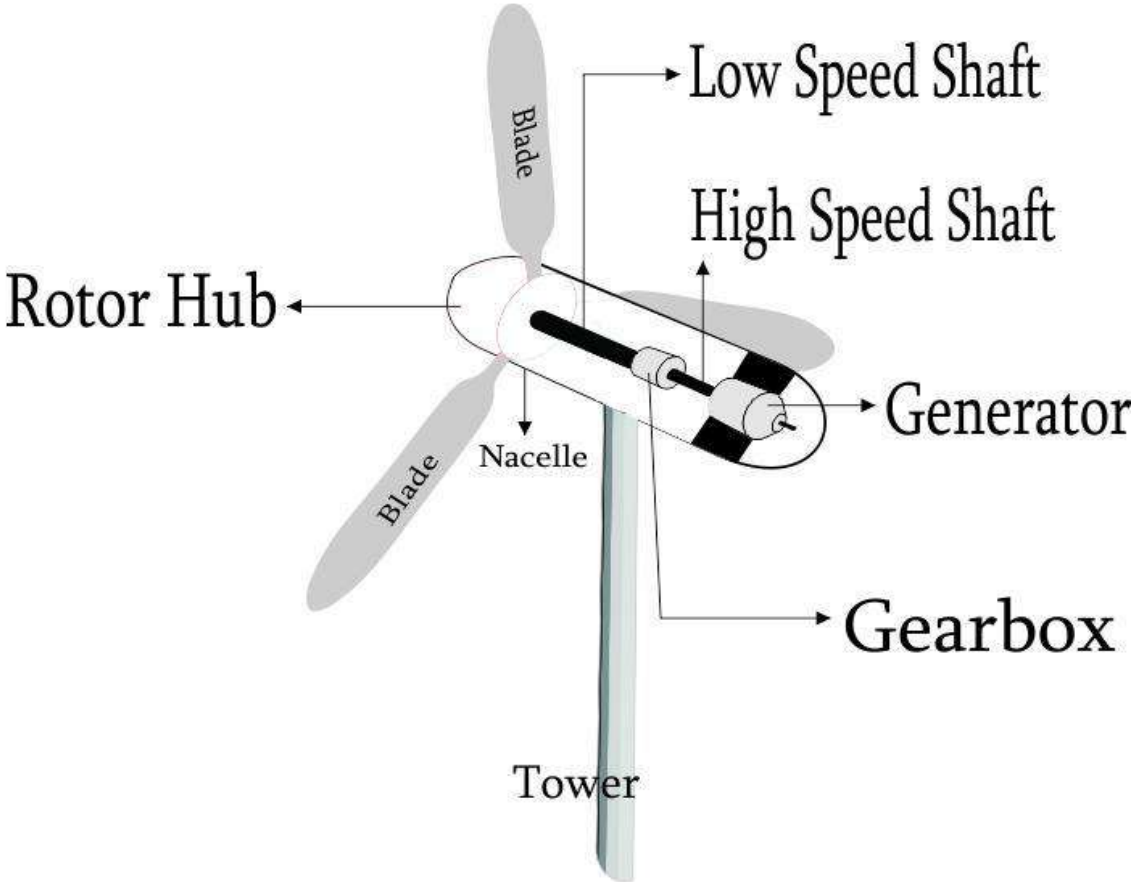

Figure 2.4: Basic components of horizontal-axis wind turbines.

2.4 Biomass Overview

2.4.1 Bio-Reactor

A bioreactor is a crucial component of the microbial conversion process because it provides a suitable, stable environment for microbial growth and metabolism by controlling operating parameters. The performance of bioreactors is greatly affected by various other aspects, including the structure and size of the bioreactor, its mixing and transfer properties, and the methods of feed entry and product removal. Complex multiphase flow patterns occur in bioreactors, which may affect the heat and mass transport characteristics and impact microbial conversion processes [43].

Numerous techniques exist for turning biomass into usable energy. In certain aspects, the conversion process relies on the particular characteristics of the biomass, such as its moisture and ash content. The energy content of the biomass source effects the conversion process in several ways. Important among these transformation processes is anaerobic digestion (AD), in which biogas is created from biomass sources [44]. During the fermentation process, anaerobic digesters may consume various biomasses, such as agricultural residues, animal manure, and food waste. Numerous researchers have investigated several aspects of biogas production, treatment, and use [45].

2.4.2 Anaerobic digestion process

AD is a biochemical conversion process carried out by many microorganisms in which organic biomass is turned to organic acids, which are further converted to methane gas and carbon dioxide. Extremely harsh anaerobic conditions are present throughout the process (no oxygen). Normal anaerobic treatment eradicates Chemical Oxygen Demand (COD) by converting organics to methane. Consequently, the COD of the methane generated in an anaerobic system is typically comparable to the COD that is removed. The whole method consists of the four different occurrences and four separate steps listed below:

2.4.2.1 Hydrolysis

Extracellular enzymes of hydrolytic bacteria turn insoluble, complex biomass into soluble molecules by Hydrolysis. These microbes degrade biomass into simpler

compounds before any others. Transformation of carbohydrates, lipids, and proteins into glucose, fatty acids, and ammonia acids. At the end of the hydrolysis process, complex organic molecules are converted predominantly into volatile fatty acids [46].

2.4.2.2 Acidogenesis

In the second phase, hydrolysis-derived soluble organics are transformed into short-chain fatty acids and alcohols. Through the acetic acid conversion process, the majority of acids are changed into acetic acid. Other organic acids, like propionic, butyric, and valeric, are produced as well. During this phase, hydrogen is produced by the fermentation of glucose. These organisms are known as "acid formers" and include homoacetogenic and facultative bacteria. This step comprises the transformation of acetic acid and water into carbon dioxide and hydrogen.

2.4.2.3 Acetogenesis

This acetogenesis stage is an advanced step of the acidification stage; at this stage, roughly 79% of COD is converted to acetic acid. The formation of acetate is dependent on the oxidation conditions of organic substances, which are often accompanied by the generation of CO_2 and hydrogen. Acetogenic bacteria create acetic acid by converting ethanol, butyric acid, and lactic acid to acetic acid [47]. This step represents the extensive hydrogenation of acetic acid. During the process of dehydrogenation, acetic acid may also be generated. Besides numerous fatty acids, acetic acids are the most abundant organic acids produced by the AD process.

2.4.2.4 Methanogenesis

In this phase of methanogenesis, methane and CO_2 are produced. Methane is produced by acetotropic and hydrogenotrophic bacteria by the breakdown of carbon dioxide with hydrogen. The atmosphere is appropriate for methane-producing bacteria due to the process of acid-producing bacteria. Methane-producing bacteria will use this acid to make acid-forming bacteria. At this point, methanogenetic bacteria transform low-molecular-weight compounds into molecules with a high molecular weight.

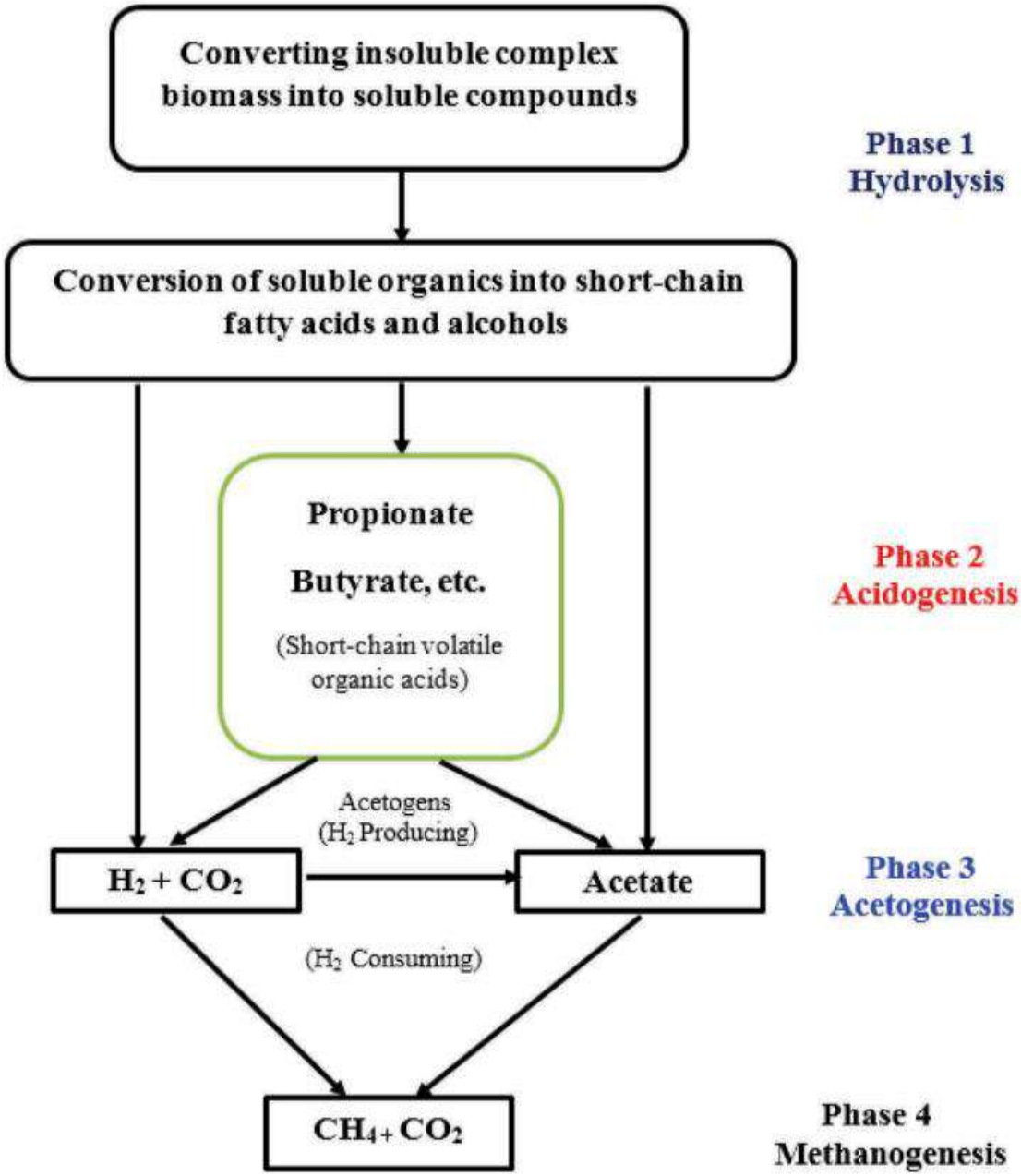

Figure 2.5: A schematic diagram of the four stages of AD process.

CHAPTER 3
METHODOLOGY

3.1 PHOTOVOLTAIC ENERGY SYSTEM

3.1.1 Modelling of the PV System

PV system consists of a photovoltaic array that converts solar radiation to electricity, a DC-DC buck-boost converter, and a maximum power point tracking (MPPT) control system to achieve the maximum power point (MPPT). Figure (3.1) depicts the block diagram of the proposed PV system.

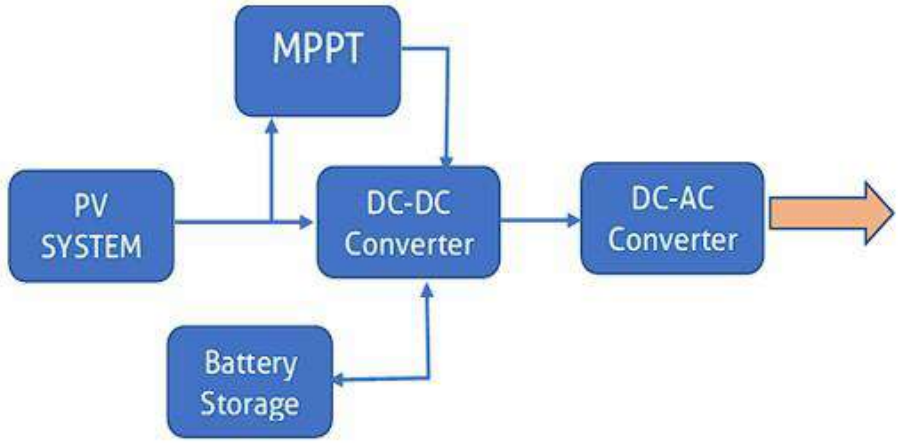

Figure 3.1: The proposed PV system.

3.1.1.1 Ideal PV Cell

Figure (3.5) illustrates the electrical circuit of an ideal PV cell in order to describe the study of perfect PV cells in electrical circuits [12]. This circuit may be approximated by a radiation- and temperature-dependent current source in parallel with an ideal diode with its terminals reversed. The following equation may be used to hypothetically define the perfect PV cell [21].:

$$I = I_{pv} - I_0\,[\exp(\frac{qV}{\alpha kT}) - 1] \qquad \ldots(2)$$

Where:

- I_{pv} is the current produced by solar radiation (A).
- I_0 is the leakage current (A).
- V is a cell voltage (V).
- q is the electron charge which is approximately equal to (1.602×10-19 C).

- α is the diode ideality factor.
- T is temperature, in Kelvin (K).
- k is the Boltzmann constant which is (1.3807×10-23 J/K) [12].

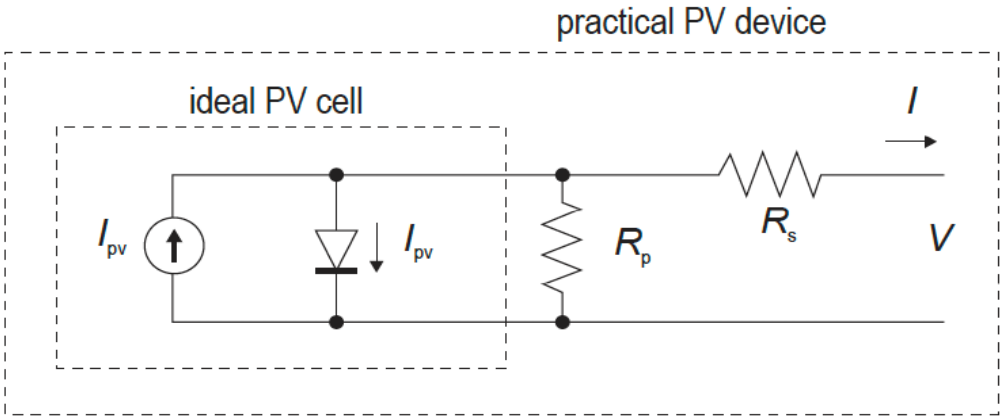

Figure 3.2: The electrical circuit of a single-diode PV cell [12].

The equation of the Shockley diode current (I_D), which is the equation (3), is equal to the second part of the equation (2), and the I-V characteristic curve of a PV cell describes this equation in Figure 3.6).

$$I_D = I_0\,[\exp\,(\frac{qV}{\alpha kT}) - 1] \qquad \ldots(3)$$

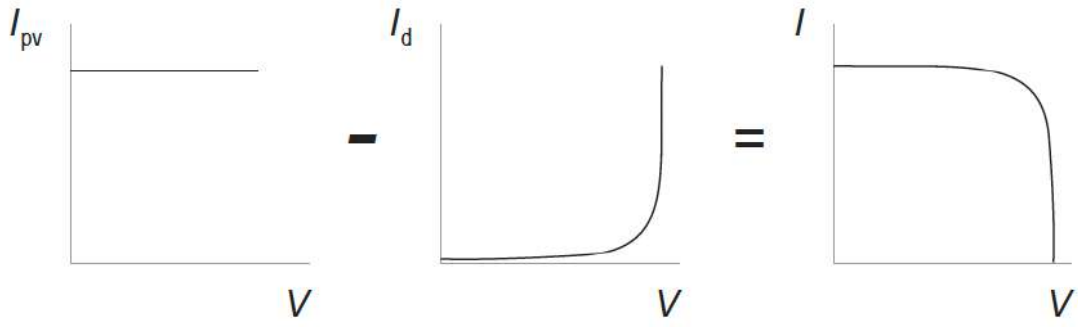

Figure 3.3: The characteristic I-V curve of a PV cell [21].

3.1.1.2 Modelling of PV Array

Typically, the PV cell or module is represented by the single-diode or double exponential model Figure 3.5). The double exponential model contains an additional diode in parallel. This model is more difficult to solve than the one with a single diode, but it is better. Therefore, the single-diode model is often used because it strikes an ideal compromise between simplicity and efficiency [22]. The ideal photovoltaic cell model may be stated theoretically using a current source with an inverted diode; however, parallel and series

resistors are added to make the circuit more practical, as detailed in Figure 3.5). The series resistance is created due to the metal contacts and restriction in the direction of the electron stream from the N to P junction. The series resistance is a crucial characteristic since it affects the maximum output power and short-circuit current of the solar cell. Parallel resistance (R_P) or shunt resistance characterizes the loss caused by surface leakage current or manufacturing defects [23]. Consequently, the following equation [7] is used to represent the current as a function of voltage and other pertinent factors:

$$I = I_{pv} - I_0 \left[\exp\left(\frac{V+IR_S}{\alpha V_T}\right) - 1\right] - \left[\frac{V+IR_S}{R_P}\right] \quad \ldots(4)$$

Where:

- I_{pv} is the photocurrent (A).
- I_0 is the reverse saturation current (A).
- V is the voltage across the diode (V).
- α is the diode ideality factor.
- V_T is the thermal voltage (V).
- R_S is the equivalent series resistance (Ω).
- R_P is the equivalent parallel resistance (Ω).

The following equation illustrates the factors that affect the photocurrent of a photovoltaic cell:

$$I_{pv} = (I_{PV,STC} + K_1 \Delta T)\left(\frac{G}{G_{STC}}\right) \quad \ldots(5)$$

Where:

- $I_{PV,STC}$ is the generated current under STC (A).
- K_1 is the short-circuit current's temperature coefficient.
- G is solar radiation (W/m2).
- G_{STC} is the solar radiation under STC (1000 W/m2).

The following equation illustrates the impact of temperature on the reverse saturation current [9]:

$$I_0 = I_{0,STC}\left(\frac{T_{STC}}{T}\right)^3 \exp\left[\left(\frac{q\,E_g}{\alpha K}\right)\left(\frac{1}{T_{STC}} - \frac{1}{T}\right)\right] \quad \ldots(6)$$

Where:

- $I_{0,STC}$ is the nominal saturation current at STC.
- T_{STC} is the temperature at STC.

- E_g is the energy of the band gap in semiconductors.

Also, by modifying the above equations, the reverse saturation current would be as [24]:

$$I_0 = \frac{I_{SC,STC}+K_1\Delta T}{\exp\left[\left(\frac{(V_{OC,STC}+K_v\Delta T}{\alpha V_T}\right)\right]-1} \quad \ldots(7)$$

Where:

- $I_{SC,STC}$ is the short-circuit current at STC.
- $V_{OC,STC}$ is the open-circuit voltage at STC.
- K_v is the open-circuit voltage's temperature coefficient.

So, the output current equation of the photovoltaic array is represented as:

$$I = I_{PV}N_P - I_0N_P \left[\exp\left(\frac{V+IR_S\left(\frac{N_S}{N_P}\right)}{\alpha V_T N_S}\right) - 1\right] - \left[\frac{V+IR_S\left(\frac{N_S}{N_P}\right)}{R_P\left(\frac{N_S}{N_P}\right)}\right] \quad \ldots(8)$$

Where, N_P is the total cells that are connected in parallel and N_S is the total cells that are connected in series.

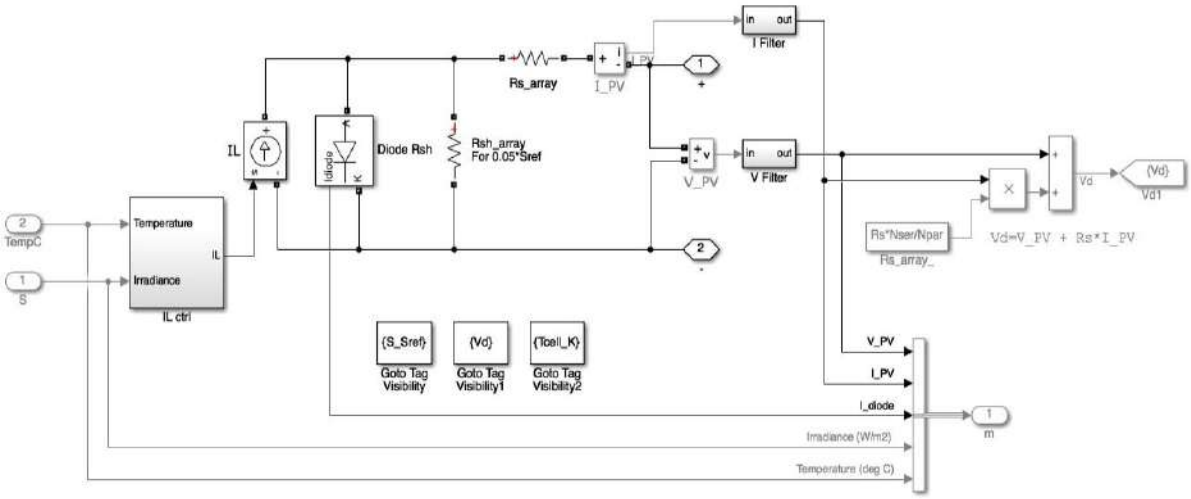

Figure 3.4: The Simulink model of the PV array.

3.1.1.3 PV Characteristics

Numerous PV cells are integrated to provide enough output power. The array's characteristics are represented by multiplying the current by the total number of parallel PV cells and the voltage of a single PV cell by the total number of series PV cells. I-V and P-V characteristics of actual photovoltaic devices vary across types [25]. As seen in Figure (3.5), three points on the characteristic curve of a PV device are considered crucial: the short-circuit, open-circuit, and maximum power points [13].

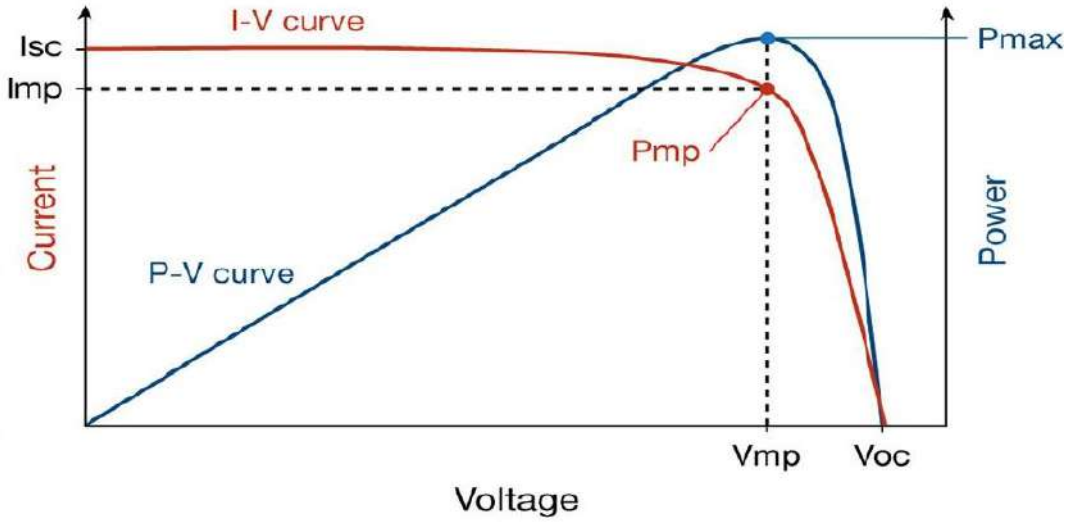

Figure 3.5: I-V and P-V characteristic curves.

All manufacturers of PV devices give datasheets for their products. The datasheets give experimentally derived information on the electrical characteristics of PV devices. The following data might be obtained on the datasheets of PV devices [26]:

- Nominal short-circuit current ($I_{SC,N}$).
- Nominal open-circuit voltage ($V_{OC,N}$).
- Current at the MPP (I_{MP}).
- Voltage at the MPP (V_{MP}).
- Temperature coefficient of short-circuit current (K_I).
- Temperature coefficient of open-circuit voltage (K_{IV}).
- Experimental maximum power ($P_{MAX,E}$).

Always accompanying experimental data are STC or NOCT references. On occasion, PV device makers assist the modification of the mathematical P-V and I-V equations by supplying P-V and I-V curves for varying temperature and irradiance circumstances [12].

Another crucial element of PV is the fill factor (FF). As seen in Figure (3.6), the fill factor measures the squareness of the I-V curve and is given as the ratio of two regions. In addition, it offers an indicator of the performance of the semiconductor in the solar cell. Any restriction that diminishes the fill factor also diminishes output power by reducing (I_{MP}), (V_{MP}), or both. Fill factor is less than 1 and is material-dependent [13]. When the fill factor is near to 1, the photovoltaic array may produce more power. As shown in

Figure (3.9), the fill factor is derived by dividing the shadow area by the hatching area, and it is represented by the following equation [13]:

$$FF = \frac{P_{MP}}{V_{OC}I_{OC}} = \frac{V_{MP}I_{MP}}{V_{OC}I_{OC}} \quad \ldots(9)$$

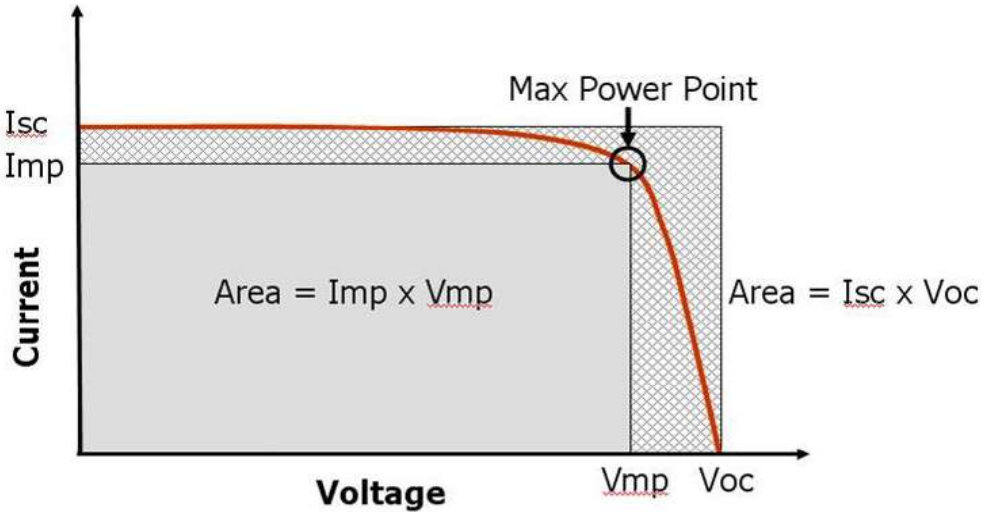

Figure 3.6: PV module characteristics showing the fill factor.

3.1.1.4 Factors Affecting PV Characteristic Curves

3.1.1.4.1 The Effect of Solar Radiation Variations

The PV parameters (I-V and P-V parameters) are strongly reliant on solar irradiation because the short-circuit current is greatly dependent on solar irradiation and grows proportionally as irradiation increases. As solar irradiation rises, the change in open-circuit voltage (V_{OC}) is minimal, as seen in Figures (3.7) and (3.8). Consequently, the amount of solar radiation will fluctuate in reaction to any change in environmental circumstances, causing the output power value to grow or decrease. Consequently, maximum power point tracking (MPPT) methods are used to ensure constant maximum power. [6].

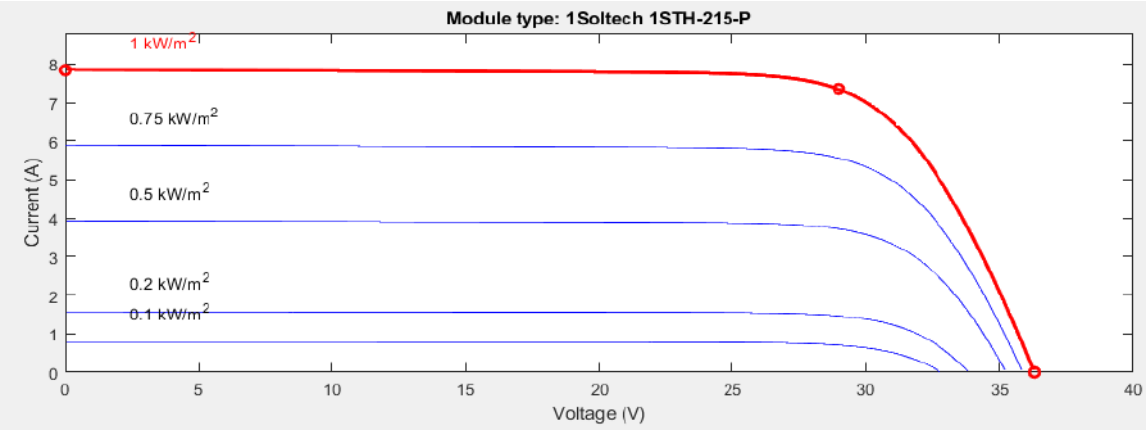

Figure 3.7: I-V characteristics with different irradiance for the PV array.

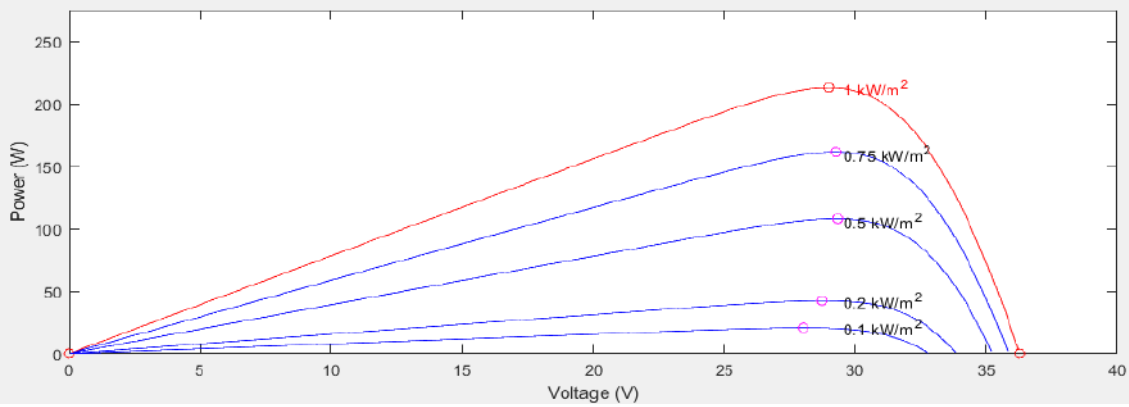

Figure 3.8: P-V characteristics with different irradiance for the PV array.

3.1.1.4.2 The Effect of Temperature Variations

Temperature also effects the photovoltaic characteristics. The short-circuit current increases somewhat as the internal temperature of the solar cell rises. Nevertheless, the open-circuit voltage is significantly impacted by temperature. Figure (3.9) depicts the influence of temperature on photovoltaic characteristics [6]. In the field, under sunny conditions, the PV cell's internal temperature is often elevated, resulting in a drop in efficiency [27].

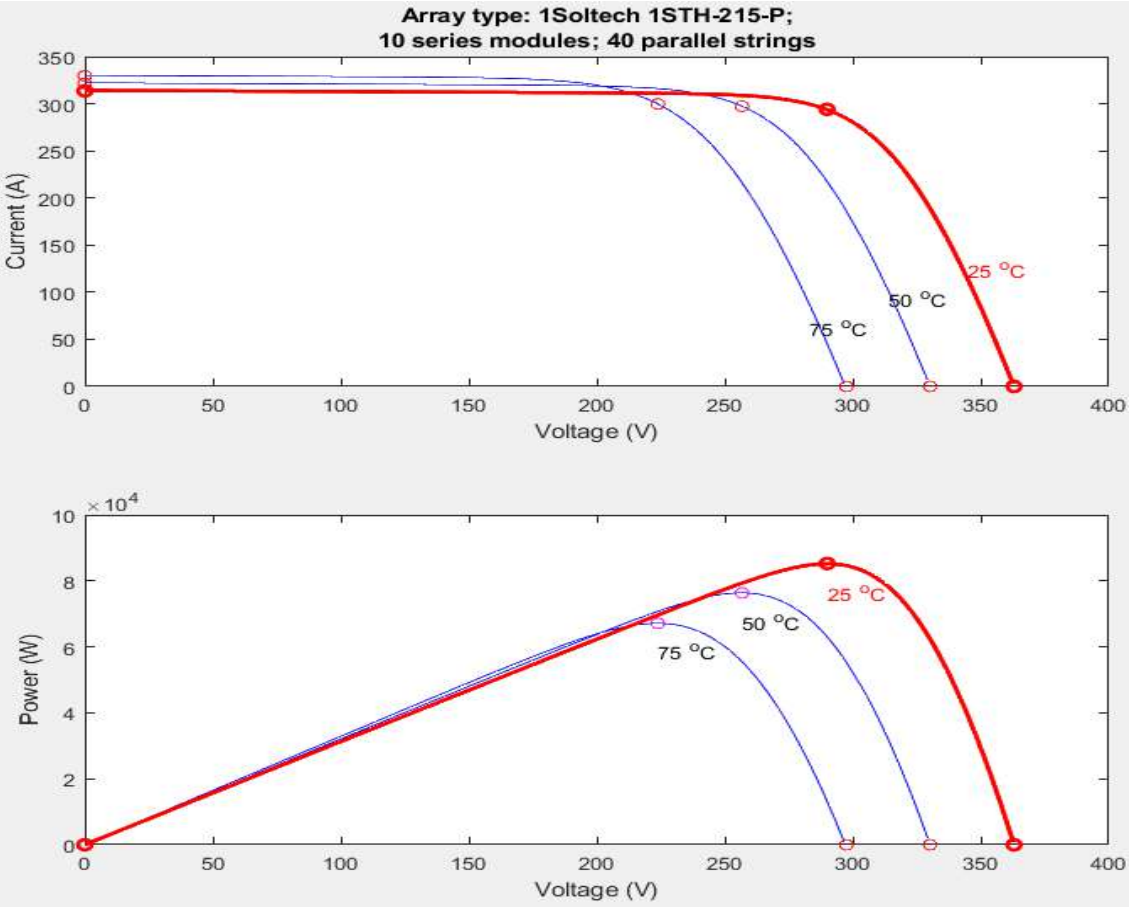

Figure 3.9: Temperature effect on the PV characteristics.

3.1.1.4.3 The Effect of Shading

One of the most critical factors that might impact the effectiveness of a solar system is shading. Shading is the casting of a shadow on the outside surface of PV devices, which decreases the system's power output. A solar device generates less voltage or current while it is in the shade. When PV devices are linked in series, the same current will flow through the circuit, however the shaded region is incapable of producing the same current. When PV devices are linked in series, the shaded region operates as a load and consumes energy. This problem may result in system damage. As seen in the block diagram of a darkened PV array in Figure (3.10), the bypass diode is used to limit the damage under these conditions. [7].

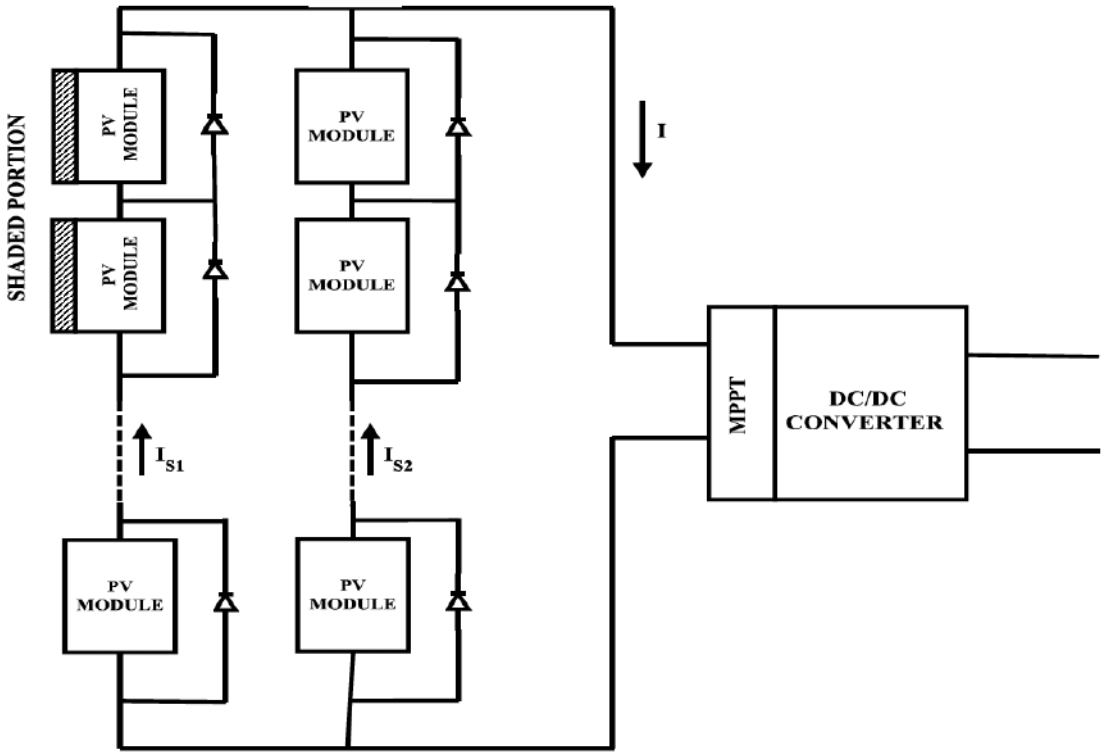

Figure 3.10: A PV array in shaded condition.

In the presence of partial or complete shadow, photovoltaic (PV) parameters become more nonlinear, with a greater number of maximum power points. Under these conditions, the MPPT becomes a challenging endeavor. The influence of shadow on PV parameters (P-V and I-V) may be seen in Figure (3.11) [7].

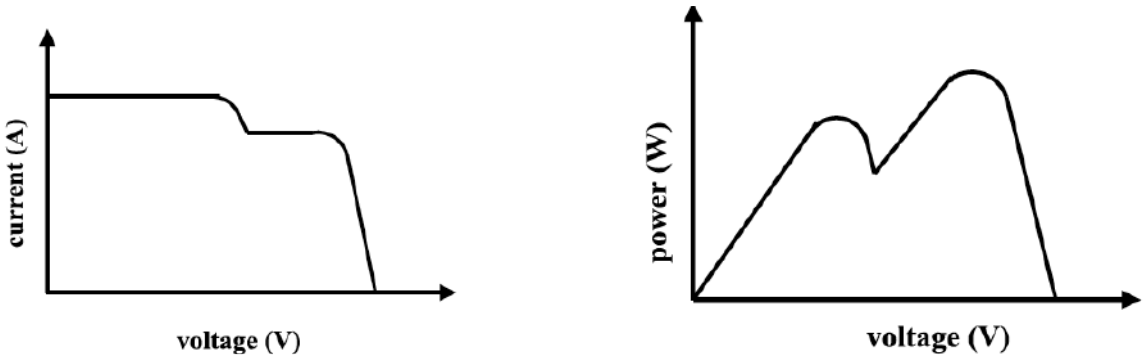

Figure 3.11: The effect of shading on I-V and P-V characteristics.

3.1.2 Maximum Power Point Tracking of a PV System

Tracking the maximum power point (MPP) of a PV array is an essential component of a PV system. It is an electrical control system that can harvest the maximum amount of energy from a solar system. MPPT is not a mechanical technique that alters the orientation of PV arrays mechanically to face the sun directly. It is a fully electronic system that can achieve MPPT by altering the PV arrays' operating point [27]. Typically, a PV module converts around 40% of the incident solar energy into electricity. Therefore, the MPPT is applied to boost the efficiency of the PV module. The maximum amount of power is delivered from the source to the load when their resistances are equal [9]. MPPT is based on the premise of automatically determining the maximum current I_{MP}, or voltage V_{MP}, at which photovoltaic modules must operate in order to generate the greatest power P_{MPP}, under certain irradiance and temperature circumstances. Under partial shade, it is possible to acquire many peaks, as shown in Figure (3.11); nevertheless, it is difficult to measure the absolute MPP. [12].

3.1.2.1 MPPT Techniques

Maximum power point tracking (MPPT) techniques are vital in photovoltaic applications because the MPP of a PV module changes with solar radiation and temperature. To extract the greatest amount of electricity from a PV module, MPPT algorithms are necessary. Using a number of techniques, the identification of the maximum power point has been strengthened and reported. These methods vary in a variety of aspects, including necessary sensors, complexity, cost, speed, tracking correction, and application simplicity. The most prominent MPPT approaches include [10]:

1. Perturb and observe (P&O).
2. Incremental conductance (INC).

3. Fractional open-circuit voltage.
4. Fractional short-circuit current.
5. Neural networks.
6. Fuzzy logic.

Table 3.1: Main Characteristics of Various MPPT Techniques [28]

Methods	Convergence Speed	Implementation Difficulty	Frequent Tuning	Sensed Parameters	Analog or Digital
P&O	Varies	Low	No	V, I	Both
Incremental Conductance (INC)	Varies	Medium	No	V, I	Digital
Fractional (V_{OC})	Medium	Low	Yes	V	Both
Fractional I_{SC}	Medium	Medium	Yes	I	Both
Neural Networks	Fast	High	Yes	Varies	Digital
Fuzzy Logic	Fast	High	Yes	Varies	Digital

3.1.2.1.1 Perturb and Observe (P&O)

Each MPPT method has benefits and downsides. The perturb and observe (P&O) method is one of the most popular and basic MPPT techniques. In this method, voltage and current sensors are used to measure the PV array's power output. This method is considered clear and easy to implement [10]. In the P&O method, the array voltage generates a continuous disruption. The subsequent step is to match the new PV output power to the prior cycle. When a little disturbance is introduced into the system, the photovoltaic array's output power is adjusted. Therefore, if the power fluctuation is positive, the direction of the disturbance stays unchanged. However, if the variation is negative, the incremental voltage will reverse direction. Consequently, the sign of the preceding increase in power and perturbation is utilized to identify the direction of the

upcoming perturbation. The following equation depicts the power change and outlines the P&O method's methodology:

$$\Delta P = PK - (PK - 1) \quad \ldots(10)$$

Where:

- PK = The new power point.
- PK-1 = The prior power point of power.

By comparing the new power point to the prior power point, the new MPP may be calculated. As shown in Figure (3.12), the power will grow as the voltage lowers to the right of the maximum power point. The power is increased by increasing the voltage on the left side of the MPP. The P&O approach is useful when temperature and solar radiation conditions vary gradually; nevertheless, it does not track the maximum power point [28]. Each tracking cycle causes the solar array's voltage to vary, a frequent problem with this technology. Therefore, progressive conduction is used to avoid this problem. The flowchart of the P&O algorithm is shown in Figure (3.13) [10].

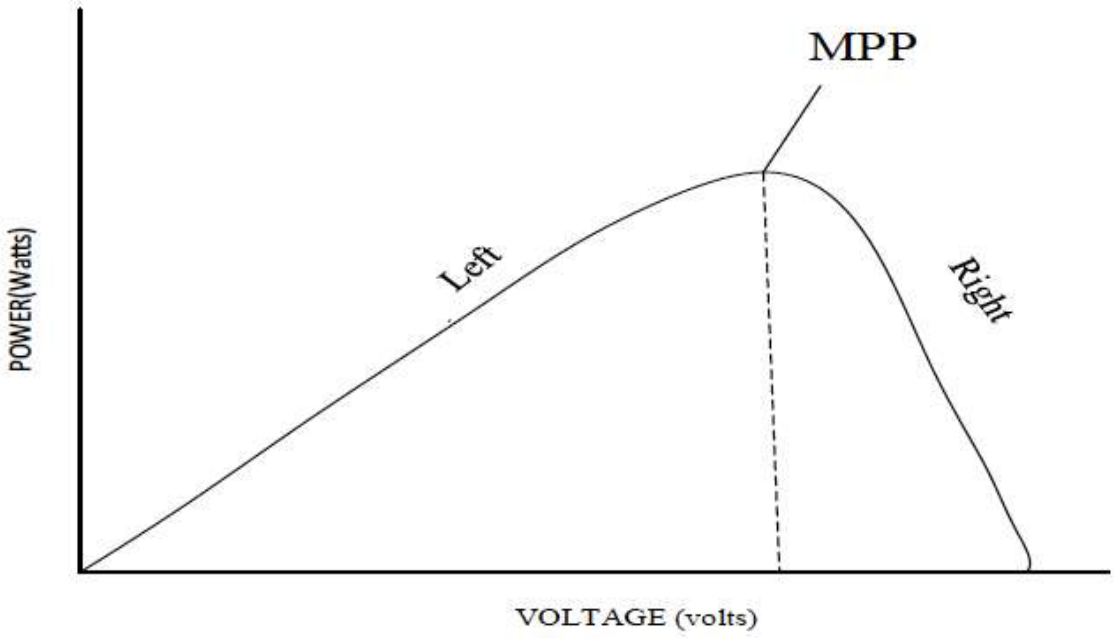

Figure 3.12: P-V characteristics (the principle of P&O technique).

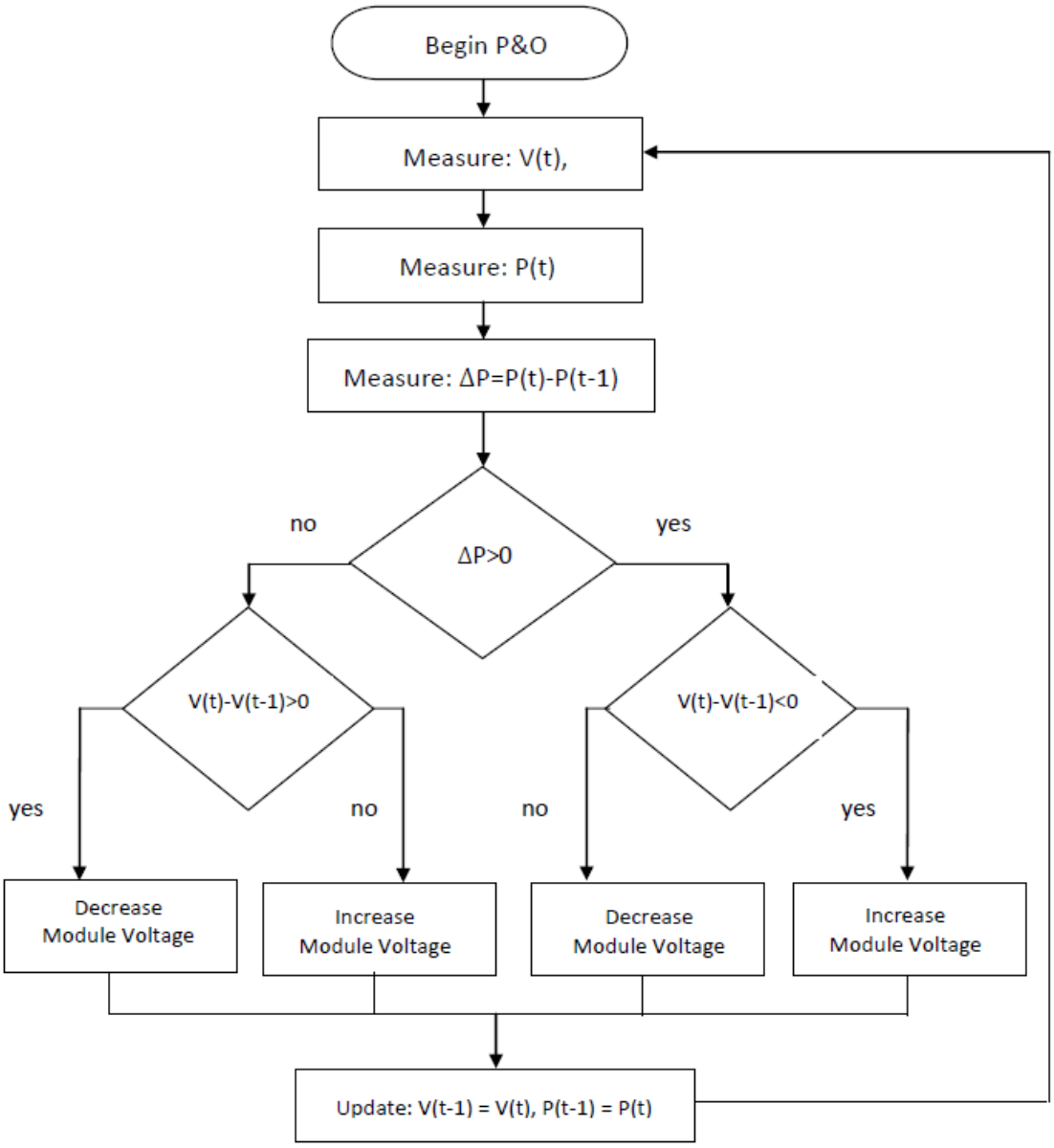

Figure 3.13: Flowchart of P&O algorithm.

P&O method will be used to track MPP in the PV system; therefore, this algorithm is constructed using MATLAB/Simulink, as shown in Figure (3.14). The MATLAB code to this algorithm is on Appendix-I.

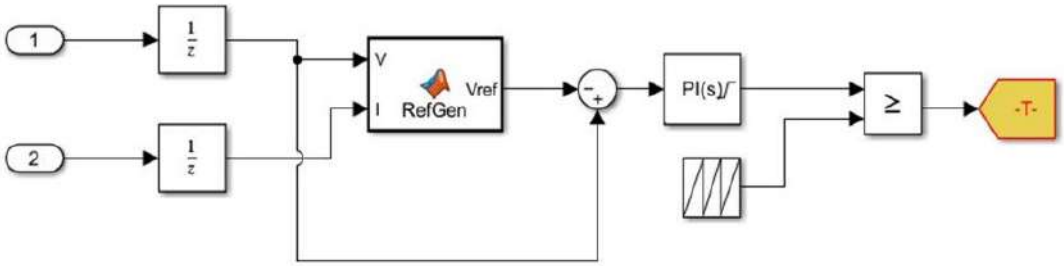

Figure 3.14: The Simulink model of P&O algorithm.

3.1.3 Finalized Model of the PV System

This power plant's PV Site comprises of a PV Module, a Converter coupled to the MPPT and the Battery Storage system, and an Inverter. As described in previous chapter, the production of solar energy relies on solar radiation and temperature. Figure (3.15) depicts the PV power generating site's Simulink model.

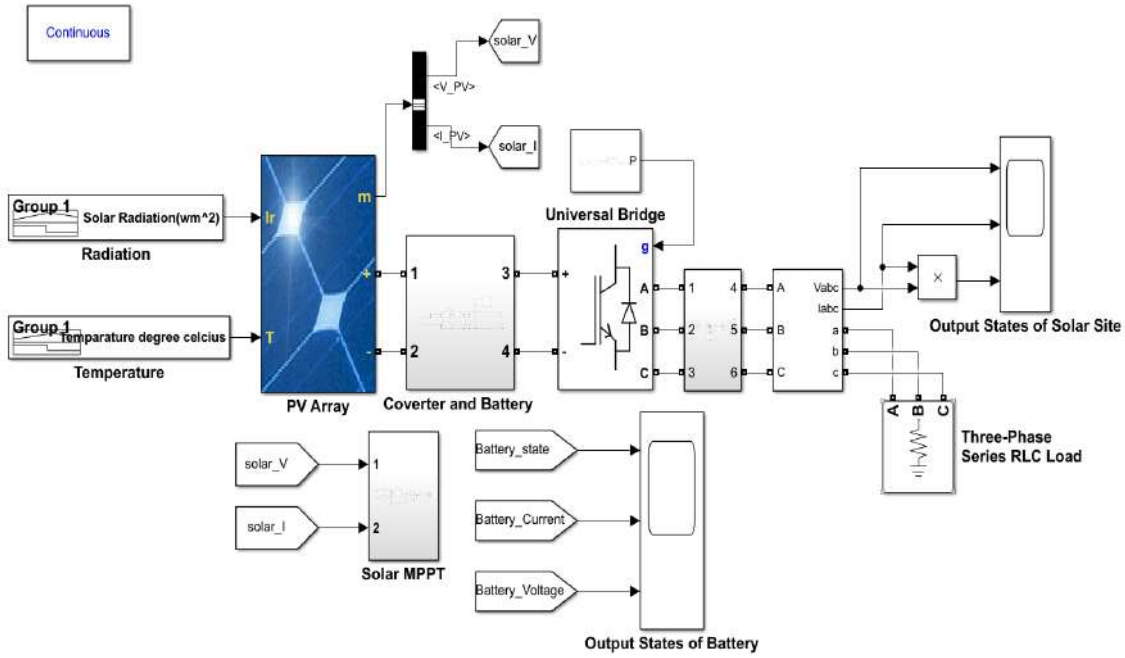

Figure 3.15: Simulink model of the PV System

3.2 BATTERY AND POWER MANAGEMENT SYSTEM

3.2.1 Introduction

The battery is a device for storing energy that may also serve as a power source. In this thesis, the battery storage system is linked to Perturb and Observe (P&O) and the PV power system. In a PV system, P&O is used to control the flow of power. The power flow of the battery storage system should be bidirectional. Therefore, a bidirectional converter is required to charge and discharge the battery in the event of an excess or deficiency of power [7].

3.2.2 Battery

A battery is a group of electrochemical cells capable of converting chemical energy to electricity. Nickel Cadmium (NiCd), Nickel Metal Hydride (NiMH), Lead Acid, Lithium Ion (Li-ion), and Lithium Polymer (Li-Poly) are examples of chemically unique battery types [40]. The battery is designed using MATLAB/Simulink, as shown in Figure (3.16).

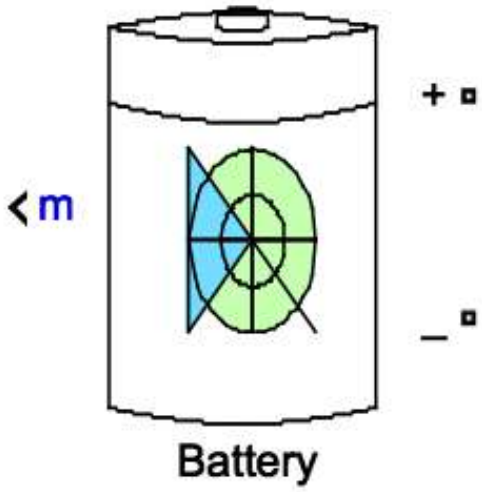

Figure 3.16: The Simulink model of the battery.

As depicted in Figure (3.17), the battery discharge characteristics for nominal discharge current (1A) vs different discharge currents (2, 4, and 6A).

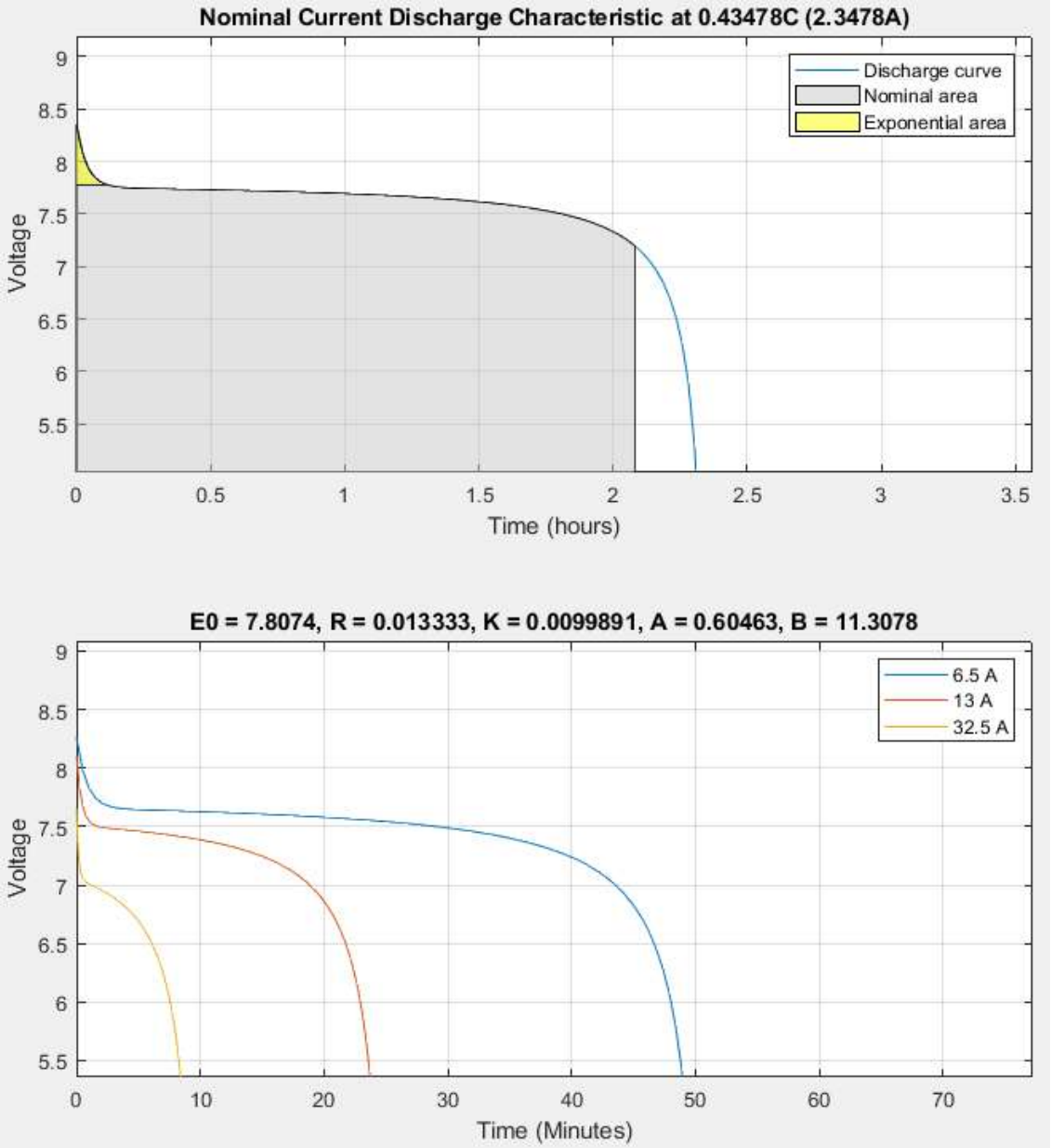

Figure 3.17: Battery discharge characteristics.

3.3 CONVERTERS

3.3.1 DC-DC Converters

A DC-DC converter is an electrical device that converts DC power to a high or low level. Similar to an AC transformer, it has the ability to raise or decrease the voltage level. The irregular DC voltage value may be stabilized by adjusting the duty cycle ratio of the converter. Three essential topologies are shown here (buck, boost, and buck-boost) [31].

3.3.1.1 Buck Converter

A buck converter's primary purpose is to lower voltage. Figure (3.18) is the simplest depiction of this converter. When the switch is in the conduction state, the input voltage and load voltage are same, and current flows from the input to the load. There will be no voltage across the load while the switch is open, and the current will stay constant. Since power is transferred from input to output, the DC voltage across the output is always less than that across the input [7]. The following formula may be used to get the average output voltage:

$$V_o = \left(\frac{1}{T_S}\right)\int_0^{T_S} V_o(t)dt = \left(\frac{1}{T_S}\right)((t_{ON}.V_d) + (t_{OFF}.0) = \left(\frac{t_{ON}}{T_S}\right).V_o \qquad \ldots(1)$$

Hence, the duty cycle would be:

$$D = \frac{t_{ON}}{T_S} \qquad \ldots(2)$$

And therefore,

$$V_o = D\,.V_d \qquad \ldots(3)$$

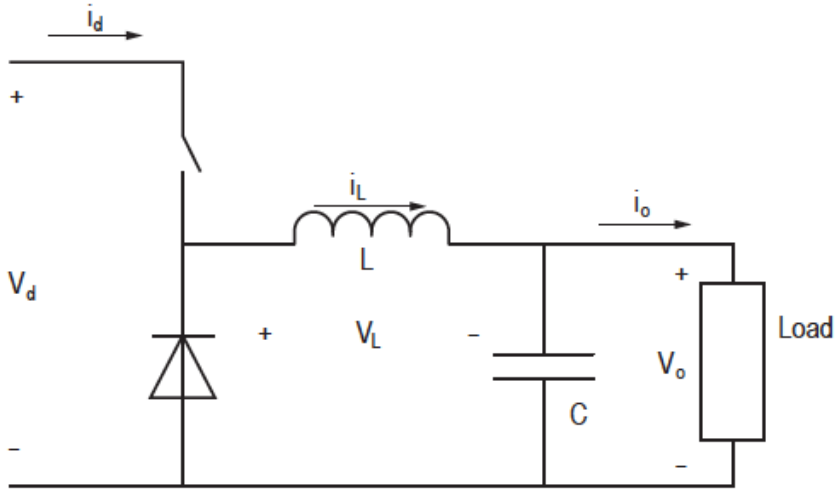

Figure 3.18: A Buck converter

3.3.1.2 Boost Converter

This converter's principal job is to boost the voltage. Figure (3.19) depicts the electrical circuit of the boost converter.

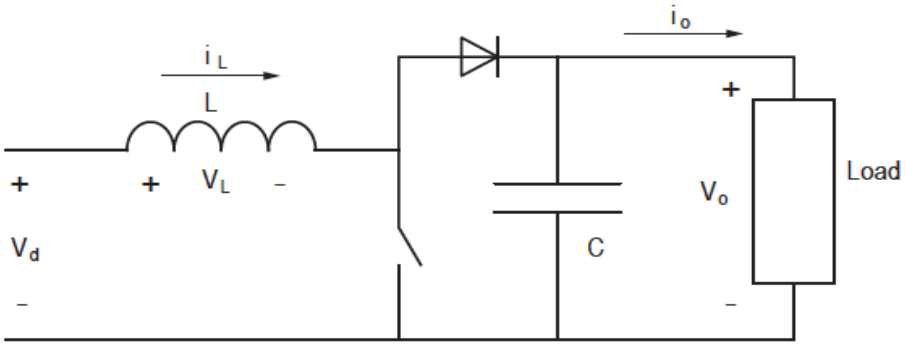

Figure 3.19: A boost converter.

3.3.1.2.1 First-Mode Operation

When the switch is closed, the inductor stores energy that is subsequently discharged against a voltage that is larger than the initial voltage (V_o). Thus, energy is transferred from a voltage with a lower potential to one with a greater potential. In this condition, the diode blocks current passage to the load. In addition, as seen in, the voltage across the output increases when the capacitor is depleted Figure 3.20).

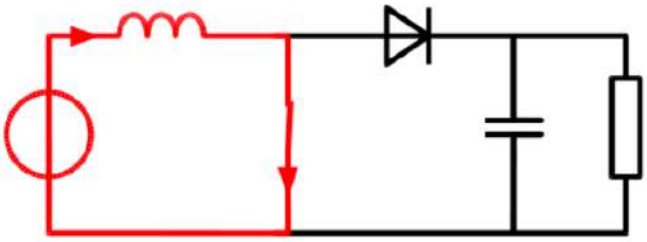

Figure 3.20: An on-state operation of a boost converter

3.3.1.2.2 Second-Mode Operation

When the switch is open, the diode is shorted, discharging the inductor and charging the capacitor with the energy that was previously stored. As seen in Figure (3.21), the load current stays constant during this cycle [32].

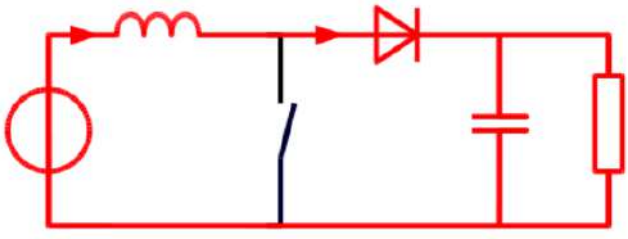

Figure 3.21: An off-state operation of a boost converter

Applying the inductor volt-second balance yields the following expression [33]:

$$t_{ON}.V_d + (V_d - V_0).t_{OFF} = 0 \quad \ldots(4)$$

This equation may be used to compute the input-to-output voltage ratio [33]:

$$\frac{V_0}{V_d} = \frac{1}{(1-D)} \quad \ldots(5)$$

In mode of continuous conduction, the equation (5) holds true. During the switching cycle, the output current will never be 0 in this mode.

The corresponding resistance encountered by the photovoltaic module, denoted by (R_{eq}), is:

$$R_{eq} = \frac{V_d}{I_d} = \frac{(1-D)V_0}{\frac{I_0}{1-D}} = \frac{(1-D)^2 V_0}{I_0} = (1-D)^2 R_L \quad \ldots(6)$$

3.3.1.3 Buck-Boost Converter

A buck-boost converter's function is to increase or decrease the DC voltage [34]. This converter incorporates both buck and boost converter topologies, making it the most significant form of switching regulator. Figure (3.22) depicts the electrical circuit of the buck-boost converter [12].

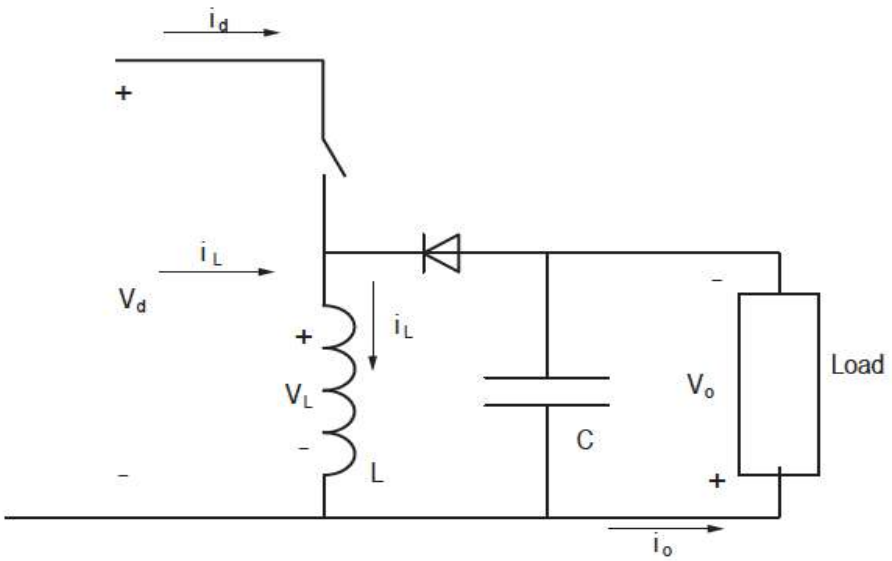

Figure 3.22: A buck-boost converter.

Modifying the output voltage (V_0) by adjusting the switching transistor's duty cycle ratio (D). The duty cycle ratio is the ratio of total switching time to operational time. This converter acts as both a buck and a boost converter, depending on the duty cycle [7]. When the duty cycle is less than 0.5, the converter operates as a buck converter and

reduces the voltage. However, when it is more than 0.5, the converter works as a boost converter and raises the voltage [33].

3.3.1.3.1 First-Mode Operation

When the switches are in the conduction mode, the input source is linked to the inductor, which is subsequently charged and used as an energy storage device. During this process, as seen in Figure (3.23), the capacitor supplies power to the load [33].

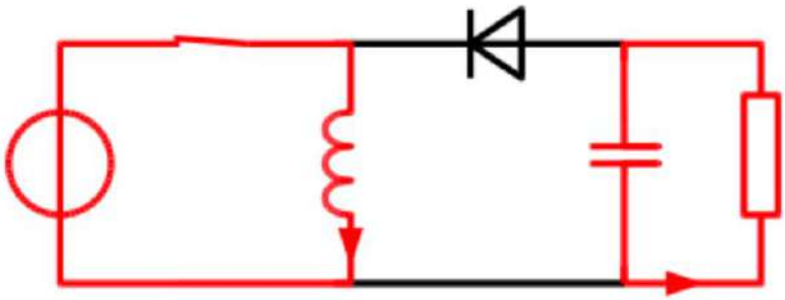

Figure 3.23: An on-state operation of a buck-boost converter.

3.3.1.3.2 Second-Mode Operation

During the open state of the switch, the inductor is linked to the capacitor and the load. As seen in Figure (3.24), the inductor transfers its stored energy to the capacitor and load [33].

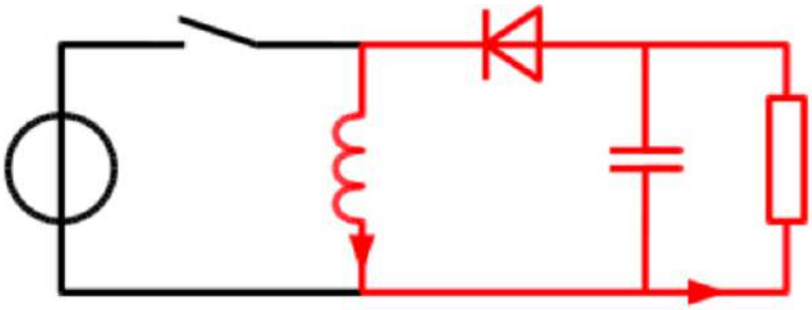

Figure 3.24: An off-state operation of a buck-boost converter.

3.3.1.4 Buck-Boost Converter with MPPT

By adding an intelligent device that changes the module's load resistance, the module's maximum power may be achieved. Power converters are applied to change and adapt the operational states in order to get the MPP. Figure (3.25) depicts the integration of a buck-boost converter into a solar system. Adjusting the duty ratio of the converter

allows control over the input voltage. By using inductor volt-second balancing in the manner of continuous conduction, we get:

$$t_{ON}.V_d + (-V_0).t_{OFF} = 0 \quad \ldots(7)$$

And, $$\frac{V_o}{V_d} = \frac{D}{1-D} \quad \ldots(8)$$

And, $$\frac{I_o}{I_d} = \frac{1-D}{D} \quad \ldots(9)$$

The load resistance will be expressed based on Ohm's law as:

$$R_L = \frac{V_o}{I_o} = (\frac{D}{1-D})^2.\frac{V_d}{I_d} \quad \ldots(10)$$

Consequently, the equivalent resistance observed at the solar module, expressed as (R_{eq}), is:

$$R_{eq} = \frac{V_d}{I_d} = (\frac{1-D}{D})^2 . R_L \quad \ldots(11)$$

This equation shows that the equivalent resistance (R_D) of the converter is dependent upon its duty cycle ratio. Consequently, the maximum power of the solar module may be obtained by adjusting the duty ratio (D). At the load terminal, electricity would be applied:

$$P_L = \frac{V_o^2}{R_L} = \frac{(\frac{D}{1-D}.V_d)^2}{R_L} = (\frac{1-D}{D})^2.\frac{V_d^2}{R_L} = \frac{V_d^2}{R_{eq}} \quad \ldots(12)$$

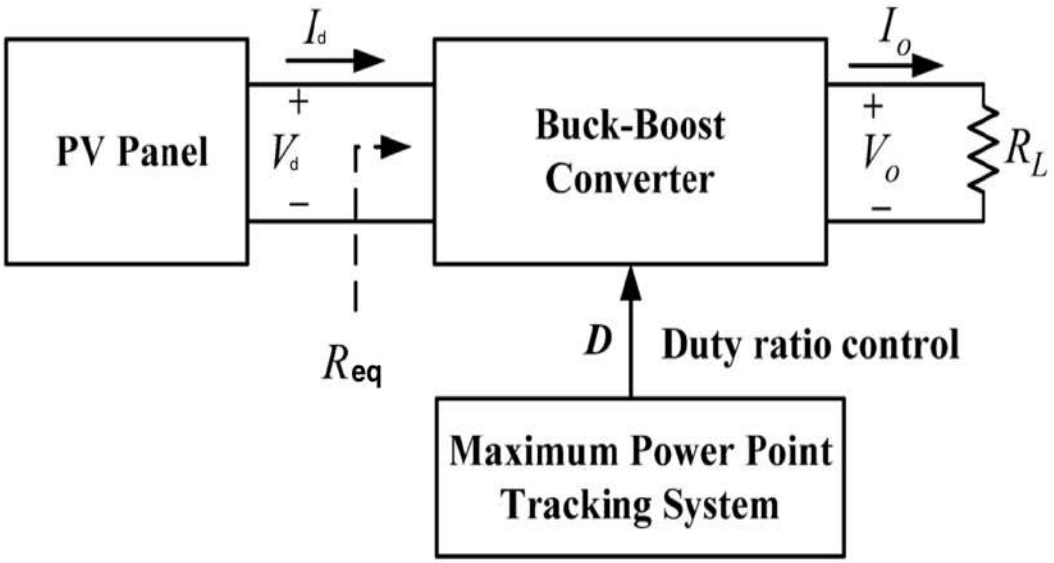

Figure 3.25: A PV array with a buck-boost converter.

3.3.2 Bidirectional DC-DC Converter

Bidirectional DC-DC converters allow electricity to flow in both directions, thus their name. These converters are applied in several applications, including uninterruptible power supply (UPS), battery storage systems, and renewable energy systems. Depending on the architecture of the system, the bidirectional DC-DC converter may either be buck or boost. Boost-type converters are attached to the low-voltage side, whereas buck-type converters are connected to the high-voltage side. In general, bidirectional DC-DC converters are classified as either isolated or non-isolated [7] according to the isolation between the input and output. The majority of bidirectional DC-DC converters use the circuit layout shown in Figure 3.26) [41].

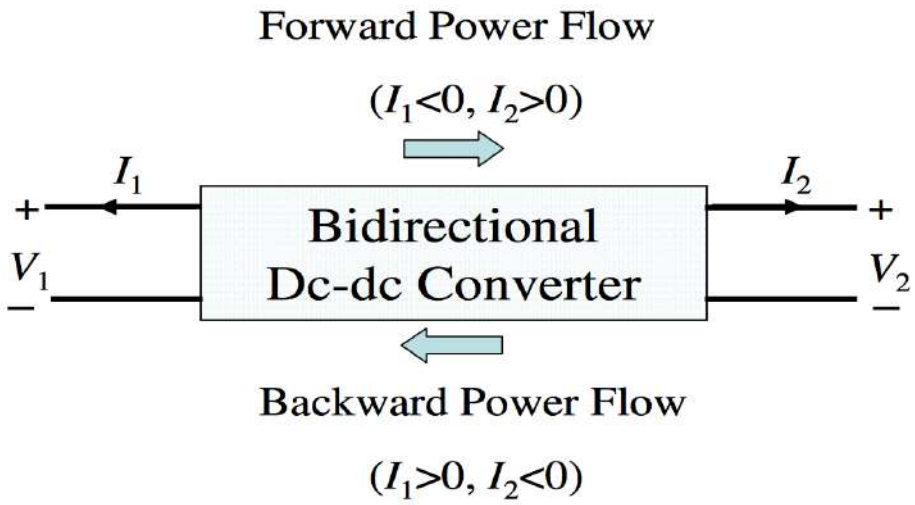

Figure 3.26: Bidirectional power flow.

3.3.2.1 Non-isolated Bidirectional DC-DC Converters

This kind of converter may be generated from converters that work in a single direction using bidirectional switches. Due to the unidirectional nature of its diodes, several kinds of converters, including buck and boost converters, do not support bidirectional power flow. This issue, however, may be remedied by deploying an antiparallel diode, such as an IGBT or MOSFET, to allow current to flow in both directions [41].

3.3.2.2 Isolated Bidirectional DC-DC Converters

A bidirectional isolated converter has extensive power ranges. In this sort of converter, isolation is often provided by a power transformer that only functions in AC systems. Adding AC connection enhances the system's complexity as a result. There are several

kinds of isolated bidirectional converters, such as fly-back, forward fly-back, half bridge, and full bridge converters [41].

3.3.3 Bidirectional DC-DC Converter for Charging and Discharging

In this hybrid system, the bidirectional DC-DC converter is used to charge and discharge the battery in response to power excess and deficiency. When there is a surplus of energy, that is, when the supply exceeds the demand, the battery is charged, enabling the converter to function in the forward direction. When supply is less than demand, i.e., when there is a power deficit, the battery is discharged and starts to provide the load with the power shortfall. In this case, the converter starts to operate in reverse. Both the battery and the P&O are coupled to the DC-DC converter.

3.4 WIND ENERGY SYSTEM

3.4.1 Wind System Components

This system comprises of a wind turbine that transforms the kinetic energy of the wind into rotational motion, a gearbox that adjusts the rotational motion to the proper generator speed, and a generator that converts the mechanical power into electrical power. Figure (3.27) is a block schematic of the wind energy system [7].

Figure 3.27: The proposed wind energy system.

3.4.2 Modelling of Wind Turbine System

The purpose of the turbine blades is to transmit the kinetic energy of the wind to the generator. The following equation expresses the wind power (P_{wind}) in a certain region [36]:

$$P_{\text{wind}} = \frac{1}{2}\rho A v_w^3 \quad \ldots(1)$$

Where:

- ρ is the density of the wind (kg/m^3).
- A is the turbine swept area (m^2).
- v_w is wind velocity in (m/s).

Furthermore, the turbine absorbs only a fraction of this energy, therefore not all wind energy may be used. Betz's law dictates that the theoretical maximum efficiency (C_p) of a wind turbine is 59.3 percent. Many smaller wind turbine generators (WTG) on the market (less than 4kW) have an efficiency rate of 20%; however, a proper WTG with blades that have superior aerodynamics may attain up to 40% efficiencies. Consequently, turbines have varying rates of efficiency. The output of the turbine may be expressed as (P_m) [2]:

$$P_m = P_{wind} C_p(\lambda) \quad \ldots(2)$$

$$P_m = \frac{1}{2} C_p(\lambda, \beta) \rho A v_w^3 \quad \ldots(3)$$

$$\lambda = \frac{\omega R}{v} \quad \ldots(4)$$

Where:

- P_m is the mechanical power of the wind turbine (W).
- C_p is the performance coefficient of the turbine.
- β is the blade pitch angle (deg).
- λ is the tip-speed ratio.
- ω is the turbine rotational speed (rad/sec).
- R is radius (m).

Normalizing equation (3) yields the following expression in the per unit (pu) system [2]:

$$P_{m_{pu}} = (K_p)(C_{p_{pu}})(v_{w_{pu}}^3) \quad \ldots(5)$$

Where:

- $P_{m_{pu}}$ is power in (pu) of nominal power for values of ρ and A.
- $C_{p_{pu}}$ is performance coefficient in (pu) of the maximum value of C_p.
- $V_{w_{pu}}$ is the wind speed in (pu) of the base wind speed, which is the average wind velocity in (m/s).
- K_p is the power gain for $C_{p_{pu}}$ and $V_{w_{pu}}$, which is less than or equal to one.

Additionally, the turbine's torque may be stated as:

$$T = \frac{1}{2} C_t(\lambda, \beta) \rho A \, R v_w^2 \quad \ldots(6)$$

Where, $C_t(\lambda, \beta)$ is the torque coefficient of the wind turbine and may be established as:

$$C_t(\lambda, \beta) = \frac{C_p(\lambda, \beta)}{\lambda} \quad \ldots(7)$$

Moreover, the turbine coefficient (C_p) is determined based on the tip-speed ratio (λ) and the blade pitch angle (β) using the following equation [11]:

$$C_p(\lambda, \beta) = C_1 \left(\left(C_2 \frac{1}{\lambda_1} \right) - (C_3 \beta - C_4) \right) \left(e^{-C_5 \frac{1}{\lambda_1}} \right) + C_6 \lambda \quad \ldots(8)$$

The coefficients are: C_1 = 0.5176, C_2= 116, C_3 = 0.4, C_4 = 5, C_5 = 21, and C_6 = 0.0068 [11]. Hence:

$$C_p(\lambda, \beta) = (0.5176) \left(\frac{116}{\lambda_1} - 0.4\beta - 5 \right) e^{\frac{-21}{\lambda_1}} + 0.0068\lambda \quad \ldots(9)$$

In addition, the parameter ($\frac{1}{\lambda_1}$) is defined as follows, where λ_1 is a constant [11]:

$$\frac{1}{\lambda_1} = \left(\frac{1}{\lambda+0.08\beta} - \frac{0.035}{1+\beta^3}\right) \qquad \ldots(10)$$

The C_p-λ curves, for various pitch angles, are shown in Figure (3.28). The highest value of C_p is obtained at β = 0 and the nominal value of the tip-speed ratio λ.

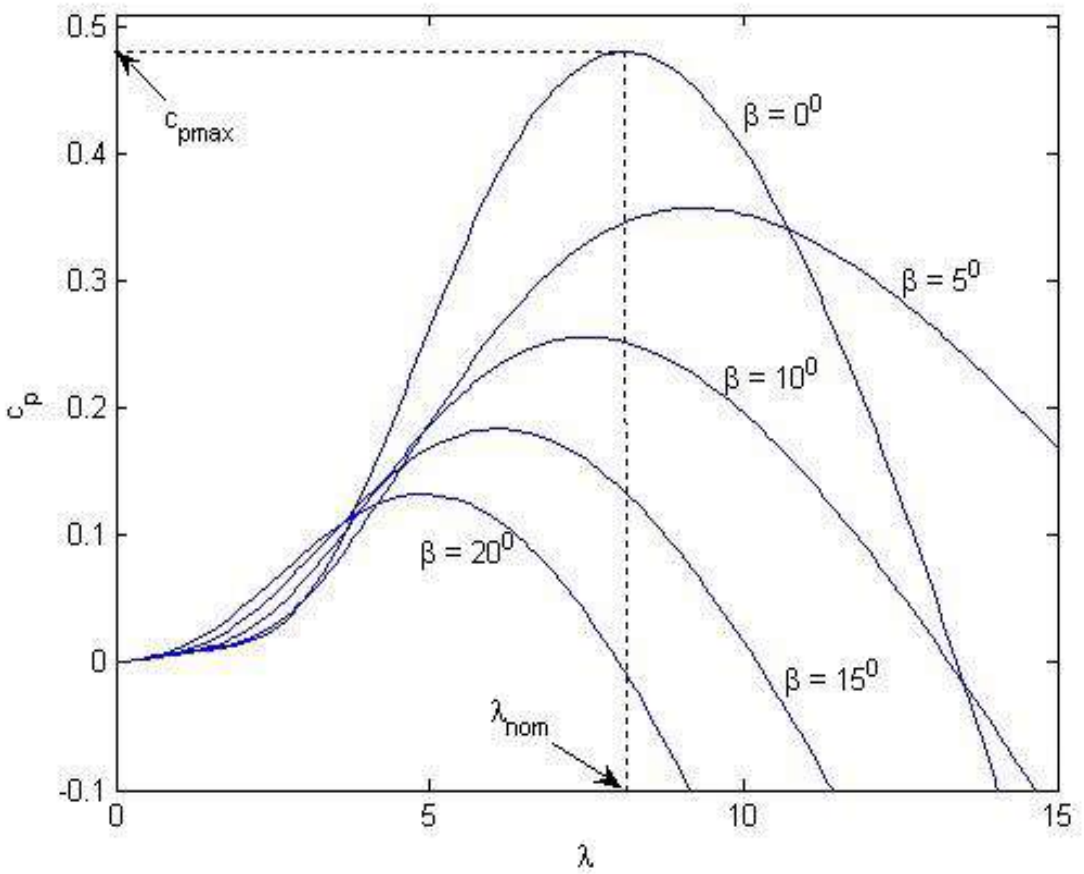

Figure 3.28: C_p-λ characteristics of wind turbines for various values of pitch angle β.

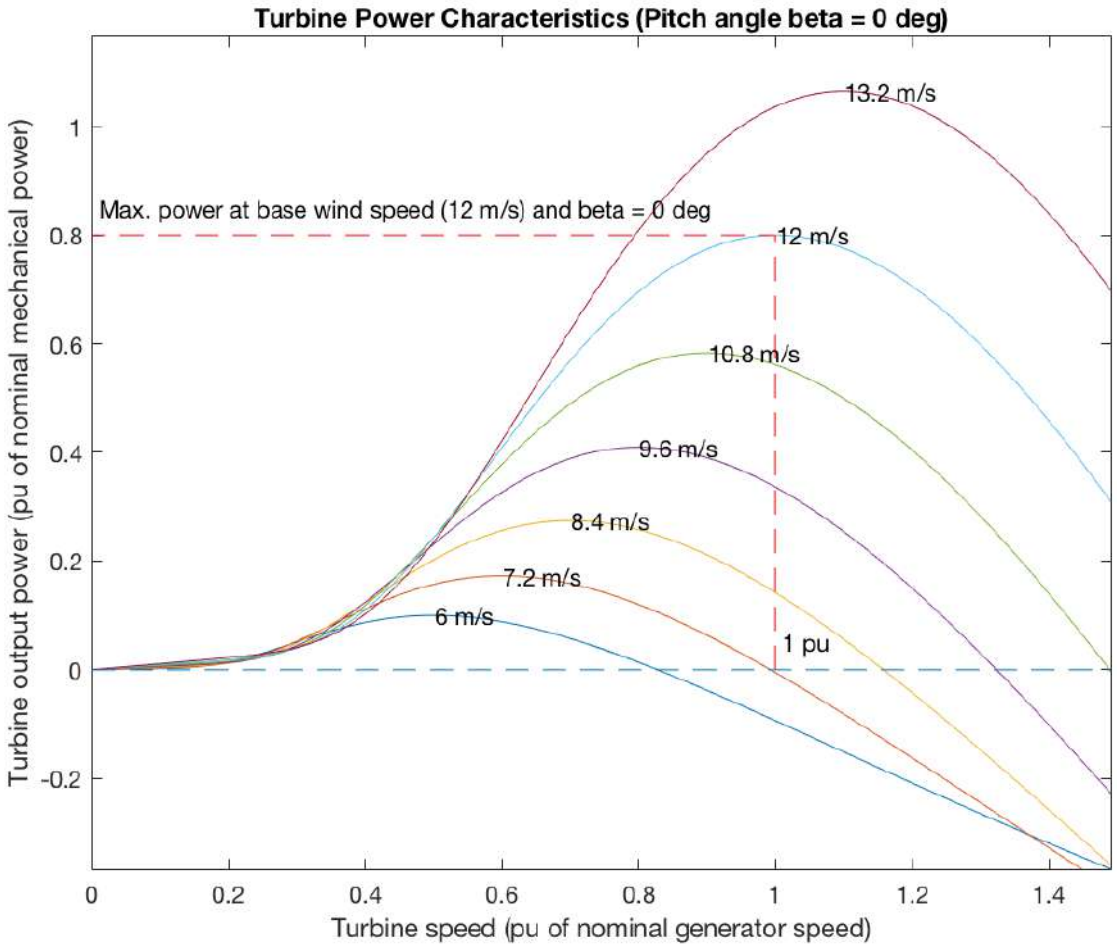

Figure 3.29: Wind-turbine power characteristics at β = 0.

3.4.3 Generators

On the basis of their Current type, generators may be categorized. There are AC and DC generators. In both cases, the produced voltage is alternating current. Alternating current may be converted to direct current via a commutator. AC generators may also be classified based on the speed of the rotor. There are two kinds of AC generators that are appropriate for wind power generation: synchronous generators with a constant speed and induction generators with variable speed. Despite the fact that both the doubly fed induction generator (DFIG) and the permanent magnet synchronous generator (PMSG) are appropriate for the wind energy system, the PMSG will be used to reduce the necessary supply [7].

3.4.3.1 Modelling of PMSG

The following equations may be used to represent the PMSG model in the synchronously rotating d-q reference system:

$$\frac{d}{dt}i_d = \frac{1}{L_d}v_d - \frac{R_s}{L_d}i_d + \frac{L_q}{L_d}pw_m i_q \quad \ldots(11)$$

$$\frac{d}{dt}i_q = \frac{1}{L_q}v_q - \frac{R_s}{L_q}i_q + \frac{L_d}{L_q}pw_m i_d - \frac{\lambda pw_m}{L_q} \quad \ldots(12)$$

$$T_e = \frac{3}{2}p[\lambda i_q + (L_d - L_q)i_d i_q] \quad \ldots(13)$$

Where,

- L_d, L_q are the generator inductance on the d-q axis;
- R_s is the stator resistance;
- i_d, i_q are, respectively, the dq-axis currents;
- v_q, $v_q$are the dq-axis voltages;
- w_m is the rotor angular speed;
- λ is the amplitude of the flux induced;
- p is the number of pole pairs;
- T_e is the electromagnetic torque [5].

3.4.4 Pitch Angle Controller

Controlling aerodynamic systems is crucial for regulating mechanical force. Pitch angle control is the most frequent way for managing the torque of a wind turbine. When wind velocity is below the nominal value, the optical angle approaches zero; nevertheless, as wind velocity rises, the optical angle increases. The pitch angle controller has a significant impact on the wind turbine's performance coefficient and torque value [37]. As seen in Figure (3.30), the rotor speed is added to the nominal speed to produce the output value of the pitch angle, which determines the performance coefficient of the wind turbine (C_p) [38].

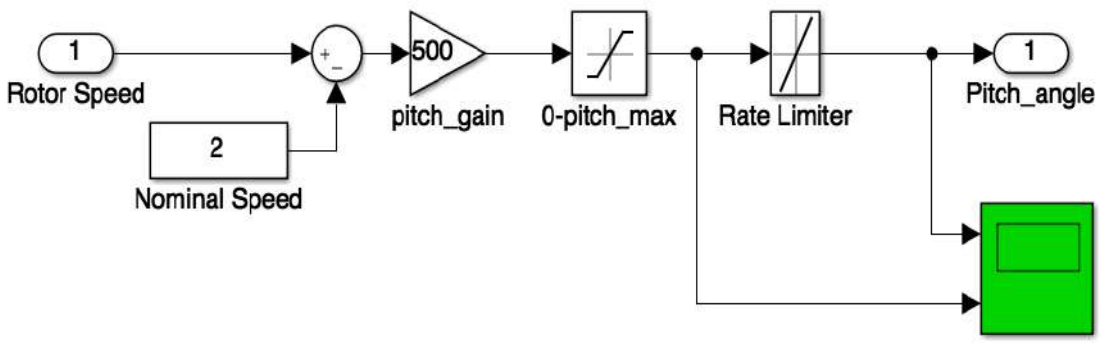

Figure 3.30: The pitch angle controller in Simulink.

3.4.5 Finalized Model of Wind System

At the Wind Turbine site, we used a Wind Turbine system based on PMSG. In addition, it has a Pitch Angle controller for adjusting the aerodynamic torque of the Turbine as necessary. Figure (3.31) depicts the Simulink model of the Power Plant's Wind Turbine site.

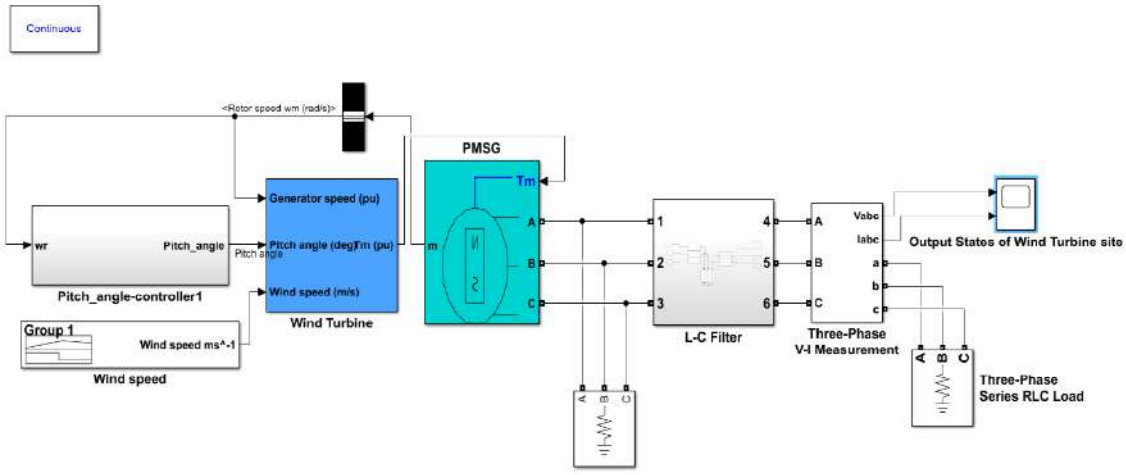

Figure 3.31: Simulink model of the Wind system.

3.5 BIOGAS FUELED POWER SYSTEM

3.5.1 Introduction

Future energy systems may rely heavily on bioenergy derived from biomass due to its renewability and sustainability. The extensive distribution of biomass offers plentiful supplies of raw materials, while the fast development of bioenergy conversion technology has boosted its competitiveness. Bioenergy, which is used to create Biomass, heat, and power, may be produced by thermochemical, biological, and bio-electrochemical processes, among others. Bioenergy systems should be enhanced to guarantee their long-term survival, boost their effectiveness, and minimize their costs.

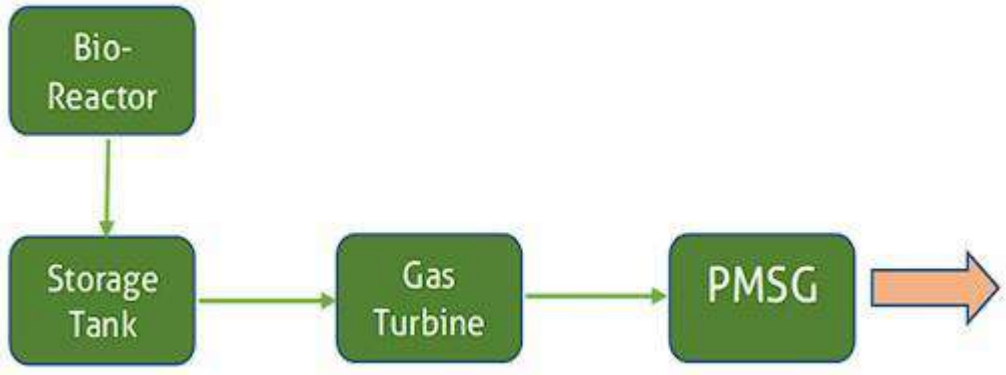

Figure 3.32: The proposed Biomass energy system

3.5.2 Mathematical Modelling

The suggested concept consists of three primary components: a biogas reactor, a Mini Turbine (MT) coupled to a permanent magnet synchronous generator, and a storage system. This section provides examples of mathematical modelling and simulation for different components.

3.5.2.1 Modelling of Biogas Reactor

A set of differential equations may be used to construct the mathematical model of the reactor, which describes the dynamic behavior of the four previously stated phases in an AD bioreactor with constant volume. The methane production of this model is dependent on the reactor's capacity, temperature, and the kind of animal feces.

3.5.2.1.1 Hydrolysis Modelling

The first phase of the AD procedure is hydrolysis. During the AD process, this is indicated as the rate of change in the concentration of biodegradable volatile solids (BVS) in the reactor. Process variables include the kind of input material, its flow rate, the effective volume of the reactor, and its temperature. The below equation represents the hydrolysis process [48]:

$$\frac{d(Sb)}{dt} = (Sb_{in} - Sb) \times \left(\frac{F_{feed}}{V}\right) + \frac{\mu_m K_1 . X_{acid}}{\frac{K_s}{Sb}+1} \quad \ldots(1)$$

Where,

- Sb is the biodegradable volatile solids concentration in the reactor (kg/m3),
- Sb_{in} is the biodegradable volatile solids concentration in the reactor feed (kg/m3),
- F_{feed} is the feed flow rate (m3/day),
- V is the effective reactor volume (m3),
- K_1 is the yield factor estimated,
- X_{acid} is the concentration of acidogens (kg/m3),
- K_s is the Monod half-velocity constant for acidogens (kg/m3),
- μ_m is the maximum growth rate for acidogens (d−1),
- X_{meth} is the concentration of methanogens (kg/m3).

Using the following empirical formula, the maximum growth rate of methanogens can be stated as a function of the temperature dependence of reaction rates.

$$\mu_m(T_{react}) = \mu_{mc}(T_{react}) = 0.013.T_{react} - 0.0129 \quad \ldots(2)$$

Where,

- μ_{mc} is the maximum growth rate for methanogens (d^{-1})
- T_{react} is the reactor temperature (°C).

The Simulink model represents the hydrolysis process is shown in Figure (3.33):

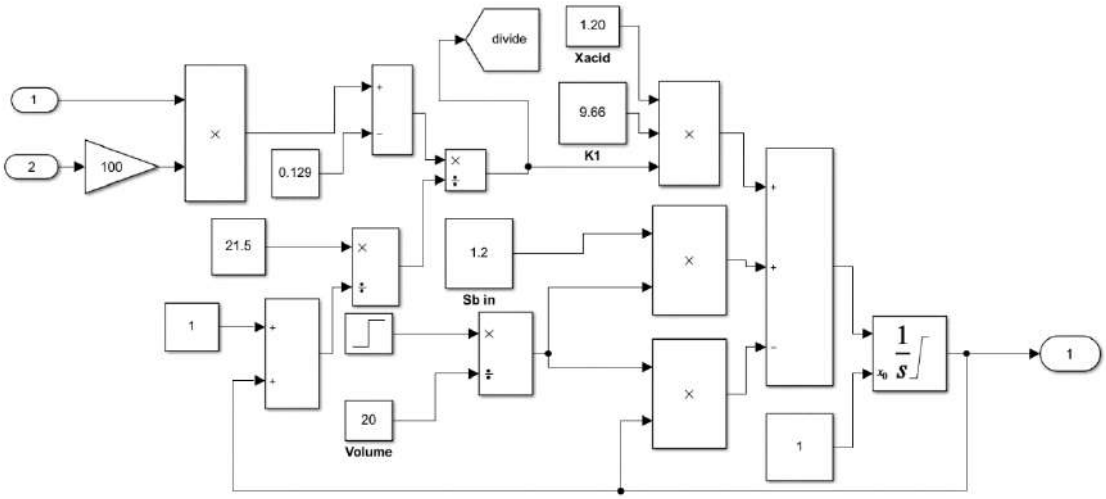

Figure 3.33: Simulink model for hydrolysis process.

3.5.2.1.2 Acidogenesis Modelling

Acidogenesis reflects the rate of change in volatile fatty acid content throughout the fermentation process. The process is dependent on the concentration of total volatile fatty acids in the reactor (type of feed material), the feed flow rate, the reactor's effective volume, and its temperature. The following equation depicts the acidogenesis process [48]:

$$\frac{d(S_v)}{dt} = (S_{vin} - S_v) \times \left(\frac{F_{feed}}{V}\right) + \frac{\mu_m K_2 . X_{acid}}{\frac{K_s}{S_b}+1} - \frac{\mu_m K_3 . X_{meth}}{\frac{K_{sc}}{S_v}+1} \quad \ldots(3)$$

Where,

- S_v is the concentration of total volatile fatty acids in the reactor (kg/m3),
- S_{vin} is the concentration of total volatile fatty acids in the reactor feed (kg/m3),
- K_2 is the yield factor estimated using experimental data,
- K_3 is the yield factor related to growth rate of methane gas,
- K_{sc} is the half-velocity constant for methanogens (kg/m3).

As illustrated in Figure (3.34), the Simulink model shows the acidogenesis process:

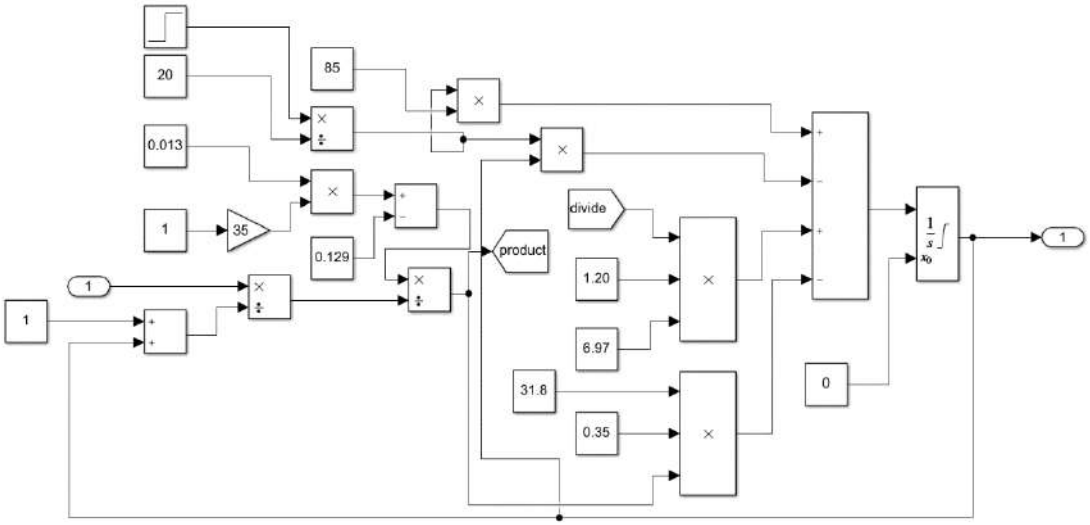

Figure 3.34: Simulink model for acidogenesis process

3.5.2.1.3 Acetogenesis Modelling

The acidogenesis procedure is the third step in the AD procedure. This procedure relies on acidogenic concentration, feed material type, feed flow rate, effective reactor capacity, and reactor temperature. The following equation represents the process of acetogenesis [48]:

$$\frac{d(X_{acid})}{dt} = \left[\frac{\mu_m}{\frac{K_s}{S_b}+1} - K_d - \left(\frac{\frac{F_{feed}}{b}}{V}\right)\right]. X_{acid} \quad \ldots(4)$$

Where,

- b is the retention time factor estimated using experimental data
- K_d is the specific death rate of acidogens (d^{-1}).

The Simulink model in Figure (3.35) represents this process:

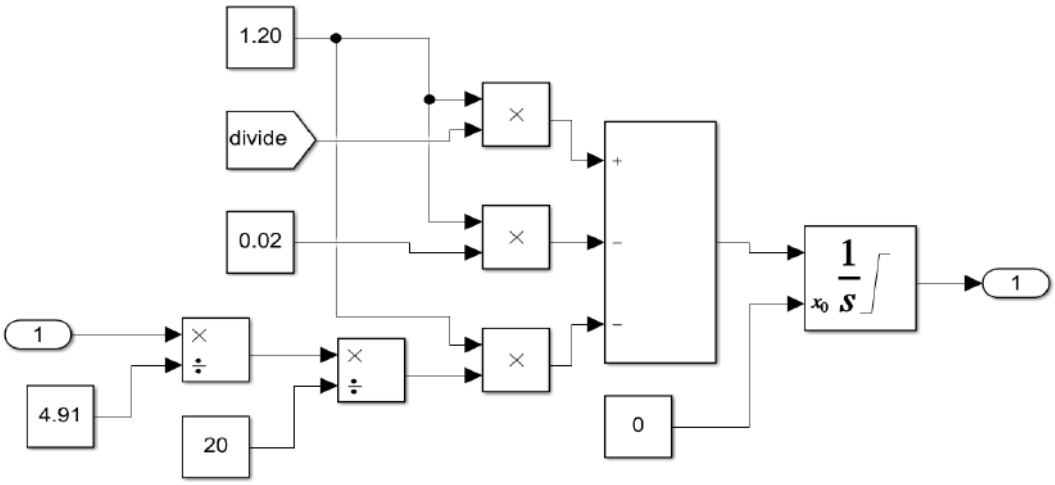

Figure 3.35: Simulink model represents acidogenesis process.

3.5.2.1.4 Methanogenesis Modelling

The stage of methanogenesis dictates the concentration of methanogens used to create methane. Process variables include retention time, feed flow rate, effective reactor volume, and reactor temperature. The following equation represents the process of Methanogenesis [48]:

$$\frac{d(X_{meth})}{dt} = \left[\frac{\mu_{mc}}{\frac{K_{sc}}{S_v}+1} - K_{dc} - \left(\frac{\frac{F_{feed}}{b}}{\mathrm{V}}\right)\right].\, X_{meth} \quad \ldots(5)$$

Where,

- K_{dc} is the specific death rate of a methanogens (d^1) and
- X_{meth} is the concentration of methanogens (kg/ m3).

Figure (3.36) illustrates the Simulink model of methanogenesis process.

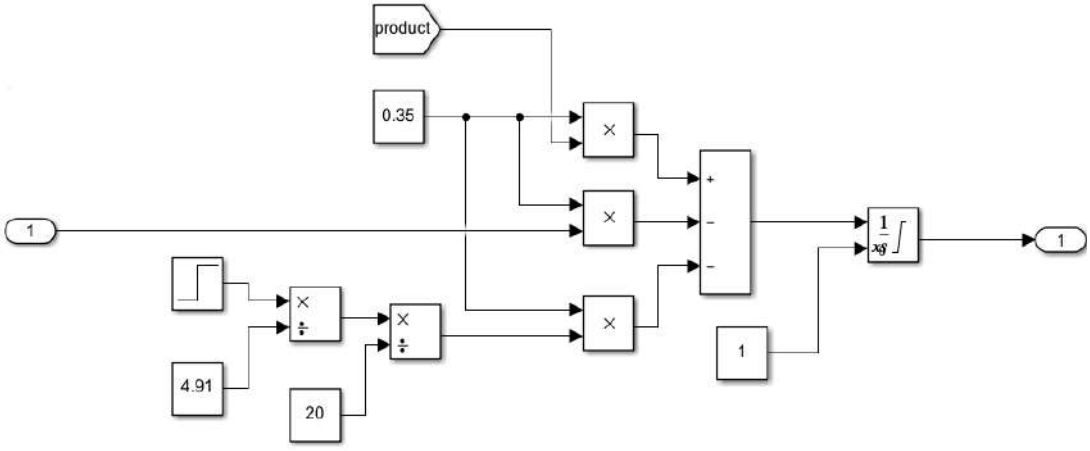

Figure 3.36: Simulink model of methanogenesis process.

The quantity of methane produced by the reactor is calculated as follows [46]:

$$F_{meth} = V.\frac{\mu_{mc}}{\frac{K_{sc}}{S_v}+1}.K_4.X_{meth} \quad \ldots(6)$$

Where, K_4 is a factor linked to methane gas flow that is determined based on experimental data. Figure (3.37) depicts a Simulink model of the given equation:

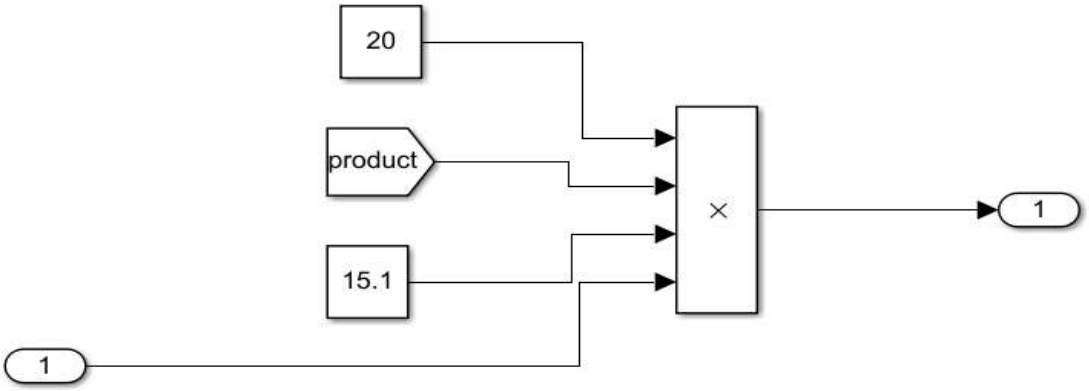

Figure 3.37: Simulink model representing amount of methane output from reactor.

3.5.2.1.5 Reactor Simulink Model

Figure (3.38) shows the complete Simulink model for the previous four stages of AD process represented by Equations.

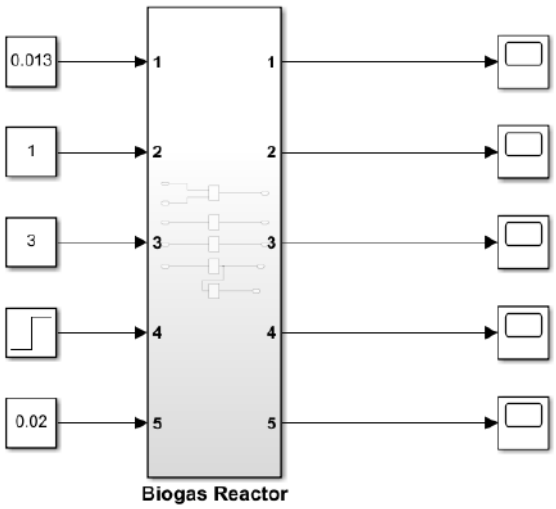

Figure 3.38: Simulink model for the four stages of AD process.

3.5.2.2 Modelling and Control of a Microturbine-Generation System

MTs are miniature gas turbines that use liquid or gaseous fuels to produce a high-energy gas stream that drives an electrical generator. In the next subsections, MT components

and their functioning principles are described in detail. Following the derivation of a suggested Simulink model for an MT-generation system, a proposed Simulink model for an MT-driven PMSG is presented.

3.5.2.2.1 Principles of Microturbine Working

MT produces power utilizing a high-speed generator directly driven by the turbo-compressor shaft. As is the case with the single-shaft designs under discussion, the removal of the gearbox that reduces the shaft speed to that of conventional electrical machines is of tremendous benefit to small gas turbines. The outcome is a machine that is more efficient, compact, and dependable, with a shaft speed that is normally more than 30 thousand rpm and may exceed 100 thousand rpm [49]. Permanent magnets and materials with a high yield strength, such as neodymium-iron-boron or Samarium-cobalt, have shown their suitability for high-speed electrical equipment.

In a PMSG, permanent magnets replace the rotor's dc field winding. Reduced field copper loss, greater power density, less rotor inertia, and a more robust rotor construction are among the benefits of PMSG. The lack of field flux control flexibility and the likelihood of demagnetization are negatives. The machine is more effective than an induction machine, although being often more costly. An MT generating system consists of a compressor, turbine, recuperator, and permanent magnet synchronous generator with a power electronics interface. The Brayton cycle underpins the functioning of MT. The parameters of the driving load significantly impact the decision between a single- or double-shaft MT. A single-shaft unit is typically specified when the load speed is constant, as in the case of an electric generator; a generator-specific engine would have a single-shaft structure. Alternatively, a two-shaft engine might be used. Two-shaft engines are beneficial when variable-speed propulsion is required. The incoming air is compressed using a radial compressor. This air is mixed with fuel in the combustor and burnt. The hot, combusting gas is amplified in the turbine to provide the mechanical energy that turns the compressor and generator. A recuperator, or air-to-gas heat exchanger, is added to increase the overall efficiency. Without a recuperator, an MT's overall efficiency is 15 to 17 percent, but it may be increased to 33 to 37 percent with an 85 percent-effective recuperator [50]. Figure (3.39) is a schematic illustration of an MT system [49].

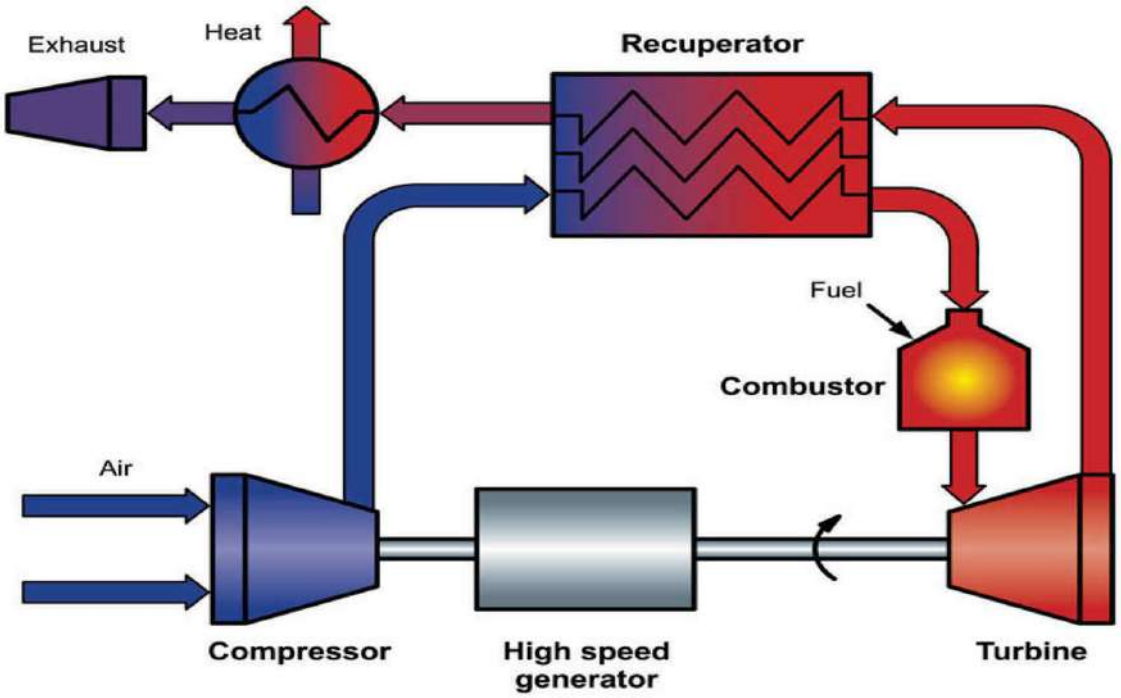

Figure 3.39: A schematic diagram of an MT system

3.5.2.2.2 Modelling of a Microturbine

The proposed model characterizes the dynamics of an MT and is suitable for simulation and analysis in steady-state and transient modes. The model incorporates a governor speed control, temperature control, acceleration control, fuel system control, and compressor-turbine model.

3.5.2.2.2.1 Speed Control

Under partial load settings, speed regulation is the primary form of control for the MT. It operates based on the difference in speed between a reference speed (one pu) and the synchronous generator rotor speed. Typically, speed control is represented by a lead-lag transfer function or a PID controller; however, a lead-lag transfer function is used to describe speed control in this work. The output of a droop governor is directly proportional to the speed deviation. The rate of change of an isochronous speed controller's output is proportional to its speed error. Any increase in load produces a decrease in speed. This control function is shown in Figure (3.40) as a block diagram [51]. K is the controller gain T_1 and T_2 are the governor lead and lag time constants, and Z is the governor mode in this schematic.

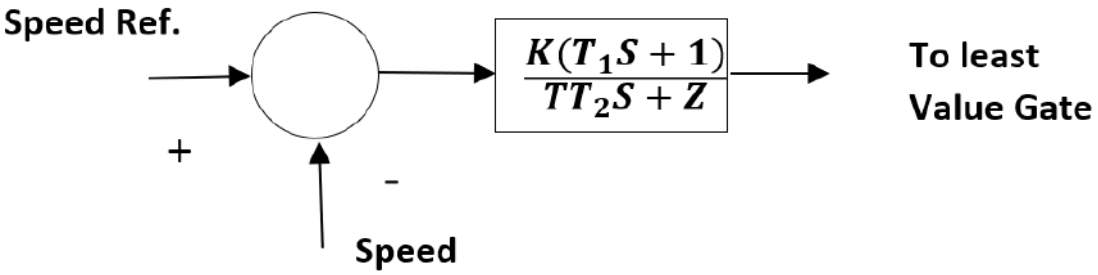

Figure 3.40: Block diagram represents MT speed control

3.5.2.2.2.2 Temperature Control

A temperature controller is used to restrict gas turbine output power to a preset firing temperature, irrespective of fluctuations in ambient temperature or fuel characteristics. Hot exhaust gases result from the combustion of fuel in the combustor. The temperature of these exhaust gases is detected using thermocouples inserted inside radiation shields. Typically, the thermocouple output is compared to a reference temperature that is greater than the thermocouple output. This keeps the temperature controller's output at its maximum, enabling the Least Value Gate to regulate the speed controller (LVG). When the thermocouple output exceeds the reference temperature, the difference becomes negative and the temperature control output decreases. Whenever the signal's declination surpasses the speed controller's output, the LVG will decrease the signal's value in order to restrict the turbine's output. Exhaust temperature is the input to the temperature controller, and the output is the temperature control signal to the LVG. Figure (3.41) depicts a block diagram of the temperature controller, where T_t is the temperature controller integration, T_3, T_4 are related with radiation shield and thermocouple time constants, respectively, K_1, K_2 are constants related with radiation shield, and T_5 is a time constant associated with the temperature controller.

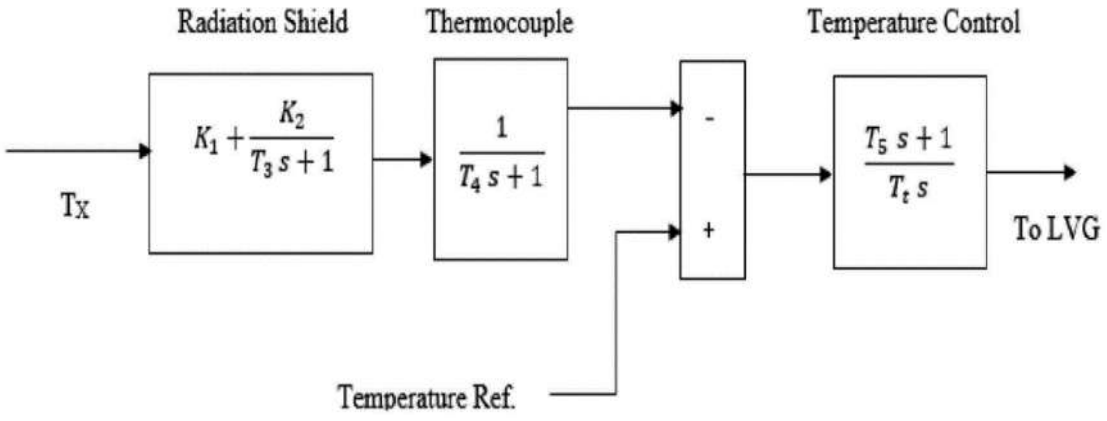

Figure 3.41: Block diagram of temperature controller

3.5.2.2.2.3 Acceleration Control

Typically, this kind of control is used during turbine startup to adjust the rotor's acceleration rate prior to achieving operational speed. These control routines generate LVG input signals. This LVG gate's output is the lowest of the three inputs, resulting in the least amount of fuel being transported to the compressor-turbine (see Figure 3.42).

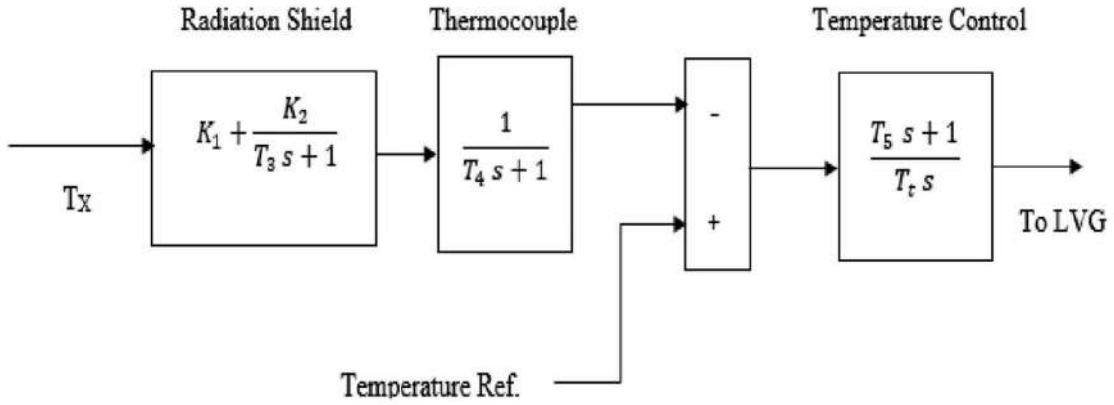

Figure 3.42: Block diagram of an MT control function

3.5.2.2.2.4 Fuel System Control

The fuel system is comprised of a fuel valve and an actuator. Fuel flows via the valve positioner from the fuel system actuator. The following describes the transfer function of the valve positioner [49]:

$$E_1 = \frac{K_v}{T_v S + C} F_d \quad \ldots(7)$$

However, the fuel system actuator transfer function is as follows:

$$W_f = \frac{K_f}{T_f S + C} E_1 \quad \ldots(8)$$

Where,

- K_v, K_f respectively valve positioner and fuel system actuator gain,
- T_v, T_f are time constants for the valve positioner and fuel system actuator, respectively,
- F_d, E_1 are inputs and outputs, respectively, of the valve positioner,
- C is a transfer function constant,
- W_f is the fuel demand signal in per unit.

The output of LVG is the least amount of fuel necessary for a certain operating point, V_{ce}. This output serves as an input to the fuel system. p.u turbine speed N is an extra fuel system input. The p.u value of V_{ce}. is proportional to the p.u value of the turbine's steady-

state mechanical power. Figure (3.43), where K3 indicates the lowest fuel flow at no-load, illustrates the fuel flow regulation as a function of V_{ce}.

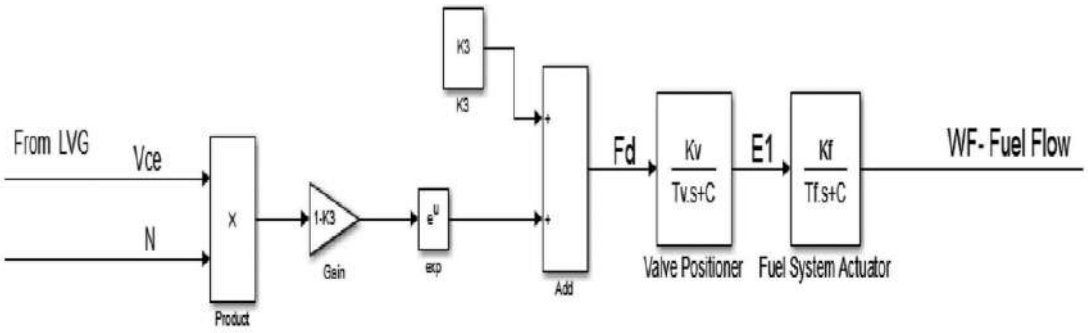

Figure 3.43: Block diagram of fuel system control.

3.5.2.2.2.5 Compressor-Turbine Model

The aim of the compressor in an MT is to deliver combustion burners with the necessary amount of air. Before discharging air to the burners at the correct magnitude and pressure, the compressor increases the pressure of the air from the air input duct. There is a small transport delay TCR associated with the combustion response time, a time lag TCD associated with the compressor discharge volume, and a transport delay TTD associated with the passage of gas from the combustion system to the turbine. Figure (3.44) depicts a block diagram of the model compressor-turbine. Below are the equations that explain the compressor-turbine model [42]:

$$P_c = \frac{W_a h_{IC}}{\eta_c \eta_{trans}} \quad \ldots(9)$$

$$W_g C_{pg}(T_{Tin} - 298) + W_f h + W_a C_{pa}(298 - T_{cout}) + W_{is} C_{ps}(298 - T_{is}) = 0 \quad \ldots(10)$$

$$P_T = \eta_T W_g h_{IT} \quad \ldots(11)$$

$$P_{mec} = P_T - P_c \quad \ldots(12)$$

Where,

- P_c is Power usage of the compressor
- W_a is Flow of air mass into the compressor
- Δh_{IC} Change in isentropic enthalpy upon compression from Pcin to Pcout
- η_c Overall compressor efficiency
- η_{trans} Efficacy of transmission from turbine to compressor
- C_{pg} Specific heat of combustion gases

- C_{pa} Specific heat of air at constant pressure
- C_{ps} Specific steam heat
- W_g Flow of turbine gas mass
- T_{Tin} Temperature of gas entering the turbine
- W_f Fuel mass flow
- T_{is} Temperature of injected steam
- W is Injection steam mass flow
- Δh Enthalpy specific to a reaction at the reference temperature
- Δh_{IT} Change in isentropic enthalpy for a gas expansion from P_{Tin} to P_{Tout}
- η_T Overall turbine efficiency
- P_{mec} Mechanical energy supplied via turbine
- P_T total mechanical power provided by the turbine

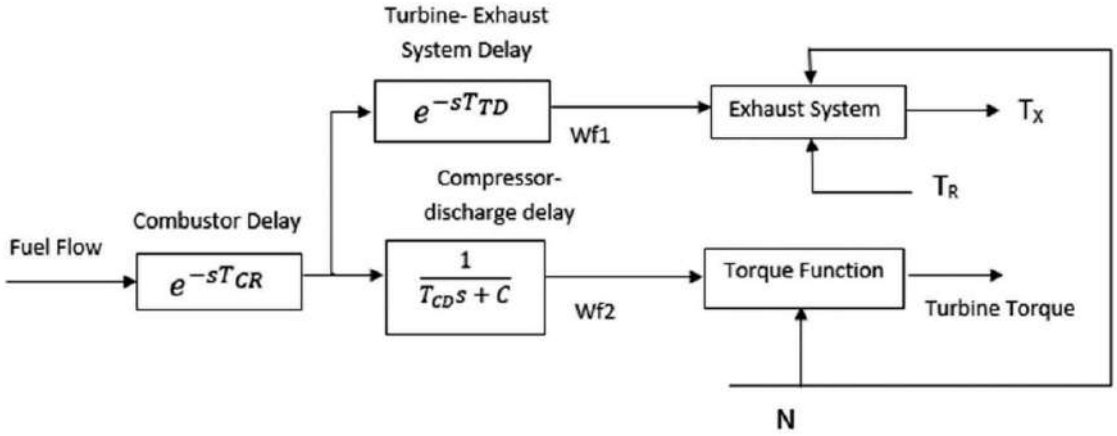

Figure 3.44: Block diagram of compressor-turbine model

3.5.2.2.2.6 Turbine Dynamics

Regarding fuel flow and turbine speed, a single-shaft gas turbine's torque and exhaust temperature characteristics are approximately linear. The mechanical torque that powers the electric generator is shown in the table below [49]:

$$T = KH(W_f - 0.23) + o.5(1 - N) \quad \ldots(13)$$

For MT temperature control operations, the turbine's temperature is calculated as follows [49]:

$$T_x = T_R - 700(1 - W_f) + 500(1 - N) \quad \ldots(14)$$

Where,

- KH is a coefficient dependent on the enthalpy of the combustion chamber's gas stream,
- T_R is the reference temperature,
- N is the p.u turbine speed and
- W_f is the p.u fuel demand signal.

This subsystem receives the p.u. fuel demand signal W_f, as input and outputs the p.u. turbine torque. MT is represented by an exhaustive Simulink model Figure (3.45) including all of its control systems.

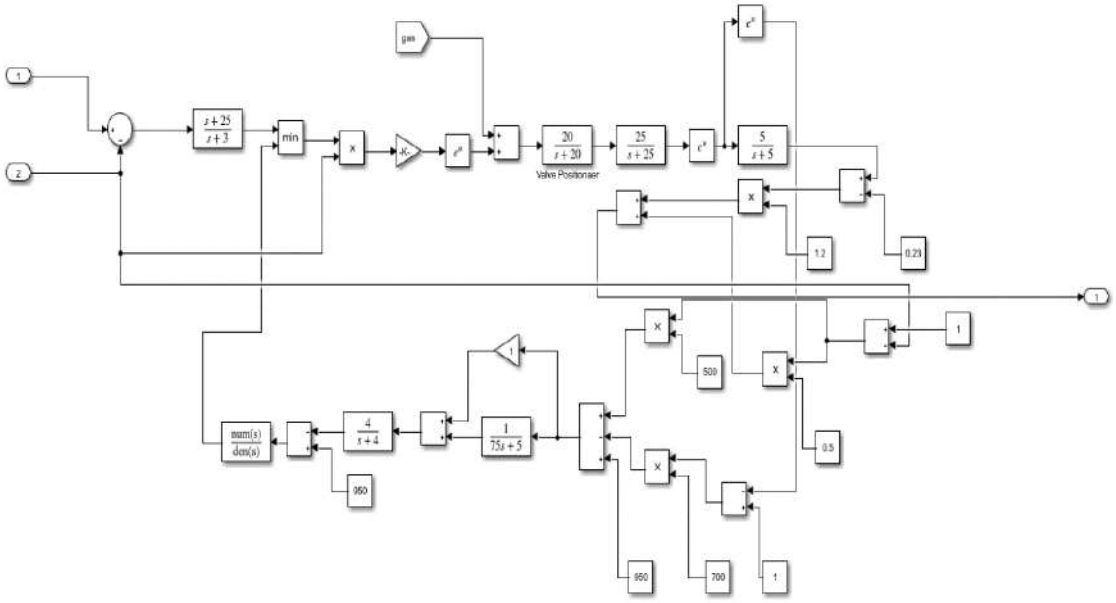

Figure 3.45: Model of MT in Simulink, containing all control systems

3.5.2.2.3 Permanent Magnet Synchronous Generator Model

In this study, a high-speed, 4-pole PMSG with a non-salient rotor model is coupled to a biogas MT to generate alternating current power. The electrical and mechanical components of the generator are both represented by a second-order state space model. It is assumed in this study that the flux created in the stator is sinusoidal, meaning that electromotive forces are similarly sinusoidal. Permanent magnets are attached to the rotor of a surface sinusoidal magnet machine, whereas they are mounted within the rotor of an interior magnet synchronous machine. The synchronously rotating air gap flux is produced by the stator's sinusoidal three-phase winding. The stator windings generate three-phase sinusoidal voltages that are balanced when the machine is rotated by a

primary mover. The PMSG configuration in dq0 reference frame (where 0-axis values are equal to zero for a balanced system) may be expressed as follows [42]:

$$\frac{d}{dt}i_d = \frac{1}{L_d}V_d - \frac{R}{L_d}i_d + \frac{L_q}{L_d}PW_r i_q \quad \ldots(15)$$

$$\frac{d}{dt}i_q = \frac{1}{L_q}V_q - \frac{R}{L_q}i_q + \frac{L_d}{L_q}PW_r i_d - \frac{PW_r}{L_q} \quad \ldots(16)$$

Ignoring core loss, the voltage equations for the d–q axis may be stated as follows [42]:

$$V_d = Ri_d + L\frac{d}{dt}i_d - W_r L i_q \quad \ldots(17)$$

$$V_q = Ri_q + L\frac{d}{dt}i_q - W_r L i_d + W_r \quad \ldots(18)$$

The following equation describes the electromagnetic field generated in the machine's air gap:

$$T_e = 1.5P(i_q{+}(L_d - L_q)i_d i_q) \quad \ldots(19)$$

The rotor speed is derived as follows from the dynamics of the mechanical system:

$$\frac{d}{dt}W_r = \frac{1}{j}(T_e - FW_r - T_M) \quad \ldots(20)$$

Where,

- V_q, V_d are q- and d-axis voltages,
- Ψd, Ψq are flux for d- and q-axis,
- L_{qm} is the mutual inductance of the stator's common q-axis,
- If comparable magnetic field current of permanent magnets,
- F is the viscosity of rotor and load friction,
- i_d, i_q are q- and d-axis currents,
- J is the combined rotor and load inertia,
- L_d, L_q are d- and q-axis inductances,
- P is the quantity of poles,
- R is the resistance of the stator windings,
- T_e is the electromagnetic torque,
- T_M is the mechanical torque,
- θ is the rotor's angular position,
- λ is the induced flux in the stator windings,
- W_r is the angular velocity of the rotor

3.5.2.3 Modelling of Storage System

The amount of biogas (methane) necessary to fulfill the load varies with the load value. To retain any extra methane gas concentrations, a storage device is necessary. The storage system in the proposed design comprises of two components: a comparator and a storage tank. The comparator compares the quantity of methane generated by the reactor to the amount necessary to provide the load. Figure (3.46) demonstrates the Comparator's Simulink model.

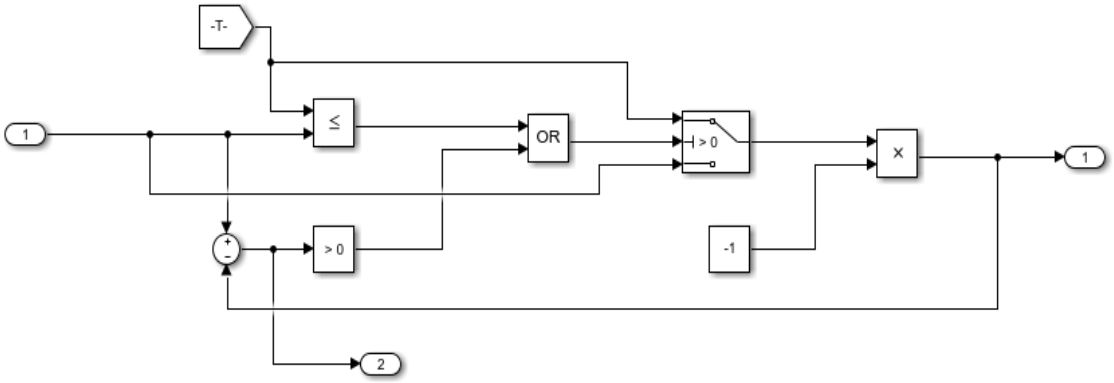

Figure 3.46: Simulink model for the storage system

The biogas production per day can be calculated as follows:

$$V_{day} = n * V_b * C_e \qquad \ldots(21)$$

Where,

- V_{day} is the biogas produced in Btu/day,
- n is the amount of dairy heifer dung supplied to a plug-flow anaerobic digester,
- V_b is the daily output of biogas per animal in ft3/day,
- C_e is the energy content in Btu/ft3.
-

The size of generator can be calculated as follows:

$$P_e = V_{day} * \frac{1_{day}}{24_h} * \eta * \frac{kwh}{3412Btu} \qquad \ldots(22)$$

Where,

- P_e is the size of generator in kW
- η is the overall conversion efficiency.

3.5.3 Finalized Model of Biomass System

The Biomass plant is comprised of all the previously specified sub-models coupled together. In this system, several kinds of animal manure are supplied as inputs to the AD. The model consists of two components: the AD model and the biogas MT generation model. Each of these two models may be executed independently in order to explore the effects of various factors (type of feed, temperature, reactor size, etc.) on the output of the AD system or the effects of methane properties on the output of the MT. The suggested biogas MT model is an universal one that may be used to any other kind of gas. Figure (3.47) depicts the Biomass plant Simulink model.

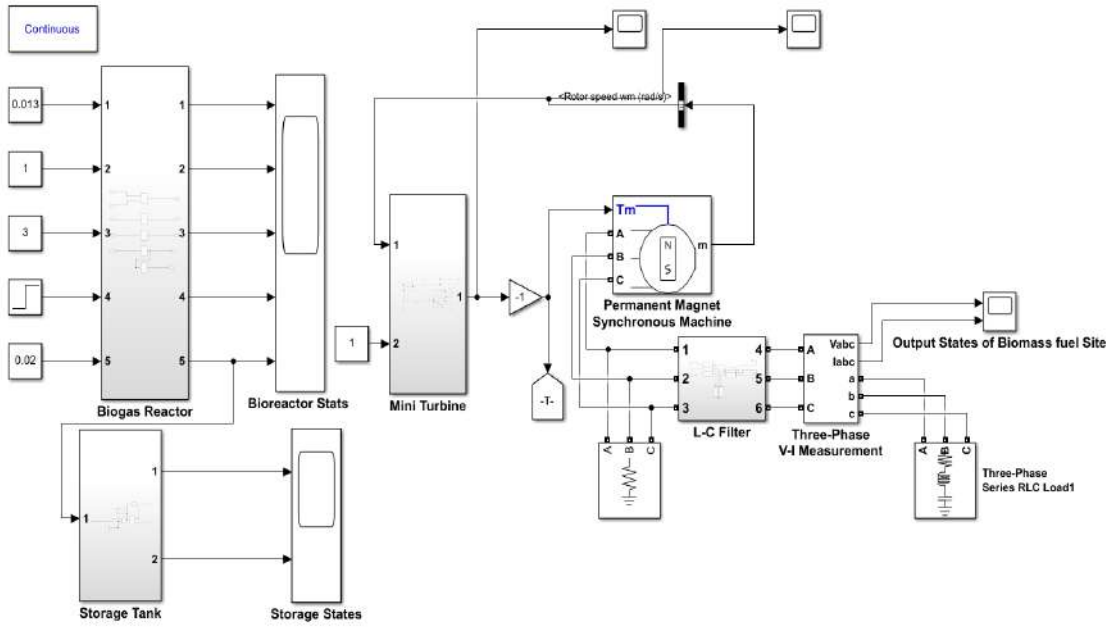

Figure 3.47: Simulink model of the Biomass system.

3.6 LOCATION AND RESOURCES

The preferred location for the hybrid power plant should have enough sun exposure, enough wind energy to control wind turbines, and adequate biomass fuel. The Rahmatpur village (22°29.2'N, 91°27.5'E) in the island sub-district Sandwip of Chattogram district is chosen as the optimal site.

Figure 3.48: Optimal location for the Hybrid Power plant

3.6.1 Resource Analysis

3.6.1.1 Solar Resource Analysis

The clearness Index is a measure of the clearness of the atmosphere [52]. Solar Irradiance (SI) is the power per unit area received from the sun in the form of electromagnetic radiation [52]. The solar GHI throughout the year ranges from 4.250 kWh/m^2/day to 5.510 kWh/m^2/day- to an average of 4.560 kWh/m^2/day [53].

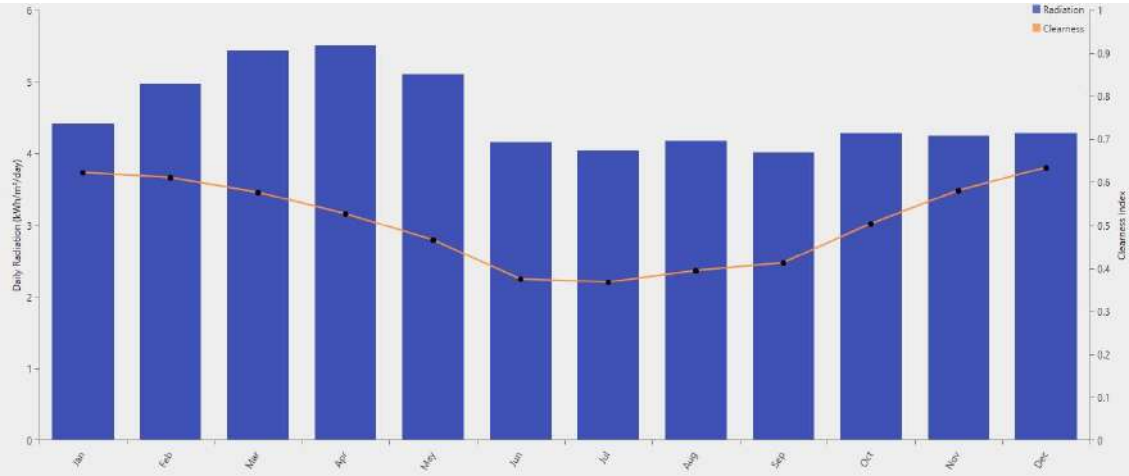

Figure 3.49: Monthly Average Solar GHI (Global Horizontal Irradiance)

3.6.1.2 Wind Resource Analysis

The monthly average wind speed ranges from 4.080 m/s to 7.820 m/s – to a total average of 5.56 m/s [53].

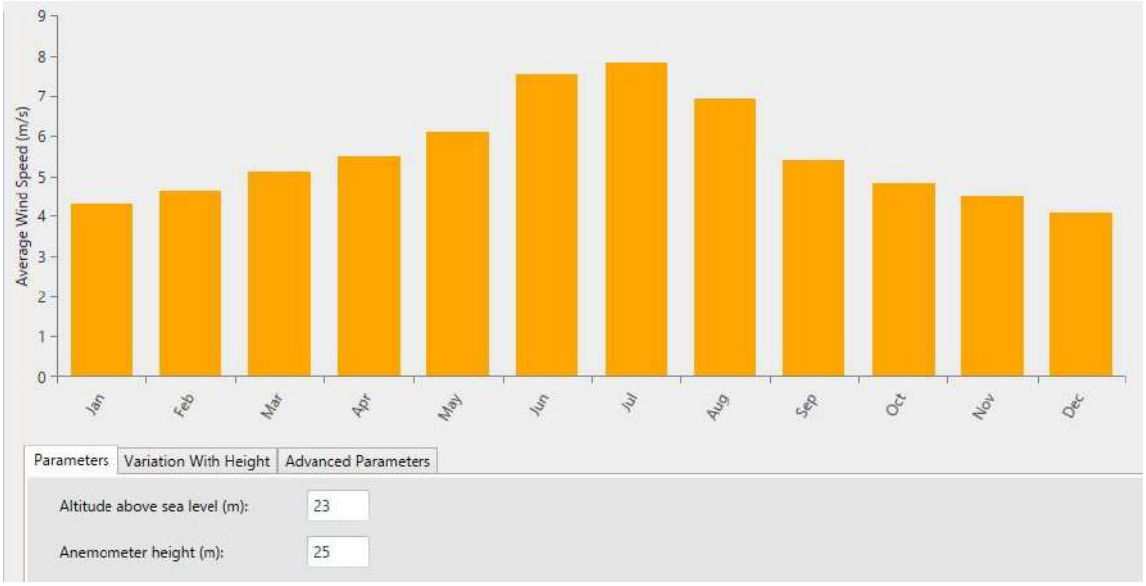

Figure 3.50: Monthly Average Wind Speed with Altitude and Anemometer Height

3.6.1.3 Biomass Resource Analysis

The average monthly biomass output varies from 12 to 22 tons per day, with an overall average of 18 tons per day. These include human and animal faeces, food and vegetable waste, as well as paper and wood. This daily Biomass resource value has been approximated.

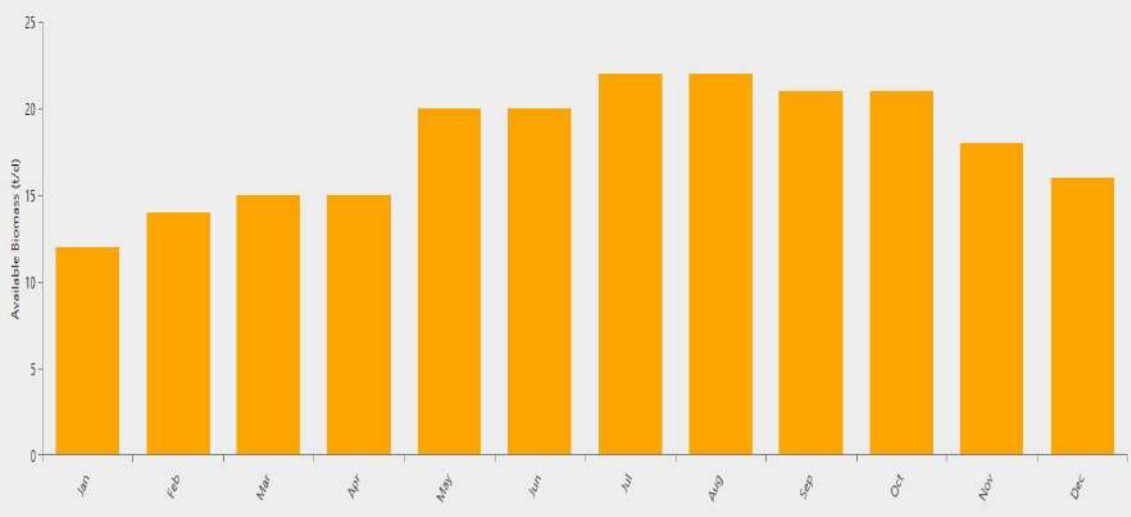

Figure 3.51: Monthly Average Available Biomass

3.6.2 Load Profile

There are two types of Load consumers in this vicinity:

1. Community Load Consumers
2. Commercial Load Consumers

Table 3.2: Daily load profiles

Load Description	Load Type	
	Community	**Commercial**
Daily Consumption	1432 kWh	5240 kWh
Peak Load	119.47 kW	721.5 kW
Average Load	59.67 kW	218.33 kW
Load Factor	0.5	0.3

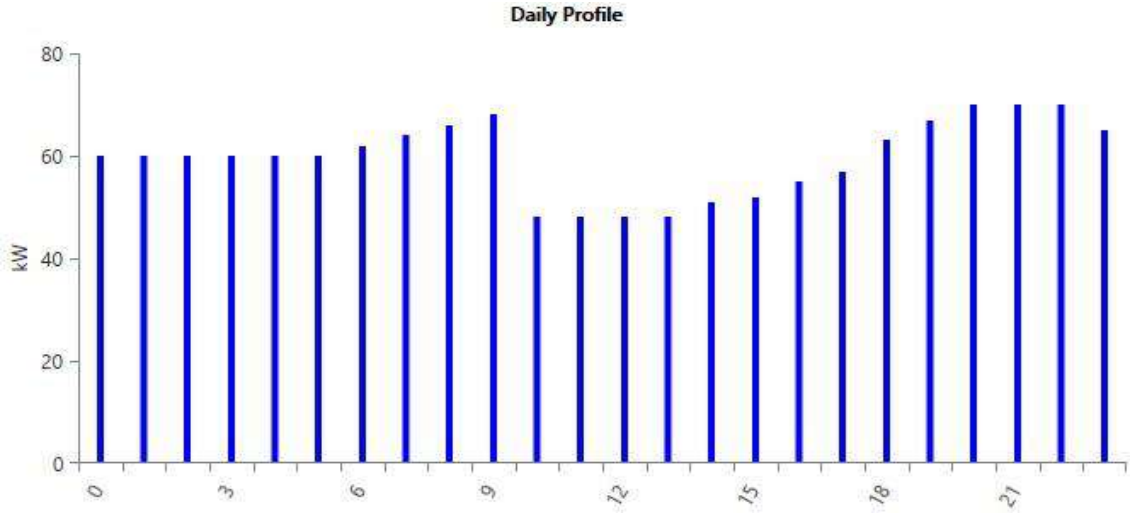

Figure 3.52: Daily average load profile of Community load consumers

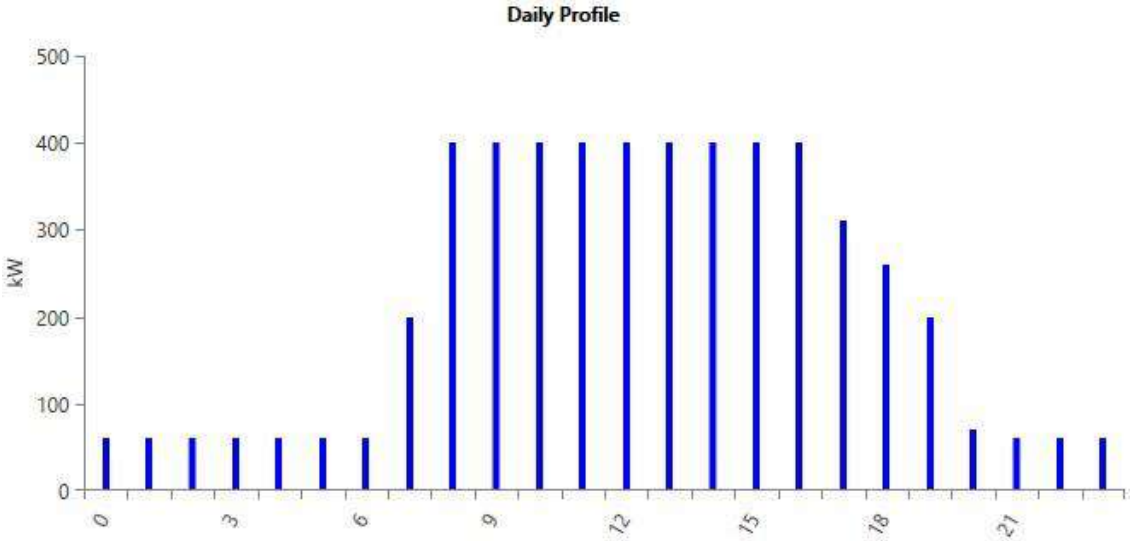

Figure 3.53: Daily average load profile of Commercial load consumers

CHAPTER 4
RESULTS AND DISCUSSIONS

4.1 MATLAB-Simulink

On MATLAB-Simulink, the Hybrid Power Plant has been simulated. The PV, Wind, and Biomass sites are interconnected through the AC Link, which generates Three-Phase AC output to a continuous AC load. The Simulink model of the full hybrid system is seen in Figure (4.1).

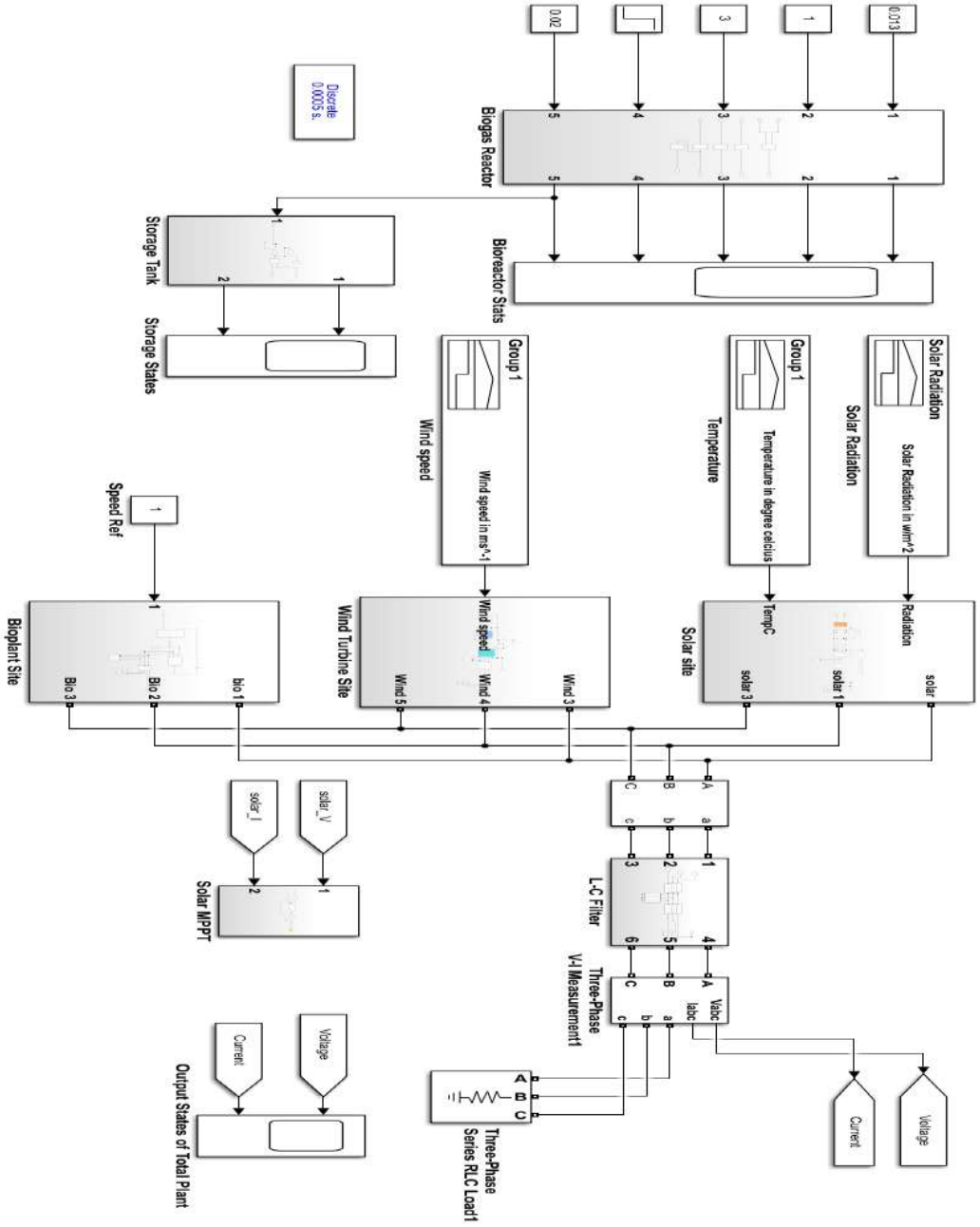

Figure 4.1: Simulink model of the Hybrid Power Plant.

Figures (4.2) and (4.3) illustrate the continuous output voltage and current of the Hybrid Power Plant with a load attached.

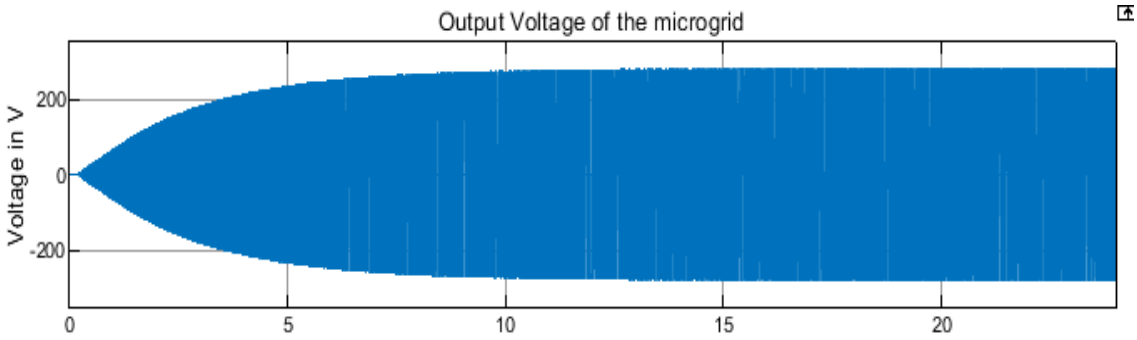

Figure 4.2: Output voltage of the Hybrid Power Plant.

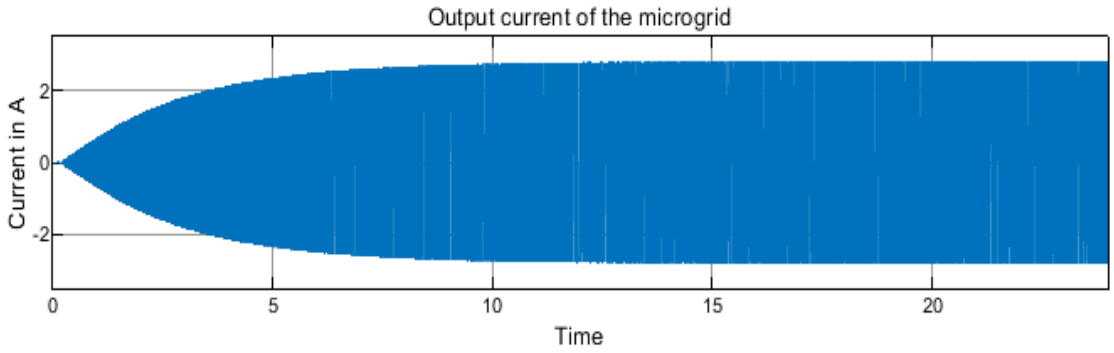

Figure 4.3: Output current of the Hybrid Power Plant.

Figures (4.4) and (4.5) illustrate the fluctuation of Solar Radiation and Temperature with Time as utilized in this simulation. These values were approximated using data from the real world. As the sun sets, Irradiation reaches zero and the temperature drops as well. The PV plant will not generate any power during this period.

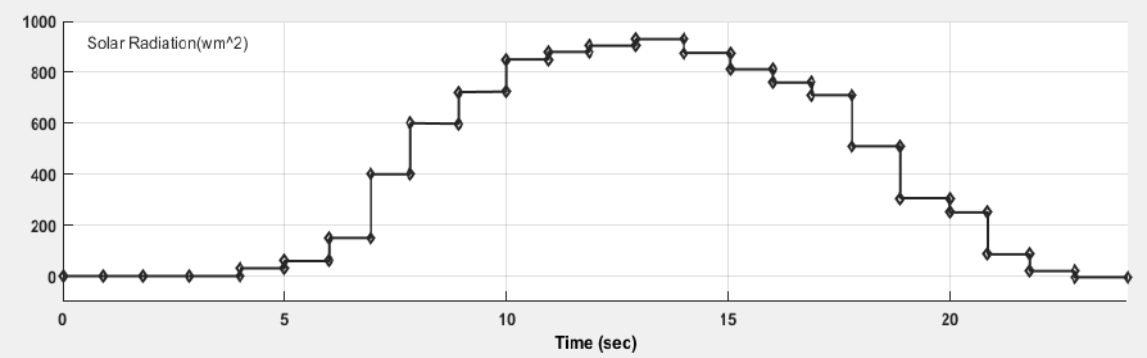

Figure 4.4: Solar Radiation Input in Simulink

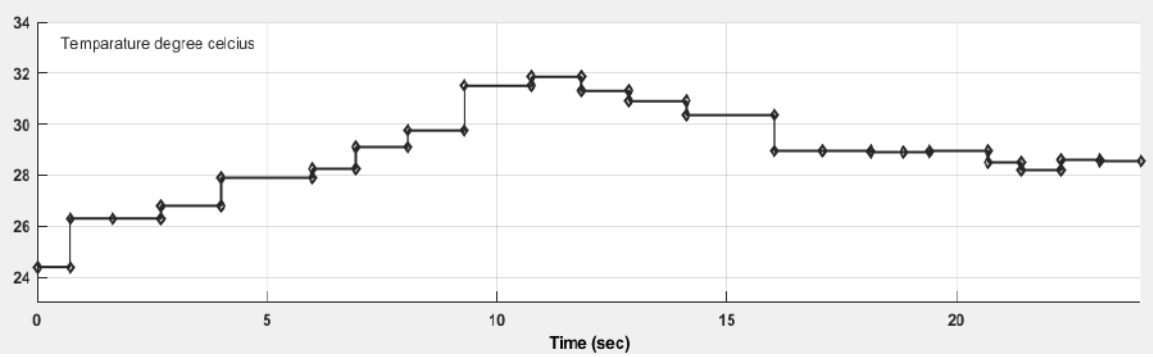

Figure 4.5: Temperature Input in Simulink

Figures (4.6) and (4.7) illustrate the Output Voltage and Current over time at the PV site. Outputs are 0 when irradiation is zero, and they grow as irradiation rises. Around noon, the outputs will be at their peak since the irradiance is around 900 W/m^2. In this Simulink model, each PV module provides a maximum of around 200W of electricity.

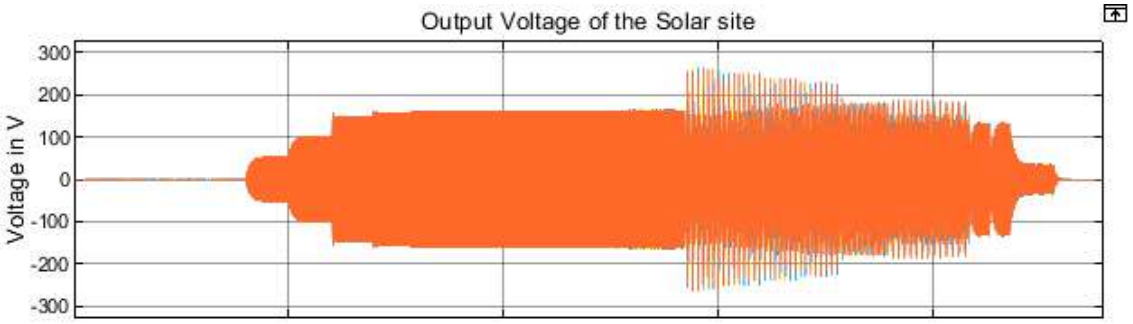

Figure 4.6: Output Voltage of the PV Plant

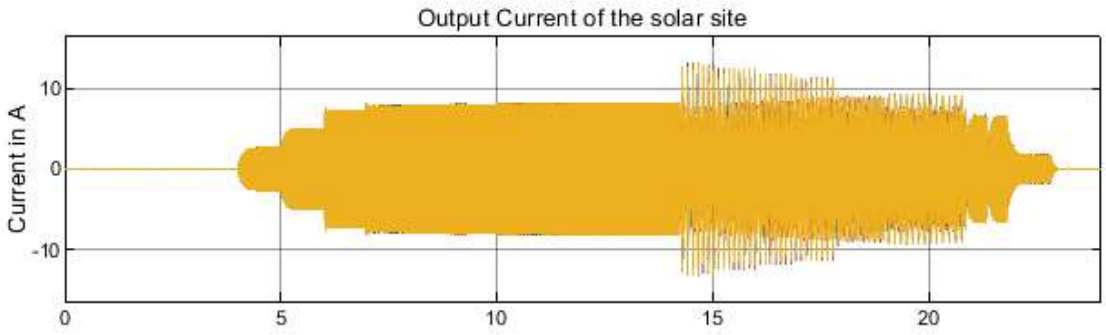

Figure 4.7: Output Current of the PV Plant

Figure (4.8) depicts the Battery Storage attached to the PV system draining while the PV plant is not generating electricity, whereas Figure (4.9) depicts the Battery Storage recharging when the PV Plant is operational again. When there is no Solar Irradiation,

PV modules will cease generating energy, and the Load will begin to draw power from the Battery system, which was being recharged while the modules were operating. When the PV modules resume energy production, the battery system will resume charging.

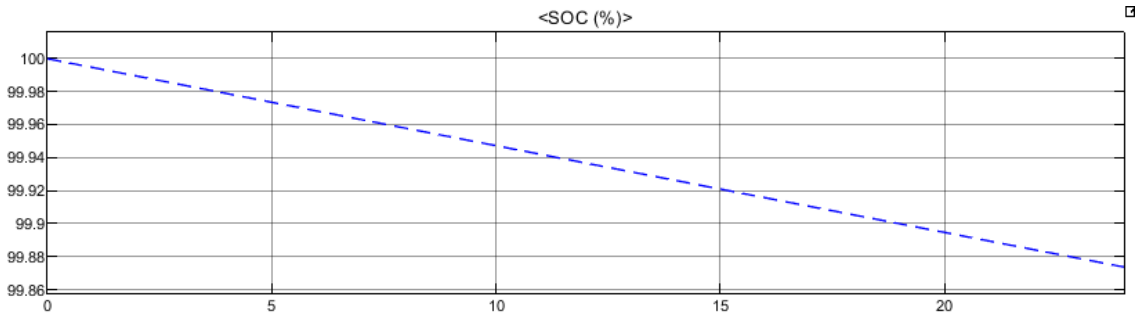

Figure 4.8: Battery Discharge with Time

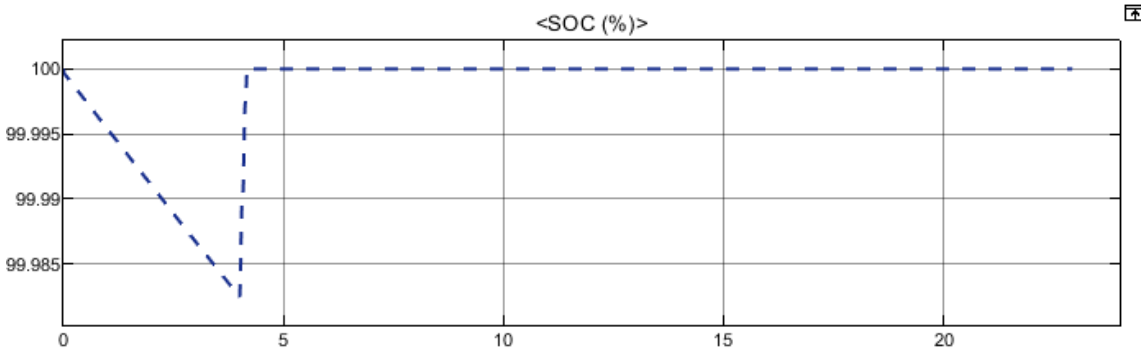

Figure 4.9: Battery Recharging when PV Plant is in Operation

Figure (4.10) depicts the time-dependent fluctuation in Wind Speed used in this simulation. This figure was also approximated using data from the real world. The power generated by the turbine will vary according on wind speed, since faster winds will result in more electrical production.

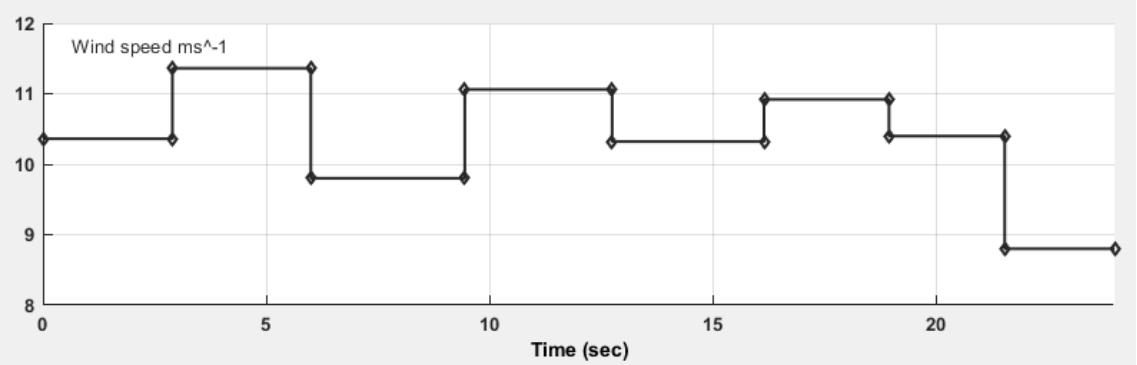

Figure 4.10: Wind Speed Input in Simulink

Figures (4.11) and (4.12) depict the Output Voltage and Current produced by the Power Plant's Wind Turbines. These outputs fluctuate according on wind speed. When the wind speed is around 12 meters per second, the wind turbine in this Simulink model will generate a maximum of 20 kW of electricity.

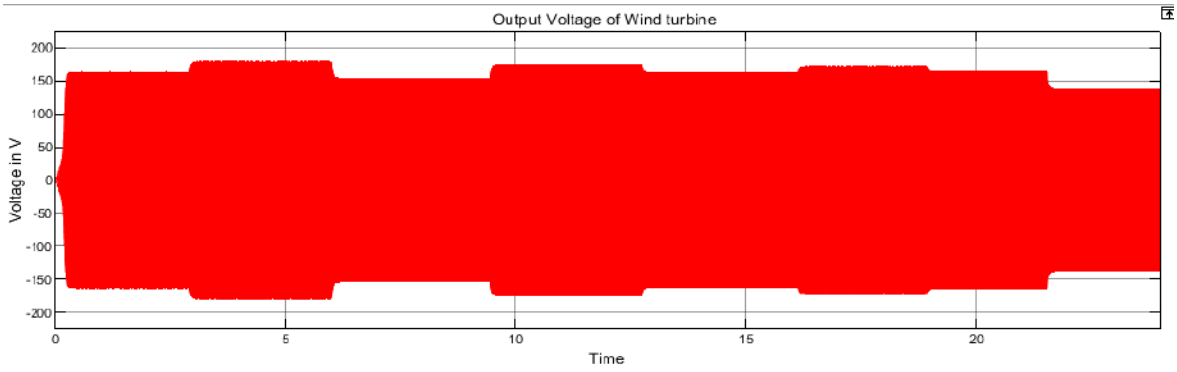

Figure 4.11: Output voltage of the Wind System.

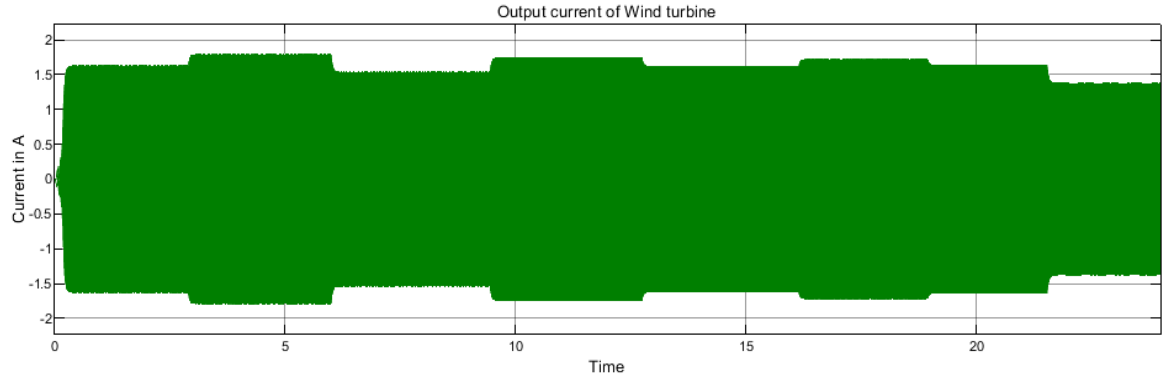

Figure 4.12: Output current of the Wind System.

Figure (4.13) illustrates the relationship between reactor temperature and methane production. It can be noted that raising the Reactor's temperature increases both the amount and duration of methane generation.

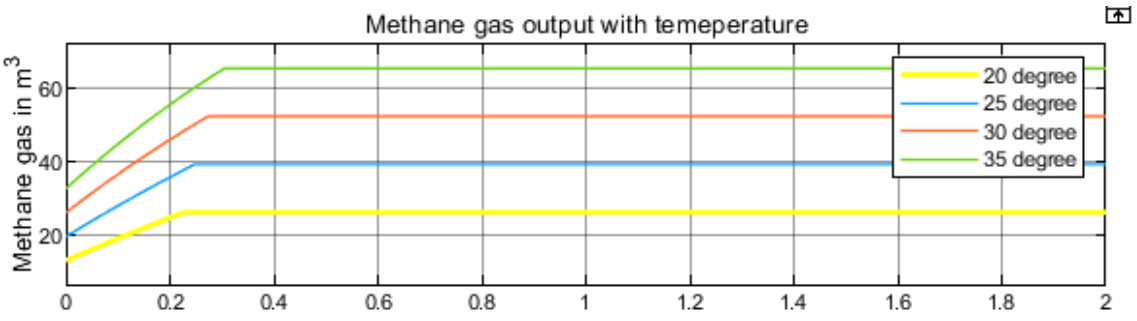

Figure 4.13: Methane Output of the Bioreactor.

Figures (4.14) and (4.15) depict the Biomass site's Output Voltage and Current. Variable depends on the quantity of methane gas supplied to the turbine.

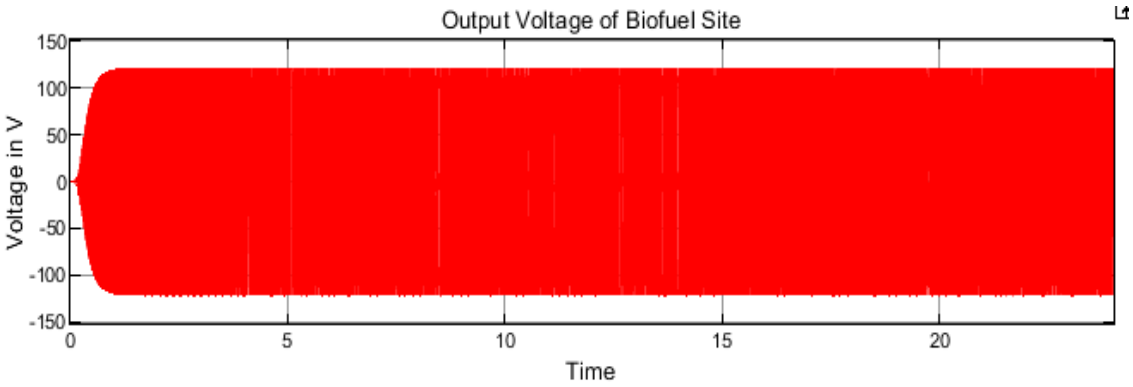

Figure 4.14: Output voltage of the Biomass Plant.

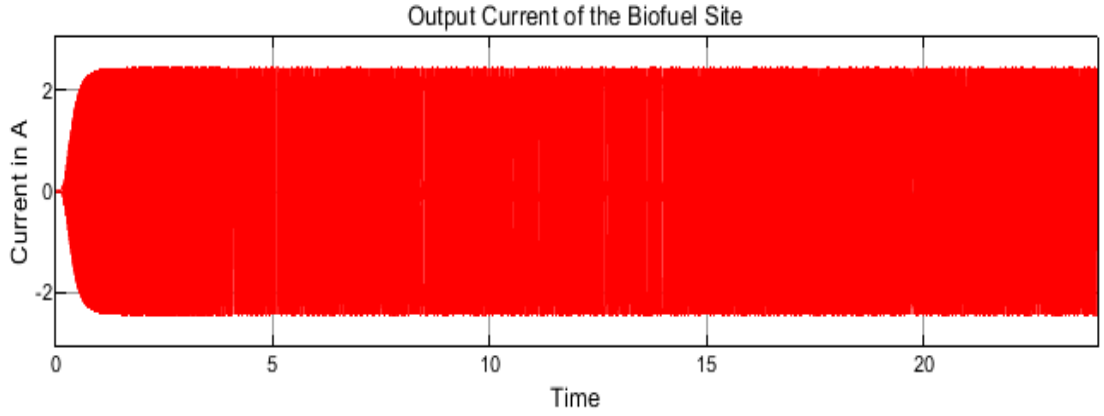

Figure 4.15: Output current of the Biomass Plant.

4.2 HOMER Pro

4.2.1 Optimal System Report

In the HOMER optimized microgrid model PV System produces 623,646 kWh/Year, which is 23.6% of the entire production. Wind System produces 525,414 kWh/Year, which is 19.9% of the entire production. Biomass System produces 1,488,859 kWh/Year, which is 56.4% of the entire production.

The Annual consumption is 2,434,949 kWh. Annual production is 2,637,919 kWh. Leaving 68,764 kWh of excess electricity a year, which is 2.6% of the entire production. We can contribute this energy to the grid if possible, or a scheduled plant turning-off could be another solution to get rid of this excess electricity.

Table (4.1) displays the components necessary to construct a Microgrid based on the previously specified load. The schematics of these individual components will be included in "Appendix-II."

Table 4.1: **System Architecture**

Component	Name	Size	Unit
Generator	Generic 500kW Biogas Genset	500	kW
PV	Generic Flat Plate PV	421	kW
Battery Storage	Generic 1kWh Lead Acid	886	Strings
Wind Turbine	Generic 10kW Turbine	19	Ea.
System Converter	Generic System Converter	495	kW
Dispatch Strategy	HOMER Cycle Charging		

Tables (4.2) to (4.6) represent the annual operating data of each component, including specifics such as daily and annual total production, rated capacity, and levelized cost for each Plant.

Table 4.2: PV Plant Statistics

Characteristics	Value	Units
Minimum Output	0	kW

Maximum Output	417	kW
PV Penetration	2,506	%
Hours of Operation	4,369	Hours/Year
Levelized Cost	0.137	$/kWh
Rated Capacity	421	kW
Mean Output	71.2	kW/Hour
Capacity Factor	16.9	%
Total Production	623,646	kWh/Year

Table 4.3: Wind System Statistics

Characteristics	Value	Units
Minimum Output	0	kW
Maximum Output	190	kW
Wind Penetration	21.6	%
Hours of Operation	7,594	Hours/Year
Levelized Cost	0.177	$/kWh
Total Rated Capacity	190	kW
Mean Output	60	kW/Hour
Capacity Factor	31.6	%
Total Production	525,414	kWh/Year

Table 4.4: Biogas Plant Statistics

Characteristics	Value	Units
Electrical Production	1,488,859	kWh/Year
Mean Electrical Output	359	kW
Minimum Electrical Output	250	kW
Maximum Electrical Output	500	kW
Fuel Consumption	4,550	Tons/Year
Specific Fuel Consumption	2.14	Kg/kWh
Fuel Energy Input	4,866,383	kWh/Year
Mean Electrical Efficiency	30.6	%
Hours of Operation	4,151	Hours/Year

Number of Starts	1,099	Starts/Year
Operational Life	4.82	Year
Capacity Factor	34	%
Fixed Generation Cost	61.3	$/Hour
Marginal Generation Cost	0	$/kWh

Table 4.5: Battery Storage System Statistics

Characteristics	Value	Units
Batteries	1,772	Quantity
String Size	2	Batteries
Strings in Parallel	886	Strings
Bus Voltage	24	V
Average Energy Cost	0	$/kWh
Energy In	424,521	kWh/Year
Energy Out	339,791	kWh/Year
Storage Depletion	195	kWh/Year
Losses	84,925	kWh/Year
Annual Throughput	379,898	kWh/Year
Autonomy	3.83	Hour
Storage Wear Cost	0.419	$/kWh
Nominal Capacity	1,773	kWh
Usable Nominal Capacity	1,064	kWh
Lifetime Throughput	1,417,600	kWh
Expected Life	3.73	Year

Table 4.6: System Converter Statistics

Characteristics	Value	Units
Hours of Operation	5,914	Hours/Year
Energy Out	705,221	kWh/Year
Energy In	742,338	kWh/Year
Losses	37,117	kWh/Year
Capacity	495	kW

Mean Output	80.5	kW
Minimum Output	0	kW
Maximum Output	445	kW
Capacity Factor	16.3	%

Figures (4.16) to (4.21) depict the Hourly and Daily Output of the PV-Wind-Biomass Plants, Battery Storage System, and System Converters, respectively.

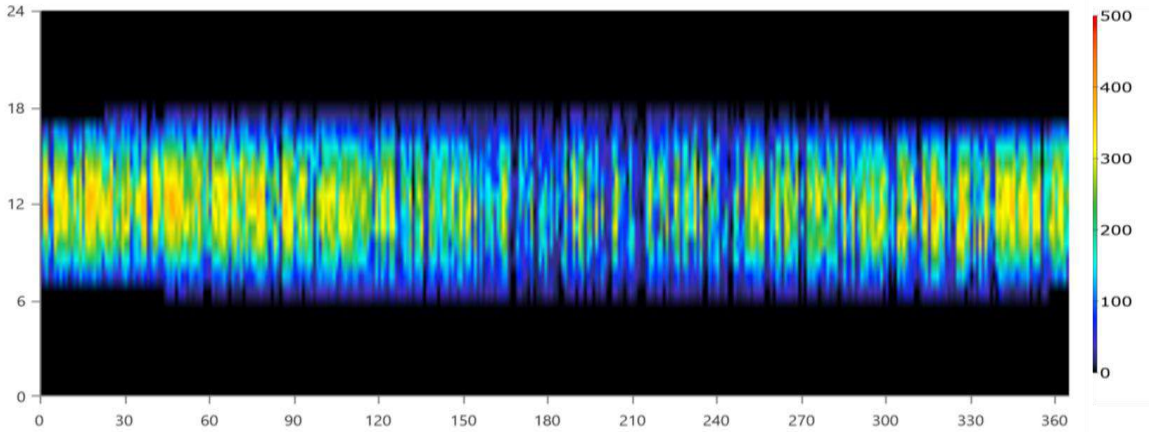

Figure 4.16: Hourly and Daily output of PV Plant (kW).

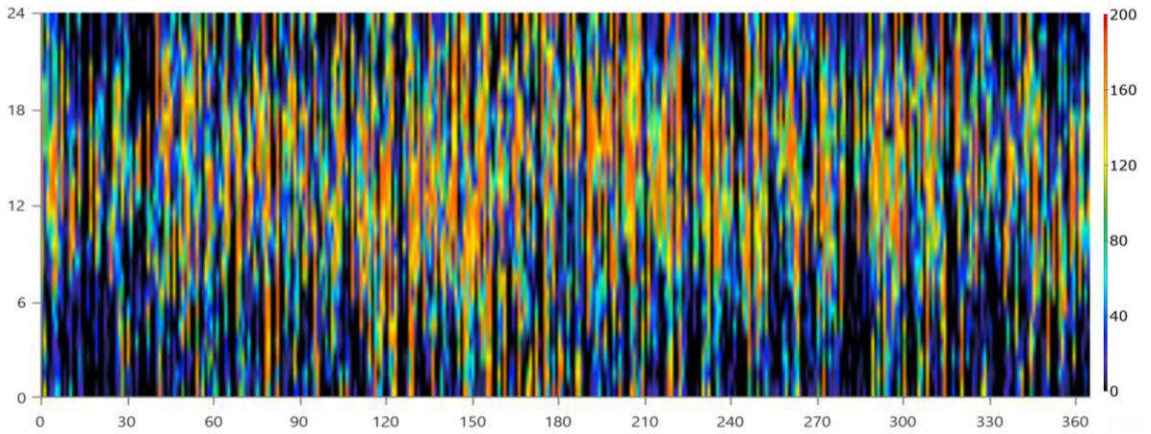

Figure 4.17: Hourly and Daily output of Wind System (kW).

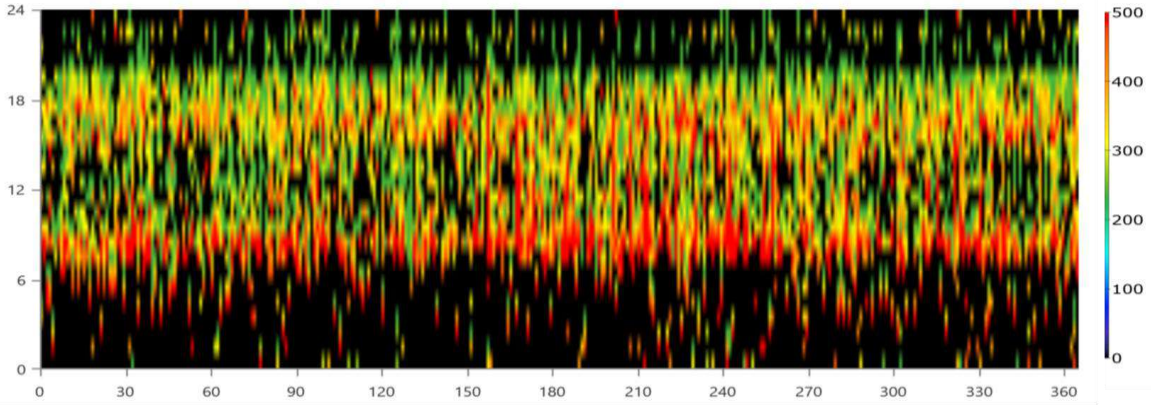

Figure 4.18: Hourly and Daily output of Biomass generator (kW).

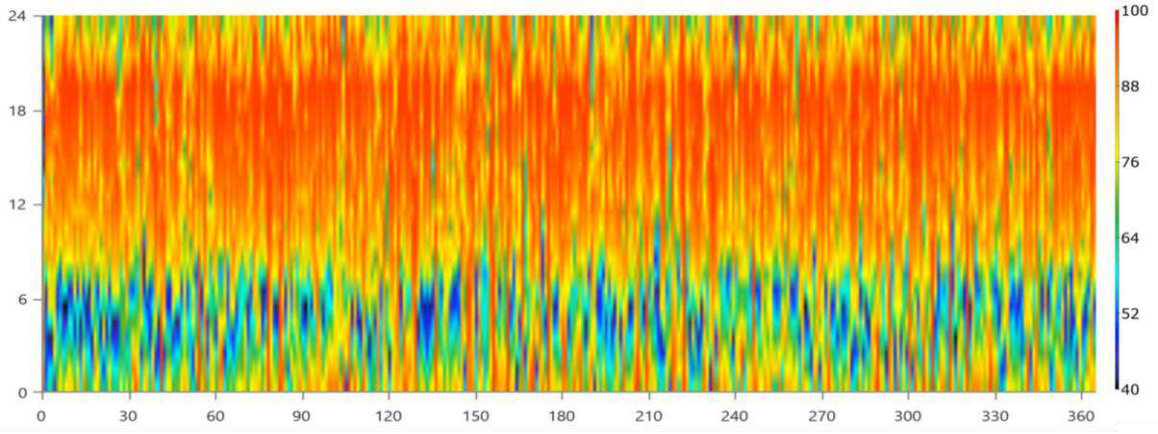

Figure 4.19: Hourly and Daily state of charge of the Battery System (%).

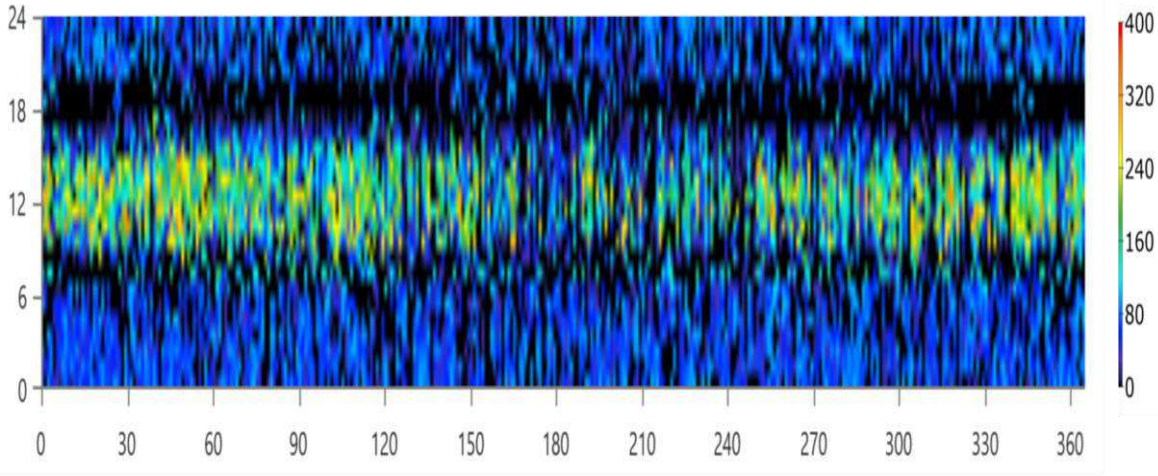

Figure 4.20: Hourly and Daily Inverter output of System Converter (kW).

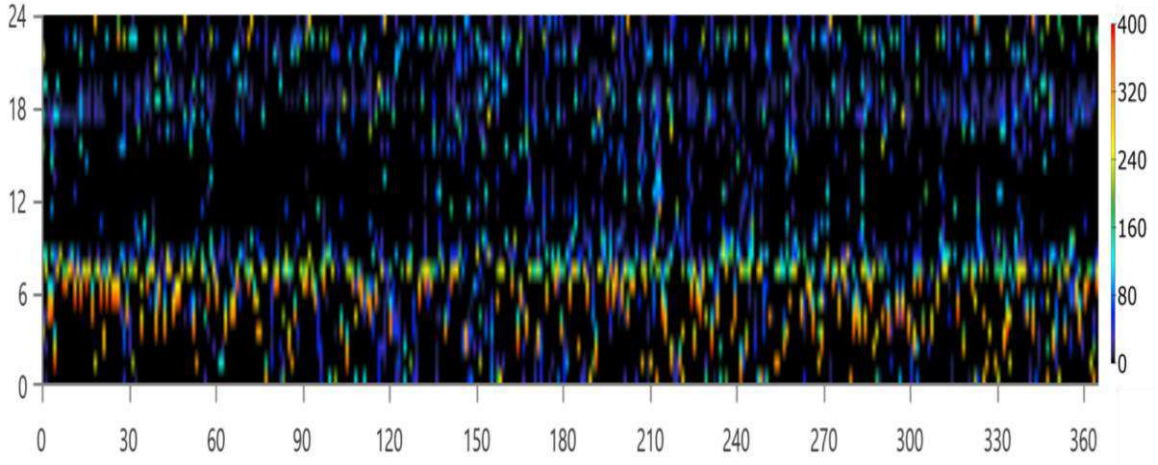

Figure 4.21: Hourly and Daily Rectifier output of System Converter (kW).

4.2.2 Feasibility Analysis

Table (4.7) shows the cost summary of each component in the Hybrid Power Plant with an operational life of 25 years. Here we can see that several components need to be replaced within the project lifetime and we can salvage the old components, recuperating some of the cost.

Table 4.7: Cost Summary of Each Component of the Hybrid Power Plant over 25 years

Name	Capital ($)	Operating Cost ($)	Replacement Cost ($)	Salvage ($)	Resource ($)	Total ($)
Generic 10kW Wind Turbine	950,000	122,811	302,865	-170,685	0	1.2 million
Generic 1kWh Lead Acid Battery	531,600	229,076	1.61 million	-38,246	0	2.34 million
Generic 500kW Biogas Genset	1.5 million	396,660	1.47 million	-121,463	1.21 million	4.46 million
Generic 1kW Flat Plate PV	1.05 million	54,439	0	0	0	1.11 million
System Converter	148,465	0	62,990	-11,855	0	199,599
Overall System	4.18 million	803,306	3.45 million	-342,250	1.21 million	9.31 million

The economic comparison between this Hybrid Power Plant, a Natural Gas-Based Power Plant, and an Oil-Based Power Plant is presented in Table (4.8). Each of these power plants was simulated using HOMER Pro under identical load conditions and for a duration of 25 years. Oil-based power plants are the most expensive due to the rising cost of fuel. Natural gas-based power plants have the lowest total cost, followed closely by hybrid power plants. The Hybrid Power Plant has a significantly higher initial capital cost than the other two power plants.

Table 4.8: Economical Comparison over 25 Years (Each Plant has a capacity of 1MW and under the same load)

Characteristics	Hybrid Power Plant	Natural Gas based Power Plant	Oil Based Power Plant	Unit
Total Net Present Cost	9.31 million	8.81 million	12.62 million	$
Initial Capital Expenses	4.18 million	1.36 million	500,000	$
Operational Expenses	396,660	576,681	1.13 million	$
Levelized Cost of Energy	0.296	0.28	0.401	$/kWh
Fuel Consumption	4,550 Tons	1,199,346 Cubic Meters	850,135 Litre	Per Year

Table (4.9) compares the annual emissions of the power plants. We can see that there is a substantial difference between Hybrid Power Plant and the other two in terms of their emissions to the environment. This makes the Hybrid Power Plant an appealing option to fossil fuel-based power plants of any sort.

Table 4.9: Emission Comparison over 25 Years (Each Plant has a capacity of 1MW and under the same load)

Name	Hybrid Power Plant	Natural Gas based Power Plant	Oil Based Power Plant	Units
Carbon Dioxide	820	1,731,770	2,229,245	Kg/Year
Carbon Monoxide	9.10	379,197	11,533	Kg/Year
Unburned Hydrocarbons	0	0	612	Kg/Year
Particulate Matter	0	0	98.6	Kg/Year
Sulphur Dioxide	0	0	5,449	Kg/Year
Nitrogen Oxides	5.69	75,839	2,210	Kg/Year

CHAPTER 5

CONCLUSIONS AND FUTURE WORKS

5.1 Conclusions

This study has designed and simulated a battery-powered PV/wind/biomass hybrid system. Separate examinations have also been performed. Using Simulink, the whole hybrid system has been constructed and simulated under a variety of weather conditions. To get the MPP in the PV system, the perturb and observe (P&O) MPPT strategy and a buck-boost converter were used to control the duty cycle. A PMSG is employed in the wind turbine system to convert the wind turbine's mechanical power output to electrical power. Using a battery storage system and a bidirectional DC-DC converter, surplus power was saved and sent to the load. Response of the proposed Biomass Plant to fluctuating operation is efficient and quick. This model is comprised of three distinct models that depict a biogas reactor, a Methane-producing system, and a storage system. Depending on simulation requirements, each model may be deployed individually or collectively to simulate the biogas power plant. After the Economical and Emission comparison with Fossil Fuel based power plants, Hybrid Power Plant can be considered a proper alternative as an energy source due to nearly similar cost and significantly less emissions.

5.2 Limitations

The study is done partially by HOMER Pro Software of version 3.14.2, which has its own algorithm of simulation and computational system, which may have effects on the outcomes. A certain range of study setups has been given for the study.

5.3 Future Works

- Adding another renewable source, such as hydropower, with a new power management system might be a useful issue for the future.
- In the future, an alternative and effective algorithm for tracking MPP may be investigated.
- Inputs for a more effective and current cost analysis of the components may be included into the HOMER simulation process.

REFERENCES

[1] Muralikrishna, M., and V. Lakshminarayana. "Hybrid (solar and wind) energy systems for rural electrification." ARPN Journal of Engineering and Applied Sciences 3, no. 5 (2008):50-58.

[2] Kjellander, Matilda, and Anders Tengvall. "Design of a small-scale hybrid photovoltaic and wind energy system." BSc thesis, Halmstad University, 2014.

[3] Faisal, Hiba. "Hybrid wind-solar electric power system." BSc diss., University of Khartoum, 2014.

[4] EIA, US. "Annual energy outlook 2022." US Energy Information Administration, Washington, DC (2022). Accessed May 01, 2022.

[5] GER22. "Ember's Global Electricity Review 2022". https://ember-climate.org/insights/research/global-electricity-review-2022/. Accessed May 01, 2022.

[6] Negi, Swati, and Lini Mathew. "Hybrid renewable energy system: a review." International Journal of Electronic and Electrical Engineering, Vol. 7, pp. 535-542 (2014).

[7] Kumar, Sandeep. "Modelling and simulation of hybrid Wind/Photovoltaic Stand-alone generation system." Master's thesis, National Institute of Technology, 2014.

[8] Patel, Sanjukta. "Modelling and control of a grid-connected wind-PV hybrid generation system." Master's thesis, National Institute Technology, 2014.

[9] MHUSA, NICHOLAUS JOSEPH. "Modelling and Control of Photovoltaic-Wind Hybrid Power System Using a Neural-Fuzzy Controller." PhD diss., COHRED, JKUAT, 2016.

[10] Ovaska, Seppo. "Maximum power point tracking algorithms for photovoltaic applications." PhD diss., Aalto University, 2010.

[11] Rolan, Alejandro & Luna, A. & Guzmán, Gerardo & Aguilar, Daniel & Azevedo, Gustavo. (2009). "Modeling of a variable speed wind turbine with a Permanent Magnet Synchronous Generator". IEEE International Symposium on Industrial Electronics. 734 - 739. 10.1109/ISIE.2009.5218120.

[12] Breza, Paraskevi. "Modelling and simulation of a PV generator for applications on distributed generation systems." PhD diss., TU Delft, Delft University of Technology, 2013.

[13] Dzimano, Gwinyai. "Modelling of photovoltaic systems." PhD diss., The Ohio State University, 2008.

[14] Villalva, Marcelo & Gazoli, Jonas & Filho, Ernesto. (2009). "Comprehensive Approach to Modeling and Simulation of Photovoltaic Arrays". Power Electronics, IEEE Transactions on. 24. 1198 - 1208. 10.1109/TPEL.2009.2013862.

[15] Rekioua, Djamila & Matagne, Ernest. (2012). "Optimization of photovoltaic power systems: Modelization, Simulation and Control". 10.1007/978-1-4471-2403-0.

[16] Blazev, Anco S. "Photovoltaics for commercial and utilities power generation". Lulu Press, Inc, 2013. ISBN: 978-1439856314

[17] Zini, G. & Tartarini, Paolo. (2015). “Solar hydrogen energy systems: Science and technology for the hydrogen economy”. 10.1007/978-88-470-1998-0.

[18] Gangopadhyay, Utpal & Jana, Sukhendu & Das, Sayan. (2013). “State of Art of Solar Photovoltaic Technology”. Journal of Energy. 764132. 10.1155/2013/764132.

[19] De Bastiani, Michele. "The Stability of Third Generation Solar Cells." PhD diss., University of Padova, (2016).

[20] "Reported timeline of solar cell energy conversion efficiencies." National Renewable Energy Laboratory (NREL) Home Page. 2022. Accessed May 04, 2022.

[21] Villalva, Marcelo & Gazoli, Jonas & Filho, Ernesto. (2009). “Comprehensive Approach to Modeling and Simulation of Photovoltaic Arrays. Power Electronics”. IEEE Transactions on. 24. 1198 - 1208. 10.1109/TPEL.2009.2013862.

[22] Said, S. & Massoud, Ahmed & Benammar, Mohieddine & Ahmed, S.. (2012). “A matlab/simulink based photovoltaic array model employing simpowersystems toolbox”. Journal of Energy and Power Engineering. 6. 1965-1975.

[23] Ramos, Jose & Martín, J.J. & Belver, I. & Larrañaga Lesaca, JM & Zulueta, Ekaitz & Pérez, E.. (2010). “Modelling of Photovoltaic Module”. Renewable Energy and Power Quality Journal. 1. 1186-1190. 10.24084/repqj08.619.

[24] Sai, Sumathi & Kumar, L Ashok & Paneerselvam, Surekha. (2015). “Application of MATLAB/SIMULINK in Solar PV Systems”. 10.1007/978-3-319-14941-7_2.

[25] Tan, Yun Tiam. "Impact on the power system with a large penetration of photovoltaic generation." PhD diss., University of Manchester, 2004.

[26] M'Sirdi, Nacer, Aziz Namaane, Robert J. Howlett, and Lakhmi C. Jain, eds. “Sustainability in Energy and Buildings”. Proceedings of the 3rd International Conference on Sustainability in Energy and Buildings (SEB´11). Vol. 12. Springer Science & Business Media, 2012.

[27] Tiwari, G. & Mishra, Rajeev & Solanki, S.C.. (2011). “Photovoltaic modules and their applications: A review on thermal modelling”. Applied Energy. 88. 2287-2304. 10.1016/j.apenergy.2011.01.005.

[28] UmaShankar Patel, Ms. Dhaneshwari Sahu, Deepkiran Tirkey, “Maximum Power Point Tracking Using Perturb & Observe Algorithm and Compare With another Algorithm”, International Journal of Digital Application & Contemporary research, Volume 2, Issue 2, September 2013.

[29] Faranda, Roberto & Leva, S.. (2008). “Energy comparison of MPPT techniques for PV Systems”. Journal of Electromagnetic Analysis and Applications. Vol 3.

[30] Karuna, Kartik. "Optimized MPPT implementation for Dye-sensitized Solar cells: Maximum Power Point Tracking for DCSs." Master’s thesis, KTH Royal Institute of Technology, (2015).

[31] Jimenez, Emil & Ortiz-Rivera, Eduardo & Gil-Arias, Omar. (2008). “A dynamic maximum power point tracker using sliding mode control”. Control and Modeling for Power Electronics, 2008. COMPEL 2008. 11th Workshop on. 1 - 5. 10.1109/COMPEL.2008.4634685.

[32] Dwivedi, Laxmi & Yadav, Prabhat & Saket, Dr. R.K.. (2016). “MATLAB based modelling and maximum power point tracking (MPPT) method for photovoltaic system under partial shading conditions”. International Research Journal of Engineering and Technology (IRJET). vol-3.

[33] Mohan, Ned, and Tore M. Undeland. “Power electronics: converters, applications, and design”. John Wiley & Sons, 2007. ISBN : 978-0471226932

[34] Ortiz-Rivera, Eduardo. (2008). “Maximum power point tracking using the optimal duty ratio for DC-DC converters and load matching in photovoltaic applications”. Conference Proceedings - IEEE Applied Power Electronics Conference and Exposition - APEC. 987 - 991. 10.1109/APEC.2008.4522841.

[35] Tzanakis, Iakovos. "Combining Wind and Solar Energy to Meet Demands in the Built Environment." PhD diss., Master Thesis, Energy Systems Research Unit. University of Strathclyde, Glasgow, UK, 2005-2006, 2006.

[36] V. Ramakrishnan and S.K. Srivatsa , 2007. “Mathematical Modeling of Wind Energy Systems”. Asian Journal of Information Technology, 6: 1160-1166.

[37] Qazi, Sajid Hussain, M. W. Mustafa, and Irfan Ahmed Bajkani. "Simulation of PMSG based Wind Energy System with Multi-Level NPC Converter." 4th International Multi-Topic Conference. MUET, Pakistan. Accepted Papers (2011): 84.

[38] Wang, Chia-Nan & Lin, Wen-Chang & Le, Khoa. (2014). “Modelling of a PMSG Wind Turbine with Autonomous Control”. Mathematical Problems in Engineering. 2014. 1-9. 10.1155/2014/856173.

[39] Cheng, Wei. "Incremental Conductance Algorithm for Maximum Wind Power Extraction Using Permanent Magnet Synchronous Generator." Master’s thesis, University of Houston, 2013.

[40] Al-Qasem, Ola Subhi Waheed. "Modelling and Simulation of Lead-Acid Storage Batteries within Photovoltaic Power Systems." PhD diss., An-Najah National University, 2012.

[41] Zhang, Junhong. "Bidirectional DC-DC power converter design optimization, modelling and control." PhD diss., Virginia Polytechnic Institute and State University, 2008.

[42] Saeed, Mohammed & Fawzy, Samaa & El-Saadawi, Magdi. (2018). “Modeling and simulation of biogas-fueled power system”. International Journal of Green Energy. 16. 1-27. 10.1080/15435075.2018.1549997.

[43] Liao, Q., J. Chang, C. Herrmann, and A. Xia. 2018b. “Bioreactors for microbial biomass and energy conversion”. Springer. doi:10.1007/978-981-10-7677-0.

[44] Hagos, Kiros & Zong, Jianpeng & Li, Dongxue & Liu, Chang & Lu, Xiaohua. (2017). “Anaerobic co-digestion process for biogas production: Progress, challenges and perspectives”. Renewable and Sustainable Energy Reviews. 76. 1485-1496. 10.1016/j.rser.2016.11.184.

[45] Neshat, Soheil & Mohammadi, Maedeh & Najafpour, Ghasem & Lahijani, Pooya. (2017). “Anaerobic co-digestion of animal manures and lignocellulosic residues as

a potent approach for sustainable biogas production". Renewable and Sustainable Energy Reviews. 79. 308-322. 10.1016/j.rser.2017.05.137.

[46] Pathmasiri, Kalpani & Haugen, Finn Aakre & Gunawardena, Sanja. (2013). "Simulation of a Biogas Reactor for Dairy Manure". Annual Transactions of IESL. The Institution of Engineers, Sri Lanka. 394-398.

[47] A. Husain, "Mathematical models of the kinetics of anaerobic digestion—a selected review", Biomass and Bioenergy, Volume 14, Issues 5–6, 1998, p. 561-571, ISSN 0961-9534

[48] Haugen, F., R. Bakke, and B. Lie. 2012b. "Mathematical modelling for planning optimal operation of a biogas reactor for dairy manure". Dublin: IWA World Congress on Water, Climate and Energy. May. 14–18.

[49] Guda, S. 2005b. "Modelling and power management of a hybrid wind microturbine power generation system". MSc diss., Montana State University.

[50] Duan, Zhaoyang & Cruz Bournazou, Mariano & Kravaris, Costas. (2017). "Dynamic Model Reduction for Two-Stage Anaerobic Digestion Processes". Chemical Engineering Journal. 327. 10.1016/j.cej.2017.06.110.

[51] Khorshidi, Abbas & Zolfaghari, Mahdi & Akhavanhejazi, Maryam. (2014). "Dynamic Modeling and Simulation of Microturbine Generating System for Stability Analysis in Microgrid Networks". International Journal of Sciences: Basic and Applied Research (IJSBAR). 5. 663-670.

[52] "HOMER Pro User Manual": https://www.homerenergy.com/products/pro/docs/latest/index.html : Accessed April 24, 2022.

[53] "NASA Prediction of Worldwide Energy Resource (POWER) Database": https://power.larc.nasa.gov/ : Accessed April 24, 2022.

APPENDIX-I

MATLAB Code for Perturb & Observe:

```
function Vref = RefGen(V, I)

Vrefmax = 363;
Vrefmin = 0;
Vrefinit = 300;
deltaVref =1;
persistent Vold Pold Vrefold;

dataType = 'double';

if isempty(Vold)
   Vold = 0;
   Pold = 0;
   Vrefold = Vrefinit;
end

P = V*I;
dV = V-Vold;
dP = P-Pold;
if dP ~= 0
   if dP<0
      if dV<0
         Vref = Vrefold + deltaVref;
      else
         Vref = Vrefold - deltaVref;
      end
   else
      if dV<0
         Vref = Vrefold - deltaVref;
      else
         Vref = Vrefold + deltaVref;
      end
   end
else Vref = Vrefold;
end
if Vref >= Vrefmax | Vref <= Vrefmin
   Vref = Vrefold;
end
Vrefold = Vref;
Vold = V;
Pold = P;
```

APPENDIX-II

Table 1: PV Panel Schematics

Characteristics	Quantity
Panel Type	Generic Flat Plate
Rated Capacity	1 kW
Temperature Coefficient	-0.55
Nominal Operating Cell Temperature	40℃
Efficiency	15.5%
Manufacturer	Generic
Lifetime	25 Years
Ground Reflection	20%
De-Rating Factor	88%
Panel Slope	24.37°

Table 2: Wind Turbine Schematics

Characteristics	Quantity
Type	Generic Wind Turbine
Rated Capacity	10 kW
Manufacturer	Generic
Hub Height	40 meters
Lifetime	20 Years
Start-up Wind Speed	3 m/s
Rated Wind Speed	14 m/s
Cut Out Wind Speed	21 m/s
Power Regulation	Pitch Regulated with Variable Speed

Table 3: Biogas Generator Schematics.

Characteristics	Quantity
Type	Generic 500 kW Biogas Genset
Capacity	500 kW
Fuel	Biogas
Minimum Load Ration	50%

Lifetime	20,000 Hours
Emissions	CO_n – (2g/kg Fuel), NO_n (1.5g/kg Fuel)
Lower Heating Value	5.5 MJ/kg

Table 4: System Converter Schematics.

Characteristics	**Quantity**
Type	Generic System Converter
Inverter Efficiency	95%
Inverter Lifetime	15 Years
Rectifier Efficiency	95%
Rectifier Lifetime	15 Years
AC Generator Connection	Parallel with AC Generator

Table 5: Storage System Schematics.

Characteristics	**Quantity**
Type	Generic Lead Acid
Nominal Voltage	12
Nominal Capacity	1 kWh
Maximum Capacity	83.4 Ah
Capacity Ratio	0.403
Rate Constant	0.827/Hour
Effective Series Resistance	0.000596 Ohms
Other Round-Trip Losses	15%
Initial State of Charge	100%
Minimum State of Charge	20%
String Size	2